A Numerical Investigation of a Family of Frontal Cyclogenesis Events During CASP II

by

Ekaterina Radeva

A thesis submitted to the
Faculty of Graduate Studies and Research
in partial fulfilment of the requirements for the degree of
Master of Science
March, 1996
McGill University, Montreal, Quebec
CANADA

ISBN 0-612-12258-1

Résumé

Dans cette étude, nous exécutons une série de simulations numériques (48-60 h) d'une famille de cyclones frontaux qui s'est produite le long de la côte ouest de l'Océan Atlantique le 13-15 mars 1992. Une version à grille pilotée du modèle mésoéchelle de PSU/NCAR (MM4) avec une grille fine de 30 km de résolution a été utilisée. Il est démontré que le modèle MM4 reproduit convenablement la genèse, le déplacement et l'intensité des trois cyclones secondaires, leur structure thermique et circulation à la surface aussi que la précipitation associée aux systèmes. Finalement, un des cyclones frontaux (le MFC) parvient à éclipser le cyclone primaire dans la région polaire; il peut être tracé 3 jours auparavant comme provenant d'un mésocyclone au nord d'Alberta.

On trouve qu'un anneau du tourbillon potentiel (TP) à haut niveau joue un rôle important dans l'engendrement des cyclones frontaux et la détermination de leur déplacement. Apparemment, les cyclones se forment en conséquence de la superposition d'anomalies de TP à haut niveau et de baroclinicité intense à bas niveau derrière le front froid primaire; après ils se propagent toujours dans le secteur froid vers le centre du cyclone primaire. Il est montré de même, que l'intensification du MFC provoque l'apparition d'un creux à mésoechelle dans la troposphère basse à moyenne. Cela crée un décalage de phase favorable entre ledit creux et son homologue thermique plus lent, en facilitant la conversion baroclinique de l'énergie potentielle du système en énergie cinétique.

Le diagnostic des expériences de sensibilité démontre que: i) les forçages à large échelle déterminent l'engendrement et le déplacement des cyclones frontaux étant responsables pour environ 59% de l'intensité finale du MFC; ii) la baroclinicité à niveau bas et les anomalies de TP à niveau haut sont d'une importance presque égale lors de la formation des systèmes secs; iii) la perte d'inertie angulaire d'Ekman a tendance à ralentir considérablement le développement des cyclones frontaux; et iv) les flux de chaleur et d'humidité à la surface peuvent avoir un impact important (c.à.d., 59%) sur l'intensité finale des cyclones en présence du dégagement de chaleur latente, mais leur impact est insignifiant dans le cadre de la dynamique sèche.

Abstract

In this thesis, a series of (48 - 60 h) numerical simulations of a family of frontal cyclogenesis events that occurred over western Atlantic Ocean during 13 - 15 March 1992 are conducted using a nested-grid version of the PSU/NCAR mesoscale model (MM4) with a fine-mesh grid size of 30 km. It is shown that MM4 captures very well the genesis, track and intensity of three secondary cyclones, their associated thermal structure and precipitation pattern as well as their surface circulations. One of the frontal cyclones (MFC) eventually overpowers its parent cyclone in the polar region, and its origin could be traced back 3 days earlier from a mesolow over northern Alberta.

It is found that an upper-level potential vorticity (PV) ring plays an important role in determining the initiation and track of the frontal cyclones. The cyclones appear to form as a consequence of the superposition of upper-level PV anomalies on the low-level intense baroclinicity in the cold sector behind the slow moving primary cold front, and then they propagate into colder air towards the parent cyclone's center. It is also found that as the MFC intensifies, a mesoscale trough is induced in the low-to-middle troposphere, creating a favorable phase lag between the new pressure trough and a slow moving thermal wave. This phase lag provides a baroclinic conversion mechanism by which the system's kinetic energy could increase rapidly at the expense of available potential energy.

Diagnosis of sensitivity experiments reveals i) dry dynamics determines the initiation and track of the frontal cyclones, accounting for about 59% of the final intensity of the MFC; ii) the low-level baroclinicity and the upper-level PV anomalies are near-equally important in the genesis of the dry systems; iii) the Ekman spin-down tends to slow substantially the development of the frontal cyclones; and iv) surface heat and moisture fluxes could produce a significant impact (i.e., 59%) on the final intensity of the cyclones in the presence of latent heat release, but its impact is small in the dry dynamical framework.

Table of Contents

List of Figures

List of Tables

Acknowledgments

First and foremost, I want to thank my supervisors, Professors Da-Lin Zhang and John Gyakum, for their expert guidance and constant support throughout this thesis work. Their knowledge in mesoscale and large-scale modeling, synoptic meteorology, dynamics and physics, shared readily at any time, was of great benefit to me. I acknowledge that the computations for this work were performed by Professor Da-Lin Zhang on CRAY-YMP of the National Center for Atmospheric Research, which is sponsored by the National Science Foundation.

I especially thank Mr. Karl MacGillivray and Mr. Zonghui Huo for acquainting me with the "Recherche en Prévision Numérique" software and for their kind assistance in the various problems which arose during my study. Sincere thanks go also to Mr. Ning Bao for helping me with some model applications. Dr. Peter Zwack is acknowledged for providing the Zwack-Okossi equation solver, written by Serge Desjardins in Université de Québec à Montreal.

I am deeply grateful to my friends in the department for the interesting discussions and the good moments we had together during this research.

Last but not least, I wish to express my gratitude to my beloved ones, my parents and my husband, for their unconditional love and understanding throughout all these years.

Chapter 1 Introduction

1.1 The frontal cyclogenesis problem

The concept that extratropical cyclones grow on the boundary between the warm tropical air and the cold polar air can be traced back to the so-called "parallel current theory" proposed by Fitz-Roy in 1863. In this conceptual model, cyclones form asymmetrically as the polar air current meets and displaces the air current from the tropical region. In the early 1920s, Fitz-Roy's ideas were re-discovered and improved by scientists from the famous Bergen school of meteorology to form the polar front theory (Bjerknes and Solberg 1922). In this theory, cyclogenesis results from the instability of disturbances along a polar front, i.e., a surface of discontinuity separating tropical and polar air masses. The tendency for cyclones to develop in a family with each successive member occurring along the polar front to the southwest of its predecessor was also noticed by Bjerknes and Solberg (1922). They determined that the inter-cyclone spacing was usually of order 1000 km. Fig. 1.1 shows an example of such a frontal cyclone family along a polar cold front.

Even though the polar front theory deals with 'frontal cyclogenesis', or cyclone formation in areas of enhanced air-mass contrasts, it does not consider this process as a special type of a cyclogenesis phenomenon. According to this theory, all extratropical cyclones originate in the 'frontal' zone, and thus they are thought of as 'frontal' cyclones regardless of their characteristic spatial and temporal scales. In this thesis, the notion of 'frontal cyclogenesis' is used in somewhat different, narrower sense, i.e., to imply the cyclogenesis with a diameter of 800 - 1500 km along a polar front associated with a parent cyclone to the polar region. This notion is similar to that described by Thorncroft and Hoskins (1990). Therefore, the Norwegian conceptual model of frontal cyclones could be divided into two spatial regimes: one large-scale regime at a scale of 3000 km or larger and the other mesoscale or subsynoptic-scale regime at a scale in the range of 800 - 2000 km.

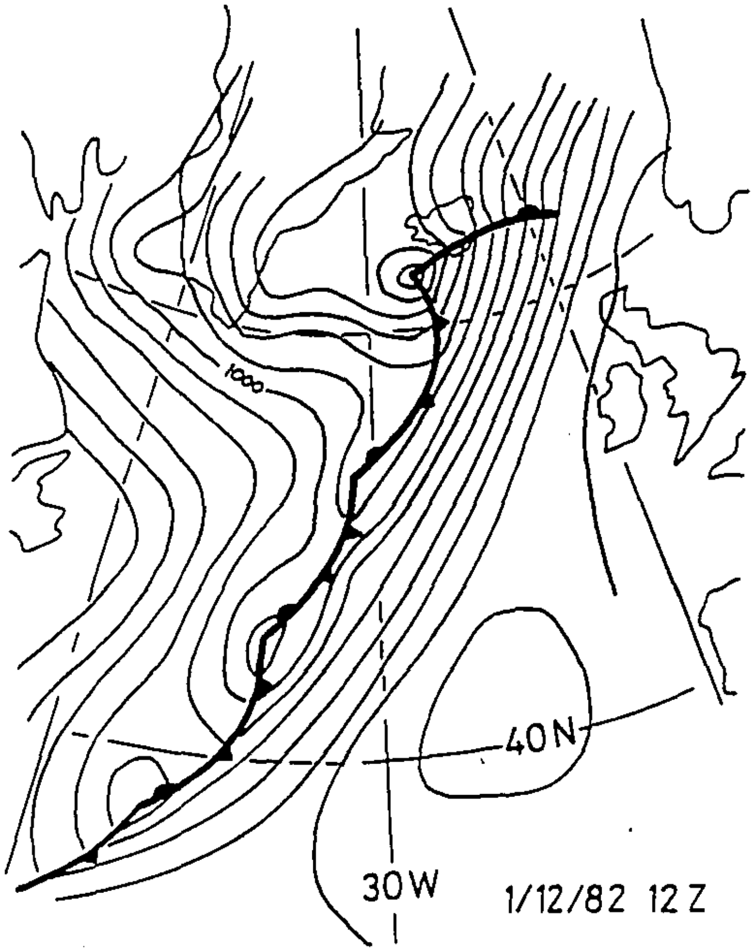

Fig. 1.1 Analysis of mean sea level pressure over the North Atlantic, 1 Dec. 1982 at 1200 UTC produced by the Meteorological Office. Intervals between isobars, 4 hPa. Figure is taken from Joly and Thorpe (1990a).

For the latter, frontal cyclones form often within a large-scale cyclone system or a 'parent' cyclone. Sooner or later, the cold front of the 'parent' cyclone becomes distorted by a single or several small depressions, which form a frontal wave. Observational studies show that they have horizontal wavelengths of 1000-2000 km and grow with time scales of less than one day (Joly and Thorpe 1990a). Even though they form in strong and deep baroclinic zones, mesocyclones tend to be shallower than their large-scale counterparts, particularly during their early development stages.

Frontal cyclogenesis phenomena have been found to occur all over the globe. Satellite photographs of North America and its coastal regions often reveal the existence of comma-shaped cloud patterns associated with subsynoptic-scale or mesoscale cyclones in polar air streams (Mullen 1979; Bosart and Sanders 1991; Wang 1995). Similar features have also been noted along Baiu fronts in East Asia and in association with polar lows in Europe (Schär and Davies 1989). While the frontal cyclogenesis is a widespread weather phenomenon, the understanding and forecasting of frontal cyclones still remain as one of the most serious challenges to meteorologists. Unlike the cyclogenesis in the large-scale regime that can be well accounted for by quasi-geostrophic baroclinic theory (Charney 1947; Eady 1949), the problem of understanding frontal cyclogenesis in the subsynoptic regime is the absence of a theoretical model that can explain the initiation and growth of disturbances with the particular spatial and temporal scales.

Recent instability studies of two-dimensional frontal baroclinic zones with continuous thermal structure have pointed to the existence of unstable modes that compare favorably with the growth rate and spatial scale of observed frontal waves. For the sake of clarity, we may divide these studies in supporting i) the 'in situ' instability; and ii) the upper-lower level interaction, as the frontal cyclogenesis mechanism. This classification actually corresponds to the Petterssen's Type A and Type B classification of cyclonic development (Petterssen and Smebye 1971).

The first category encompasses the research of Moore and Peltier (1986, 1988, 1989), Joly and Thorpe (1989, 1990a, 1990b) and Schär and Davies (1989). In exploring the stability of a steady deformation front in a uniform potential vorticity (PV) flow with a primitive equation model, Moore and Peltier (1986) found two sets of normal modes: one modified Eady mode with a wavelength between 3000 and 5000 km, and the other, what appeared to be a new mode, with a wavelength of approximately 1000 km. The mesocyclone mode, growing mainly by baroclinic energy conversion, has an e -folding time of one day which is greater than that of a typical baroclinic mode. Joly and Thorpe (1990a) added a low-level maximum of PV generated by latent heat release to the properties of unstable waves, and found that their growth derives kinetic energy from the basic state. Within a quasi- and semi-geostrophic framework, Schär and Davies (1989) found an unstable mode with a mixed barotropic-baroclinic character, and showed that the source and nature of the frontal instability is a vortex interaction effect acting across the thermal maximum of a low-level warm-band precursor.

In contrast to the natural selection principle where the fastest growing normal mode dominates over a random set of initial disturbances, baroclinic growth is often found, e.g., over western Atlantic, to be triggered by an upper-level disturbance moving off the continent (Sanders 1986). This forms the basis of the second category of frontal cyclogenesis (Hoskins et al. 1985; Thorncroft and Hoskins 1990). Thorncroft (1988) showed that explosively deepening cyclones were a result of the nonlinear interaction of the upper-tropospheric cut-off with an intense potential temperature gradient at a cold front during the final stages of a normal-mode baroclinic wave life cycle. This non-modal finite amplitude initiation can be thought of in terms of PV anomalies, as described by Hoskins et al. (1985).

A third theoretical approach to understanding the frontal cyclogenesis is to reconcile the observations with the conventional baroclinic instability of Charney (1947) and Eady (1949) that predicts disturbances with scales of 3000-4000 km to be the most unstable (e.g., Orlanski 1968, 1986; Kasahara and Rao 1972; Nakamura 1988). The discrepancies in the observed and predicted wavelengths were first discussed by Eady (1949), who noticed that the most unstable wave becomes shorter as the static stability diminishes. He further proposed that moist processes act to reduce the static stability of the atmosphere and hence the scale of baroclinic disturbances. Using a four-level quasi-geostrophic model, Staley and Gall (1977) also showed that changes in either the low-level wind shear or the static stability of a mean state can reduce the scale of the most unstable baroclinic wave from 4000 to 2000 km. Harrold and Browning (1969) observed that baroclinic zones, in which polar lows develop, are strongest near the surface, so they suggested that the shallow nature of these zones was responsible for the reduction in length scale. This idea was tested by Mansfield (1974) who, considering the stability of an Eady model with a lid artificially placed at 1.6 km, found that the most unstable disturbances were indeed of mesocyclone scale. This hypothesis was, however, questioned by Reed (1979) who pointed out that the cases studied by Harrold and Browning (1969) also had significant baroclinicity at upper levels.

Numerous observations and numerical studies have also been carried out to investigate the frontal cyclogenesis and related phenomena, e.g., coastal frontogenesis, low- and upper-level jets, and etc. For instance, Reed (1979) and Mullen (1979) studied the structures and large-scale environments for a total of 24 mesoscale cyclones that occurred behind or poleward of trailing cold fronts. They found that these mesocyclones are mostly associated with deep baroclinicity throughout the troposphere and they are located on the poleward side of upper-level jet streams in regions marked by strong cyclonic wind shear. In a case study of a small-scale polar-front cyclone, Ford and Moore (1989) noted that the storm appeared to grow in response to favorable low-level thermal advection rather than to any significant upper-level forcing. The low-level jet has been found to play an important role in frontal cyclogenesis (Ford and Moore 1989; Doyle and Warner 1991). Lapenta and Seaman (1992) and Doyle and Warner (1992) documented frontal cyclones which failed to develop in the absence of latent heat release despite the presence of strong low-level baroclinicity. Browning and Roberts (1994) and Browning and Golding (1995) examined the effect of upper-level high potential vorticity on the dry intrusions that appeared to determine the precipitation structure of frontal cyclones. In general, it has been revealed that the nonlinear interaction among various physical and dynamic processes, rather then an individual process, is responsible for the rapid evolution of these storms.

Despite the marked improvement in the numerical prediction of rapidly deepening extratropical cyclones, many operational models still have great difficulties in predicting mesocyclogenesis that often occurs in a polar frontal zone. While this type of frontal cyclogenesis has recently received considerable attention in theoretical studies (e.g., Moore and Peltier 1987; Thorncroft and Hoskins 1990), few case studies have been performed to examine the structure and evolution of these baroclinically driven mesoscale phenomena and investigate the processes responsible for their existence and pronounced case-to-case variability, owing partly to the lack of high-resolution observations and partly to the coarse grid resolution used in operational numerical weather prediction models. Of particular interest is that under certain circumstances, these baroclinically driven mesovortices can deepen rapidly and eventually dominate their parent cyclonic systems. Therefore, case studies on frontal cyclogenesis events are necessary for providing evidence to theoretical descriptions and for better understanding of the interaction of different processes leading to frontal cyclogenesis, thus in hope of improving the ability of numerical weather prediction.

1.2 Objectives of the thesis

In this thesis, we study the formation of a family of frontal cyclones that occurred on 13 - 15 March 1992 during CASP II (Canadian Atlantic Storms Program) using a 60-h high-resolution (Δx = 30 km) simulation of the case with the Pennsylvania State University/National Center of Atmospheric Research (PSU/NCAR) Mesoscale Model Version 4 (MM4; Anthes and Warner 1978; Anthes et al. 1987). This case is selected for this study because i) there were a family of (3 - 6) frontal cyclones, with diameters ranging from 800 - 1200 km, forming from a polar front that was initially located along the east coast of the U.S.; and ii) they were missed by the then operational models, such as the Nested-grid model (NGM) in the National Meteorological Center (NMC) and the Regional Finite-element (RFE) model in the Canadian Meteorological Centre (CMC). Moreover, one of the frontal cyclones underwent explosive deepening (i.e., 32 hPa/30 h) and it eventually overpowered the parent cyclonic system. However, both the RFE and NGM models, initialized at 0000 and 1200 UTC 13 March, predicted a mesotrough at the end of the cyclone's life cycle and failed to reproduce other frontal cyclogenesis events. Thus, the present case provides a unique opportunity to examine the mesoscale predictability of frontal cyclones and investigate the mechanism(s) by which these systems form and deepen.

The specific objectives of this thesis, pertaining to the physical understanding of the frontal cyclogenesis, are to:

i) demonstrate the numerical predictability of the 13-15 March 1992 family of frontal cyclogenesis events up to 60 h using a high-resolution research model with an enhanced analysis as the model initial conditions;

ii) examine the three-dimensional structures and evolution of the frontal cyclones in relation to their parent cyclone as well as their inter-relations;

iii) evaluate the sensitivity of the model-simulated cyclogenesis events to latent heat release, ocean surface fluxes and other model physical representations; and

iv) quantify the different physical processes taking place in the frontal cyclogenesis and clarify the relative importance of upper- and lower-level forcings in the genesis during the different stages of the cyclones life cycle.

The presentation of the thesis is organized as follows. Chapter 2 summarizes the model features and initial conditions used for the simulation. Chapter 3 presents a synoptic description of the case from 0000 UTC 13 to 1200 UTC 15 March 1992, and shows verification of the 60-h simulation against conventional and satellite observations. A possible scenario of the cyclone initiation and development from the PV perspective is also presented. In Chapter 4, we compare various sensitivity simulations in order to gain further insight into the factors that are important in the frontal cyclogenesis. A summary and conclusions are given in Chapter 5.

Chapter 2 Model Description and Initial Conditions

The model used for the present study is an improved version of the Penn State/NCAR hydrostatic, three-dimensional (3D), mesoscale model (MM4). This chapter describes briefly the basic model structure, including vertical and horizontal grids and finite-difference equations (Anthes and Warner 1978; Anthes et al. 1987), as well as the model initialization procedures and initial conditions. Section 2.1 outlines the model dynamics. Section 2.2 provides information on the numerical algorithms used for solving the dynamic equations. Description of the underlying physical aspects are given in section 2.3, and the model initialization and the initial conditions are presented in sections 2.4 and 2.5, respectively.

2.1 Model dynamics

The governing equations of the MM4 model, as originally described by Anthes and Warner (1978), are written in the terrain-following σ coordinate:

$$\sigma = (p - p_t)/(p_s - p_t) \qquad (2.1)$$

where p is pressure, p_s is the surface pressure, and p_t is the pressure at the top of the model atmosphere (in the present case p_t = 70 hPa). Apart from the prognostic momentum (u, v) equations, the model contains the continuity equation in terms of p_s, the first law of thermodynamics (T), and prognostic equations for the mixing ratios of water vapor, cloud water/ice and rainwater/snow (q_v, q_c and q_r), respectively. In addition to the seven prognostic variables, there are three diagnostic equations for $\dot{\sigma}$, ω and geopotential height, respectively. The effect of water vapor is included in the ideal gas law through the use of the virtual temperature, whereas the effect of liquid water or solid particle content, or the 'water loading', is incorporated through the hydrostatic equation. A complete list of the governing equations is given in Anthes et al. (1987).

2.2 Numerical algorithms

The MM4 model features a self-nesting capability (Zhang et al. 1986) which allows for simultaneous integration of the primitive equations over a coarse-grid mesh (CGM) domain with a grid size of 90 km and a nested fine-grid mesh (FGM) with a grid size of 30 km (Fig. 2.1). Both meshes are 'staggered' in the horizontal and vertical (Fig. 2.2). The horizontal staggering means that the momentum variables are defined at 'dot' points while all the other variables are defined at 'cross' points. This grid is the so-called 'Arakawa B' grid (Arakawa and Lamb, 1977) and shown by Anthes and Warner (1978) to lead to a more accurate calculation of the pressure-gradient force and the horizontal divergence. In the vertical staggering, the vertical velocity in σ-coordinates, $\dot{\sigma}$, is computed on full σ-levels, whereas all other variables are defined on half σ-levels, thus representing layer averages. Our CGM and FGM consists of 89 x 75 x 19 and 139 x 109 x 19 grid points, respectively, in (x, y, σ) dimensions and they are overlaid on a polar-stereographic map projection true at 60^0 N. The 20 σ-levels used for this study are: 0.0, 0.05, 0.1, 0.15, 0.206, 0.263, 0.321, 0.38, 0.44, 0.501, 0.562, 0.619, 0.676, 0.733, 0.789, 0.845, 0.901, 0.957, 0.99, 1.0, which give the 19 σ-layers of unequal thickness. Both computational domains cover the area of genesis and subsequent development of the frontal cyclones as well as the data-rich area to the west where upstream disturbances affecting the cyclones form.

The flux forms of the primitive equations are then spatially discretized using second-order finite differencing; the mass, momentum and total energy are approximately conserved. The time-integration scheme, designed by Brown and Campana (1978), is used to compute the pressure gradients at time step $\tau+1$ before computing the momentum variables at time step $\tau+1$, the so-called pressure-averaging method. Then, weighted averages of the geopotential and surface pressure at time steps $\tau-1$, τ and $\tau+1$ are used for the pressure-gradient force terms in the momentum equations. This method allows for a time step about 1.6 times larger than that supported by the conventional leapfrog scheme and produces virtually identical results

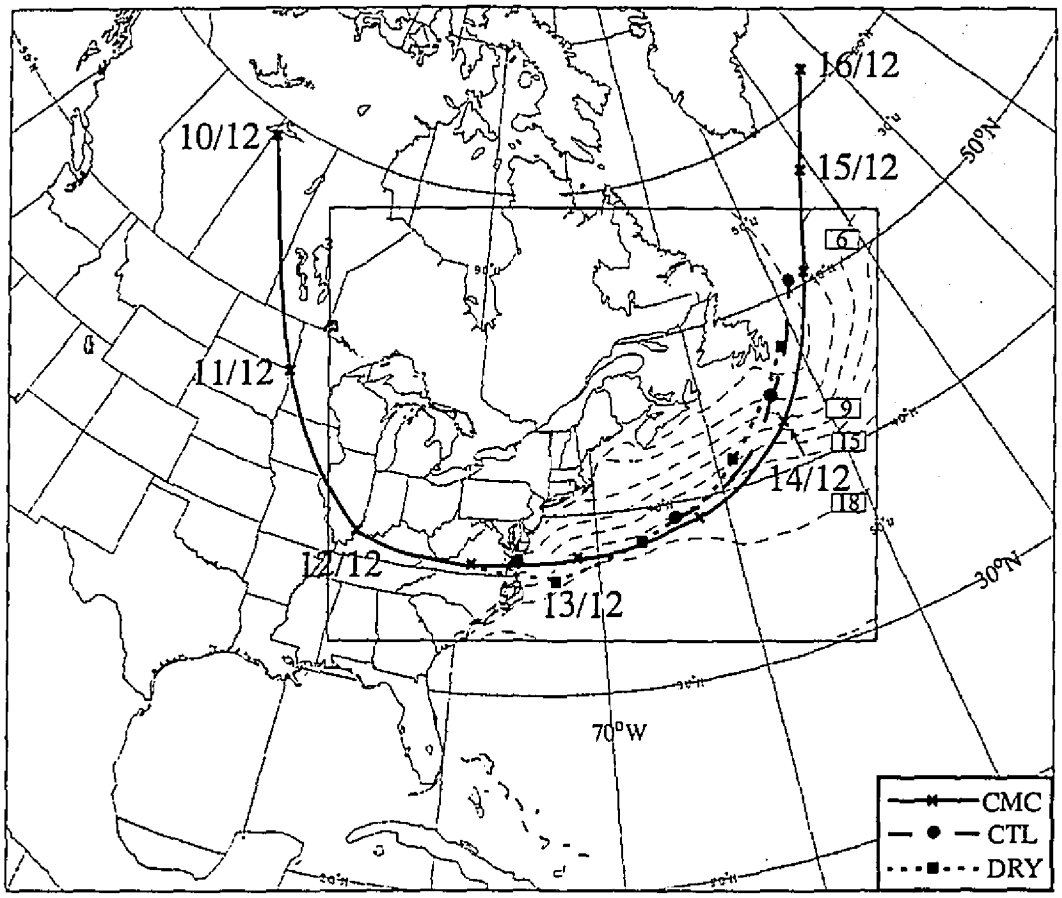

Fig. 2.1 Nested-grid domains with the fine mesh denoted by the internal frame. Sea-surface temperature (dashed) is given at intervals of 3 ^{0}C over the fine-mesh domain. Tracks of the major frontal cyclone (MFC) from the CMC analysis (solid) over a 6-day period with date/hour given, the 48-h control simulation (CTL, thick dashed), and no latent heating run (DRY, dotted) are also shown. Latitudes and longitudes are shown every 10^0.

a)

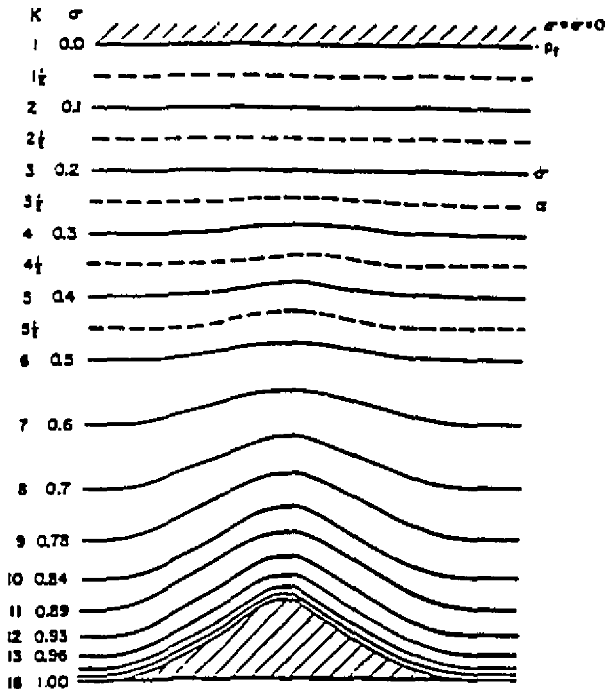

b)

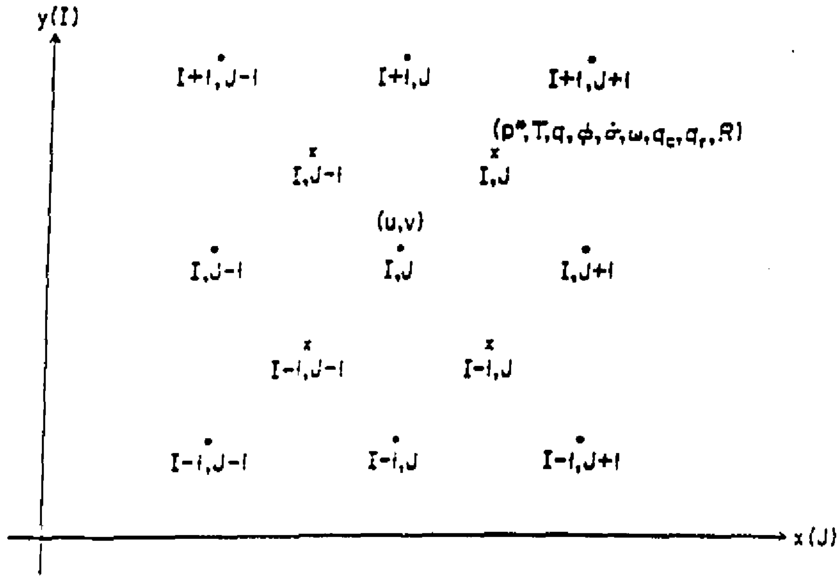

Fig. 2.2 Schematic grid structure of the PSU/NCAR model: a) vertical; and b) horizontal. Both figures are taken from Anthes et al. (1987).

(Anthes and Warner 1978). Second-order diffusion for the grid points next to the lateral boundaries and fourth-order diffusion for the interior of the grid points are used in order to control the nonlinear instability and numerical aliasing.

The model lateral boundary conditions in our case are specified in a sponge layer, comprising four cross- and five dot- points inward from the boundaries. The values of the prognostic variables at the outermost CGM lateral boundaries are determined by linearly interpolating 12-hourly observations in time (Perkey and Kreitzberg 1976), whereas in the sponge layer a weighted average of the interpolated observations and model-calculated tendencies is used. A two-way interactive self-nesting procedure is used at the interface between FGM and CGM (Zhang et al. 1986).

2.3 Model physics

a) Water cycle treatments

The realistic high-resolution simulation of multiple frontal cyclogenesis events requires an adequate representation of grid and sub-grid scale processes and water phase changes (Zhang et al. 1988), because the proper interplay between adiabatic dynamics and diabatic heating helps reproduce the track, intensity and mesoscale structures of the frontal cyclones. Thus, it is necessary to use an appropriate convective parameterization scheme suitable for a grid size of 20 -30 km that is coupled with a reasonable description of grid-scale condensation processes.

In this study, we use the Kain-Fritsch (1990, 1993; KF) cumulus parameterization scheme for the FGM, while the Anthes-H.L. Kuo convective scheme is used for the CGM. In the KF scheme, subgrid-scale convection is parameterized in such a way that it is assumed to remove convective available potential energy (CAPE) in a grid column within an advective time period. The scheme includes the effects of moist updrafts and downdrafts, and compensating subsidence; it also allows a two-way exchange of mass between cloud and environment through detrainment and entrainment which varies realistically as a function of environmental conditions. Conservation of mass, thermal energy and total moisture is assured. The Anthes-H.L. Kuo scheme is based on the concept that low-level mass and moisture convergence regulates the amount of convective mass and moisture fluxes. Moist convection occurs when the moisture convergence exceeds a critical value and the atmosphere is conditionally unstable.

These two convective schemes are coupled with more sophisticated explicit prediction of cloud water (ice) and rain water (snow) evolution (Zhang et al. 1988). The explicit moisture scheme, described in Hsie et al. (1984); Zhang (1989) and Dudhia (1989), includes additional prognostic equations for cloud water (ice) and rainwater (snow). This scheme assumes that a grid cell is completely filled with hydrometeors, which makes it suitable for high-resolution simulations. The explicit scheme contains the effects of virtual temperature, hydrostatic water loading, fallout of rainwater and snow, condensation and evaporation, freezing and melting, and sublimation. The phase demarcation between solid and liquid particles is made to depend upon the position of a parcel above or below the 0^0 C isotherm. This allows for economy of memory storage but causes the absence of supercooled droplets in the model. Proper communication between parameterized and explicit schemes is an important component of successful simulations (see Zhang et al. 1988; Molinari and Dudek 1992; Zhang et al. 1994). The implicit convection scheme is necessary for the representation of significant subgrid-scale vertical fluxes of heat and moisture, whereas the explicit scheme accounts for the transport of condensates before reaching the ground as precipitation. This provides a broader scale of interaction between subgrid-scale convection and mesoscale circulations (Zhang et al. 1988).

b) Planetary boundary layer (PBL) processes

It is well known that the planetary boundary layer (PBL) plays an important role in the exchange of heat, moisture and momentum between the surface and free atmosphere. In the present study, the frontal cyclones under investigation travel a great distance over the Atlantic ocean. Thus, appropriate treatments of heat, moisture and momentum fluxes could be crucial in obtaining a realistic simulation of the multiple frontal cyclogenesis scenarios. The Blackadar high-resolution PBL scheme (Zhang and Anthes 1982) is used for this study, in which land and water surfaces are treated differently. Over land, the surface temperature is derived from a surface energy budget following the 'force-restore' slab model developed by Blackadar (1976). It is given by

$$C_g \frac{\delta T_g}{\delta t} = R_n - H_m - H_s - L_v E_s \tag{2.2}$$

where C_g is the thermal capacity of the slab per unit area (J m^{-2} K^{-1}), R_n the net radiation, H_m the heat flow into the substrate, H_s the sensible heat flux into the atmosphere, L_v the latent heat of vaporization, and E_s the surface moisture flux. The net radiation, R_n, calculation accounts for the effects of water vapor absorption, clouds, multiple backscattering and reflection from aerosols as well as for cloud and precipitable water influences on downward infrared radiative flux. The heat flow into the ground, H_m, is computed through a simple first-order diffusion process, with the soil temperature being specified and kept fixed throughout the period of the integration. Finally, the sensible and moisture fluxes into the atmosphere are computed from similarity theory. All the basic parameters required for the surface budget calculations, i.e., moisture availability, surface albedo, roughness length, thermal capacity and surface emissivity, are derived from the land-use data archived at NCAR and given by a look-up table which assigns one value of a surface index for each grid point of the domain.

Over water surfaces, the surface temperature is assumed to be constant rather than predicted from Eq. (2.2). The heat and moisture fluxes are also computed from similarity theory, but with roughness length given by

$$z_0 = z_{ob} + 0.032\, u_*^2/g \tag{2.3}$$

where z_{ob} is a background roughness length of value 10^{-4} m, u_* is the frictional velocity and g is gravity (see Delsol et al. 1971). Over ice surfaces, defined as the ocean or lake surfaces with temperatures of less than - 2 ^{0}C, no upward surface heat and moisture fluxes are allowed. A surface roughness length of 1 cm is used in the calculation of surface momentum fluxes. This treatment is critical in reproducing the low-level temperature structures over the Hudson Bay, Labrador Sea and along ice edges, as will be shown in section 3.

Once the surface fluxes are known, the surface-layer horizontal wind (u and v), potential temperature (θ), mixing ratio (q_v), and cloud water (q_c) can be calculated and their vertical diffusion under stable conditions is computed from K-theory using an implicit diffusion scheme (Richtmyer 1957; Zhang and Anthes 1982). In the K-theory the vertical eddy diffusivity is a function of the local Richardson number. In the case of free convection, a PBL height is diagnosed and the vertical mixing takes place between the lowest layer and each layer in the mixed layer, a procedure described by Blackadar (1979) and Zhang and Anthes (1982).

2.4 Model initialization

The model was initialized at 0000 UTC 13 March 1992 with data from conventional observations, following the method described in Zhang et al. (1986), and then integrated to 60 h. The standard global National Meteorological Center (NMC) analysis was first interpolated to the model CGM as a first guess and then enhanced with rawinsonde observations at 10 mandatory and 10 significant levels (i.e., 990, 970, 950, 925, 900, 875, 825, 800, 750, 600 hPa) through a successive-correction method (Benjamin and Seaman 1985). Over the ocean, modifications of the global analysis are limited to the use of ship and buoy observations. Sea-surface temperatures are read from NCAR's Navy tape (see Fig. 2.1). The resulting CGM fields were then interpolated to the FGM. No balancing between the mass and wind fields was done, but the vertically integrated divergence was set to zero in order to minimize gravity wave noise in the first few hours of integration.

2.5 Initial conditions

Figure 2.3 shows surface maps at the model initial time, i.e., 0000 UTC 13 March 1992 (henceforth 13/00), and 12 h earlier (i.e., 12/12). The large-scale circulation was seen to be dominated by a robust low-pressure system with a central pressure of 980 hPa at 12/12, positioned over the south-central portion of Quebec. This low, hereafter referred to as the parent cyclone ("P"), had experienced a 12-hPa deepening as it moved from central Ohio during a 2-day period (not shown). There were, at least, three visible pressure perturbations under the influence of the cyclonic flow: one associated with a primary cold front extending southeastward along the east coast of Newfoundland, followed by a surface short-wave (trough/ridge) system that was more evident along the coast of the middle Atlantic states and a secondary low system centered near the common border of Illinois, Kentucky and Missouri. The secondary low could be traced back to a surface cyclone, which changed little in intensity, two days earlier in northern Saskatchewan (Fig. 2.1). It is important to note i) a cold polar air surge to the east of the Rocky Mountains that has forced the secondary system to propagate rapidly southeastward; and ii) a slowly-moving intense baroclinic zone left behind the primary cold front within which the short-wave system was located (Fig. 2.3a). Both troughs in these systems later developed into two intense secondary or frontal cyclones within the baroclinic regions as they advanced into the primary frontal zone; so they will be referred to as the major ("M") and the northern ("N") frontal cyclones or MFC and NFC for short (see Fig. 2.3), respectively, since the former eventually overpowered the parent cyclone. A third secondary cyclone emerged at 14/12 to the south of the MFC, the so named southern frontal cyclone ("S") or SFC. At the model initial time, i.e., 13/00, the secondary low weakened into a mesotrough (with a weak vorticity center) after it passed over the Appalachians (Fig. 2.3b).

a)

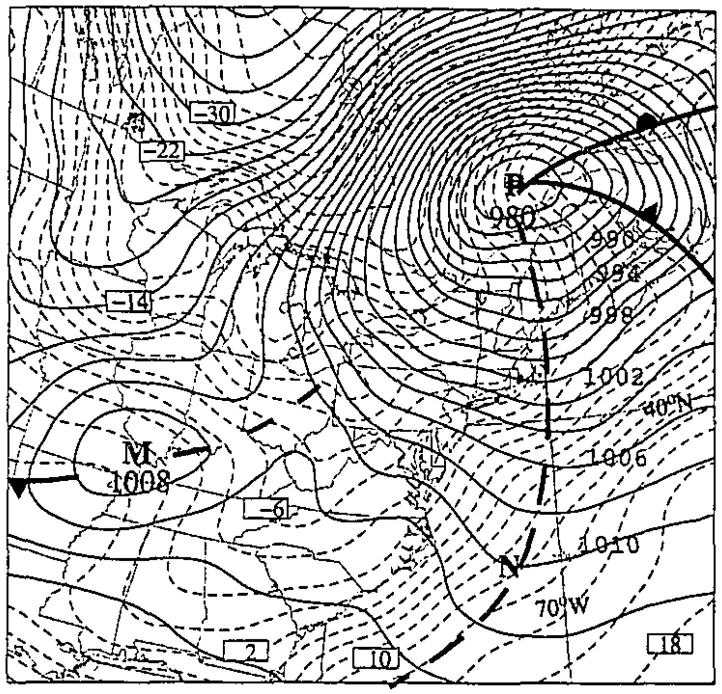

b)

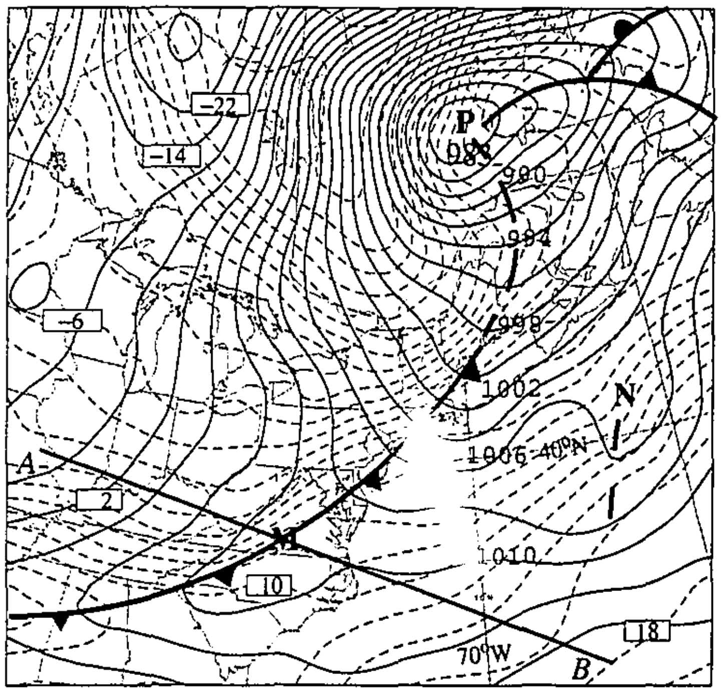

Fig. 2.3 The CMC analyzed sea-level pressure (solid) at intervals of 2 hPa and surface temperature (dashed) at intervals of 2 °C: a) 12-h before the model initial time (i.e., 1200 UTC 12 March 1992); b) at the model initial time (i.e., 0000 UTC 13 March 1992). Subjectively analyzed fronts and troughs are also shown. Centers of the parent, major and northern cyclones are marked by letters, "P", "M", and "N", respectively. Line AB in (b) shows location of the vertical cross section used in Fig. 2.5.

Meanwhile, the rapid propagation of the cold polar air mass resulted in the formation of a new large-scale cold front extending along the east coast through North Carolina into Texas, whereas the short-wave trough, "N", began to amplify in the baroclinic zone as it moved rapidly northeastward. The MFC ("M") under investigation would develop out of a vorticity center (i.e., the mesotrough) in the frontal zone over North Carolina after it moved offshore. In contrast, the parent cyclone showed a sign of weakening and slower northeastward movement during the 12-h period.

Upper-level large-scale circulations were also dominated by the parent cyclone (see Fig. 2.4), but it exhibits a vertically coherent structure up to 250 hPa. This again indicates little support for the further deepening of the parent cyclone, and, indeed, it began to fill subsequently. In contrast, a SW-NE oriented short-wave trough, superposed on the cyclone's circulation, shows a rearward-tilted structure from the surface front (cf. Figs. 2.3b and 2.4a-c). This trough, propagating together with the surface secondary mesolow, had weakened substantially during the previous two days (not shown). The 850-hPa map displays moderate cold advection occurring in the vicinity of the trough over the southeastern states (Fig. 2.4c); but its magnitude decreases upward. Of interest is that, despite the presence of intense temperature gradients, little thermal advection was evident in the low to middle tropospheres elsewhere, except near the primary cold/warm frontal system to the northeast (Figs. 2.4b,c). Nevertheless, the intense S-N thermal gradients appear to be responsible for the development of an especially strong westerly jet streak at 250 hPa (Fig. 2.4a); its peak intensity, located at the Carolinas' border, is over 75 m s^{-1}.

It is apparent that the pre-MFC, "M", was now located over a region of positive vorticity advection (Figs. 2.4b,c) and near the core of the jet streak (Fig. 2.4a). As will be seen in section 3.2, the pre-MFC propagated rapidly ahead of the jet-streak core into its left exit side after 14/00. According to Uccellini and Johnson (1979), the intense jet streak tends to induce a thermally indirect transverse ageostrophic circulation ahead in its left exit region. In this sense, the jet-streak induced circulation contributes little to the genesis of the MFC, but it might help

a)

b)

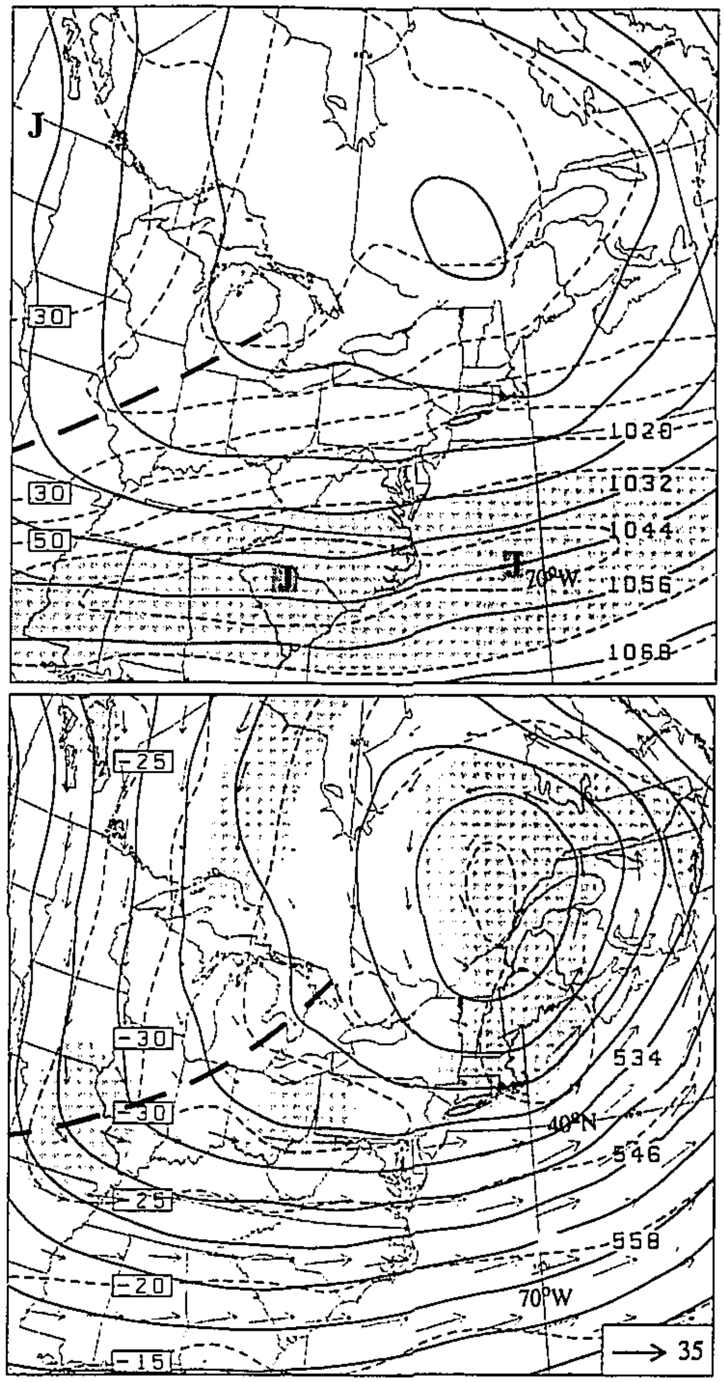

Fig. 2.4 The CMC upper-level analysis at the model initial time (i.e., 0000 UTC 13 March 1992): a) 250-hPa height (solid) at intervals of 12 dam and isotachs (dashed) at intervals of 10 m s^{-1} (>60 m s^{-1} shaded); with the jet streak marked by the letter "J"; b) 500-hPa height (solid) at intervals of 6 dam and isotherms (dashed) at interval of 5 °C, superposed with flow vectors and absolute vorticity (>1.5x10^{-4} s^{-1} shaded); c) 850- hPa height (solid) at intervals of 3 dam and isotherms (dashed) at intervals of 5 °C, superposed with flow vectors and absolute vorticity (>1.5x10^{-4} s^{-1} shaded). Thick dashed lines represent subjectively analyzed troughs. Inset indicates the scale of horizontal wind speed (m s^{-1}).

c)

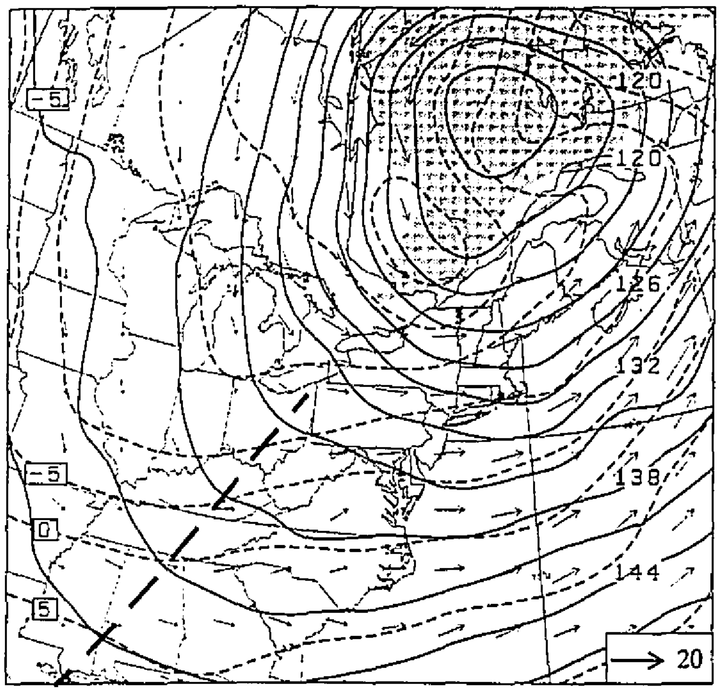

Fig. 2.4 (continued)

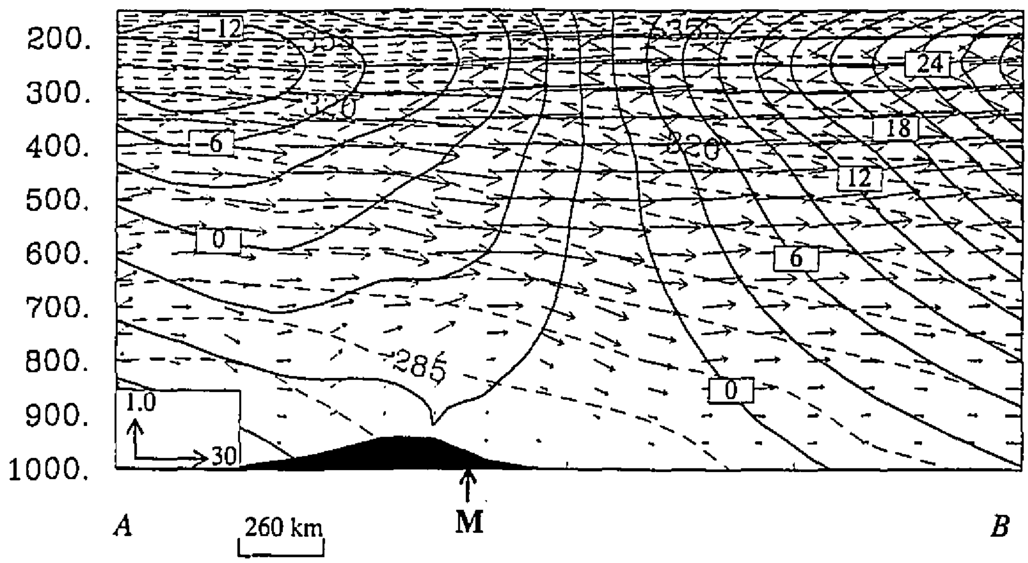

Fig. 2.5 Vertical cross section of height deviations at intervals of 3 dam (solid), and potential temperature θ (dashed) at intervals of 5 K, superposed with along-plane system-relative wind vectors at the model initial time (i.e., 0000 UTC 13 March 1992), which is taken along the line AB in Fig. 2.3. Inset indicates the scale of vertical motion (Pa s^{-1}) and horizontal wind speed (m s^{-1}).

to precondition the environment for the subsequent explosive deepening of the system. Colman et al. (1994) also found little evidence of such favorable transverse ageostrophic circulaitons in some rapid cyclogenesis cases.

To help understand the interactions between the low- and the upper-level disturbances, Fig. 2.5 shows a vertical cross section of height deviations and potential temperature through the pre-MFC, "M", at the model initial time. Height deviations are obtained by deducting the height pressure-level averages within the cross section. It is evident that the cold frontal zone was shallow, only up to 800 hPa, and about to move over the Appalachians. It was characterized by a weak ascending (descending) flow with relatively lower (moderate) static stability ahead (behind). A deep layer of strong vertical wind shear is also evident. The weak static stability in the prefrontal environment is closely related to the presence of the underlying warm Gulf Stream water, and thus tends to render it more susceptible to upright convection in the presence of a favorable forcing. The pre-MFC is located downstream of the upper-level trough which tilts westward with height. This baroclinic trough clearly provides a favorable quasi-geostrophic forcing to the initial development of the MFC.

Chapter 3 Case Description and Simulation

In this chapter. we describe the sequence of a family of secondary cyclogenesis events in relation to their parent cyclone during a 60-h integration period (from 13/00-00 to 15/12-60 March 1992), using the CMC analysis, the MM4 simulation and satellite observations. In addition, the performance of the 60-h simulation will be evaluated through verification against the CMC analysis and other available data. In view of the limited data over the ocean for verification, only surface maps, including the cyclones' intensity, tracks and their associated precipitation, will be examined. On the other hand, numerical models can often reproduce very well the structure and evolution of large-scale flows, such as the upper-level traveling short-wave trough and the jet streak in the present case. Thus, the simulated upper-level maps will be used to understand how these large-scale disturbances interact with the lower-level circulations in influencing the multiple secondary cyclogenesis events.

This chapter is organized as follows. Section 3.1 describes the evolution of the parent and the newly formed multiple secondary cyclones, based on the surface maps, and the verification of the 60-h simulation against available observations. Section 3.2 shows the evolution of larger-scale flows, and section 3.3 presents the vertical structure of the two different types of cyclones. Section 3.4 provides some insight into the roles of the low- and upper-level interactions in the multiple cyclogenesis events from a potential vorticity (PV) perspective (Hoskins et al. 1985).

3.1 The multiple cyclogenesis events

In this study, we focus primarily on the major frontal cyclogenesis scenario (i.e., MFC), with less attention given to the other secondary genesis events. Figs. 2.1 and 3.1a compare, respectively, the tracks and central pressure traces of the MFC between the MM4 simulation and the CMC analysis. As mentioned before, the MFC originates from a vorticity

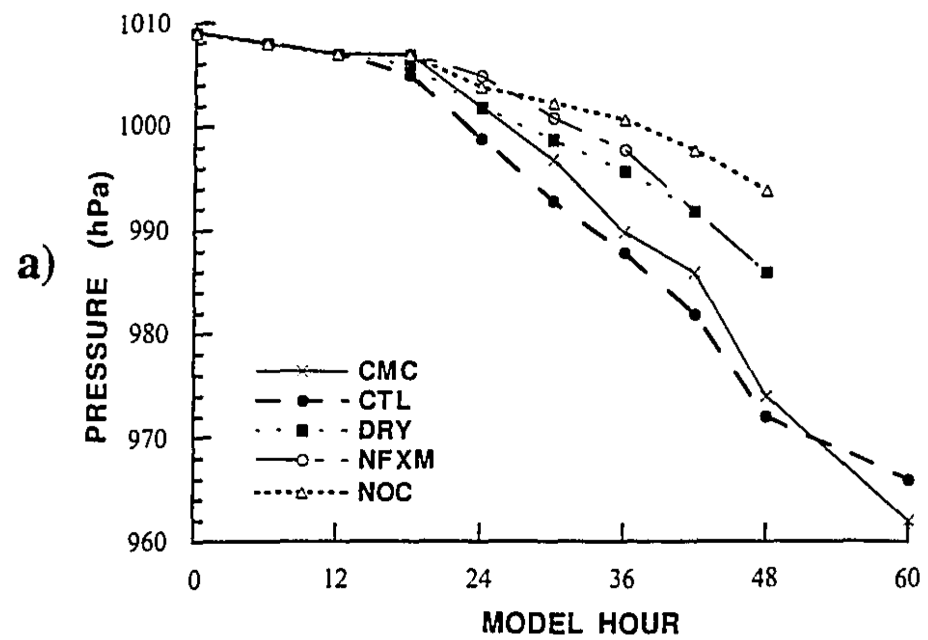

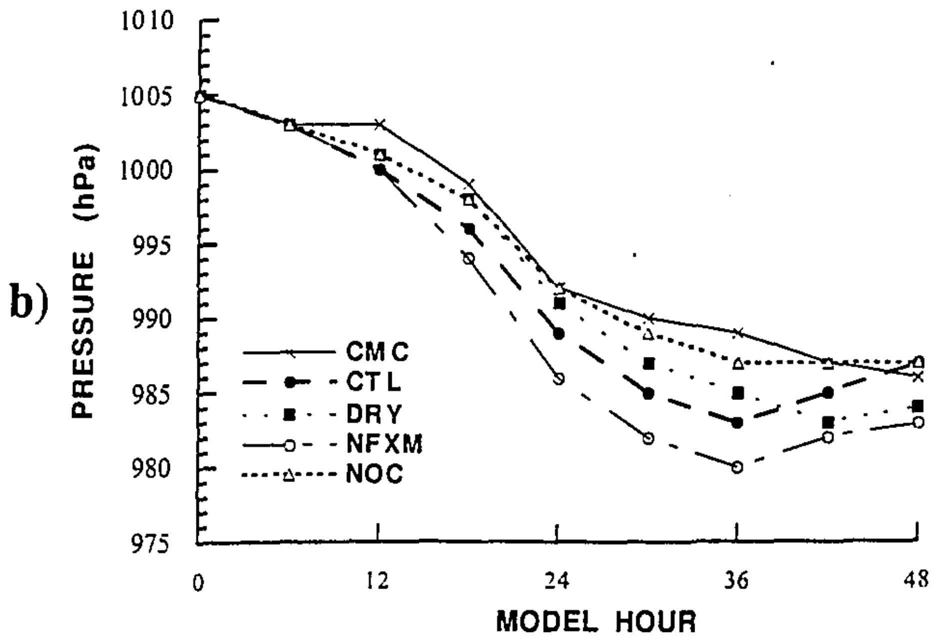

Fig. 3.1 Time series of the central sea-level pressure of a) the MFC; and b) the NFC from the CMC analysis (—×—), CTL (control; — ● —), DRY (no latent heating; - - ■ - -), NFXM (no fluxes moist; – -○- –) and NOC (no ocean surface; · · ·△· · ·); c) time series of the absolute geostrophic vorticity for the MFC averaged between 900 hPa and 1000 hPa from Exps. CTL, DRY and NOC.

c)

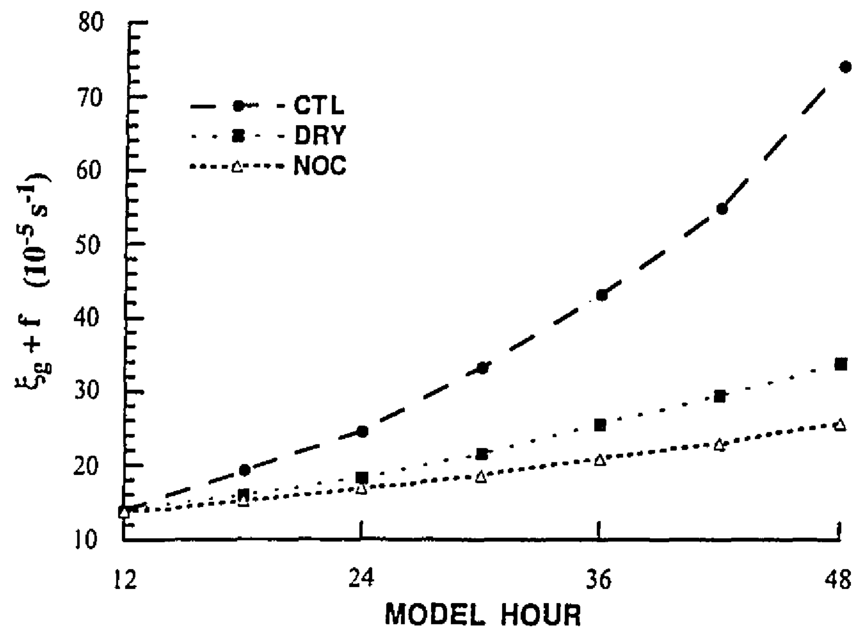

Fig. 3.1 (continued)

center in the frontal zone over central North Carolina (cf. Figs. 2.3 and 2.1). Its first closed isobar begins to emerge after 12-h integration, i.e., at 1200 UTC 13 March (henceforth 13/12-12), as the front moved offshore. The MFC propagated northeastward at a speed between 15 and 20 m s^{-1}. It is evident that the predicted track follows closely the analyzed one, with some systematical deviation to the west. The maximum departure between the two tracks is less than 200 km at the end of the 60-h integration period, during which the MFC has traveled more than 4000 km from North Carolina to the far east of Newfoundland.

The model also simulates well the slow growth of the MFC during the first 18-h of integration, the rapid deepening between 13/18-18 and 15/00-48 and its weak intensification afterwards; so its life cycle can be divided into the genesis, rapid and slow deepening stages accordingly. In particular, the MM4 replicates the observed deepening rate of 33 hPa in 30 h between 13/18-18 and 15/00-48, which qualifies it as an "oceanic bomb" in accordance with Sanders and Gyakum (1980). The systematic 1-2 hPa overprediction in the first 48-h and the subsequent 1-2 hPa underprediction of the cyclone's central pressure are acceptable, when considering the different resolutions used between the simulation (Δx = 30 km) and the observations far offshore (> 150 km). The average e-folding time between 13/12-12 and 15/00-48, computed from the geostrophic vorticity equation (see Fig. 3.1a and Appendix A), is about 22 h, which is close to the theoretical evaluations for frontal cyclogenesis (e.g., Joly and Thorpe 1990a; Moore and Peltier 1986; Schär and Davies 1989).

The MM4 appears to overpredict the central pressure of the NFC between 24- and 36- h simulation (see Fig. 3.1b). Again, this overprediction could be partly attributed to the relatively coarse observations over the ocean, particularly for such a mesocyclone with a lateral dimension much smaller than the MFC. Nevertheless, the model captures well the final intensity of the NFC, as it propagated into the CASP II network region. The NFC experienced 16-hPa deepening in 36 h. The simulation of the parent cyclone and the SFC will be discussed below in conjunction with their associated surface circulations.

Our detailed analyses of the multiple frontal cyclogenesis events focus on how well the model reproduces their genesis and associated circulation characteristics in relation to the parent cyclone. Figures 3.2 and 3.4-3.6 compare 12 hourly the simulated surface maps to the observed ones over subdomains that move with the MFC system, whereas Fig. 3.8 shows some selected satellite imageries during the study period. We have shown in section 2.4 that the rapid southeastward propagation of an intense baroclinic zone assisted the organization of a large-scale cold front along the east coast at 13/00-00. However, the coastal front evolved quickly into a frontal trough 12 h later, i.e., at 13/12-12, after the intense baroclinic zone merged with the slow-moving cold air mass offshore (cf. Figs. 2.3 and 3.2a). The sign of the dissipated mesolow or pre-MFC ("M") was still visible after the merging, as evidenced by the loose pressure gradient at the southern portion of the trough. Of particular importance is that the merging increased the cross-frontal baroclinicity through a favorable juxtaposition with the cross-isobaric flow. This would naturally result in the development of warm (cold) advection ahead of (behind) the trough axis, more intense in the vicinity of the pre-MFC. Clearly, this basic state is favorable for baroclinic growth of any disturbance, like the present mesotrough, according to baroclinic theory (Holton 1993). In contrast, the parent cyclone ("P") continued to decay as it traveled slowly northward. Because of the slow movement, the two baroclinic zones to the north behind and ahead of the coastal trough remained well separated. The thermal ridge to the northeast of the parent cyclone center, which from a PV-inversion viewpoint (Davis and Emanuel 1991) can be regarded as equivalent to a positive PV-anomaly contribution to the surface development, was also weakening with time (cf. Figs. 2.3 and 3.2a).

It is apparent that the model reproduces fairly well the intensity and propagation of the parent cyclone, the orientation of the large-scale frontal trough, the intense thermal gradients across it as well as the pre-MFC to the south (cf. Figs. 3.2a,b). An upper-air sounding, taken at the pre-MFC center (see Fig. 3.3a), shows that the cyclogenesis is about to take place in a deep baroclinically unstable state, as indicated by the intense westerly shear in the vertical.

a)

b)

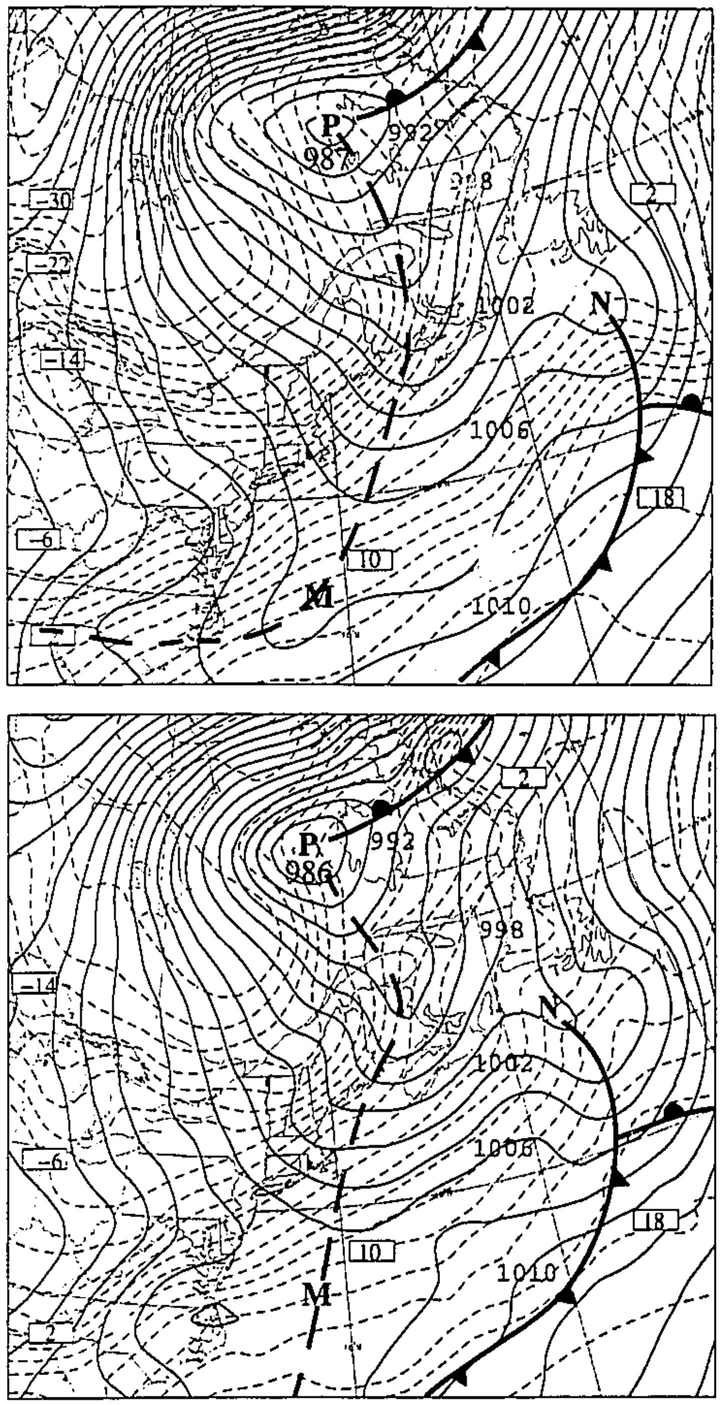

Fig. 3.2 Sea-level pressure (solid) at intervals of 2 hPa and surface temperature (dashed) at intervals of 2 °C for 1200 UTC 13 March 1992 (13/12-12) from a) CMC analysis; b) 12-h control simulation (CTL). c) Equivalent potential temperature θ_e (solid) at intervals of 5 K at 900 hPa, superposed with wind vectors, and precipitation rates (0.5, 1, 2, 5 mm h^{-1}) from 12-h control simulation. Subjectively analyzed troughs and fronts are also shown. Centers of the parent, major and northern cyclones are marked by letters "P", "M" and "N", respectively. Inset indicates the scale of horizontal wind (m s^{-1}).

c)

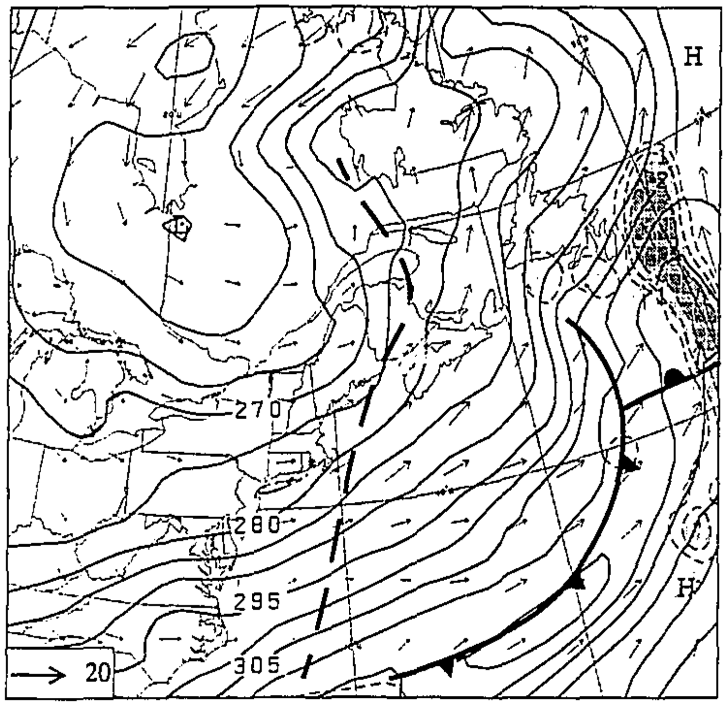

Fig. 3.2 (continued)

a)

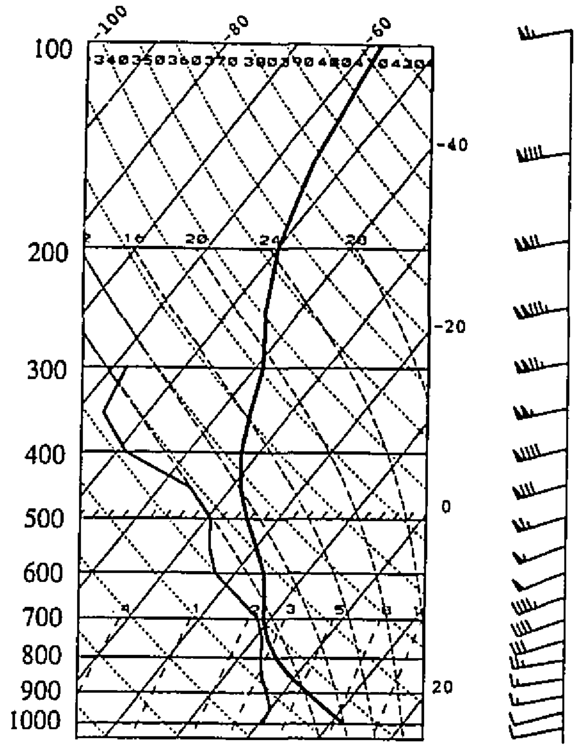

b)

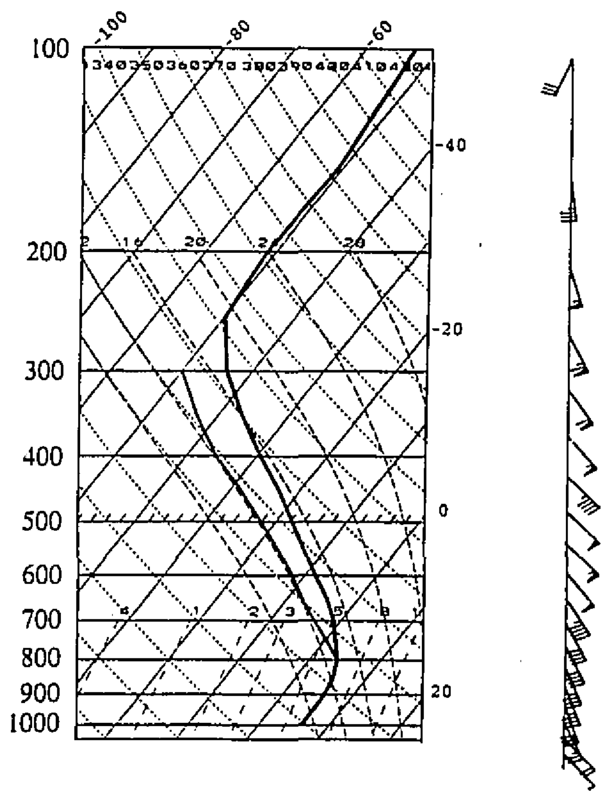

Fig. 3.3 Skew T/log p diagrams taken at the center of: a) the pre-MFC from 12-h control simulation; and b) the MFC from 48-h control simulation. A full (half) barb is 5 (2.5) m s^{-1} and a pennant is 25 m s^{-1}.

The atmospheric stratification is characterized by a well-mixed boundary layer up to 850 hPa as a result of the colder air overrunning the warm Gulf Stream water, and a deep-layer of warming and drying above 400 hPa which, to be shown in section 3.4, results from the descent of stratospheric air. During this 12-h period, the model produces little precipitation associated with the intensifying frontal trough, suggesting that dry dynamics plays an important role during the very genesis stage. The model-produced precipitation occurs mainly ahead of the primary cold front to the east, which is more or less in agreement with the satellite observations (not shown).

It is encouraging that the model replicates well the propagation of the NFC ("N"), and its associated warm and cold frontal structures ahead of the large-scale frontal trough. This mesolow intensified from a short-wave trough just off the North Carolina coast 24 h earlier (cf. Figs. 2.3 and 3.2). The strong thermal advection across the trough plus some upper-level support, to be discussed in section 3.3, appear to determine the successful predictability of this system at nearly the right location and the right time, since in the present case few upper-air observations were available to resolve it in the model initial conditions. Note that in this study moist isentropes (i.e., θ_e) at 900 hPa in conjunction with surface winds are used to determine the orientation of simulated cold and warm fronts (Fig. 3.2c). The frontal positions so obtained may differ from those determined entirely from the surface data as in the CMC analysis. It is found that the definition based on the θ_e analysis provides a more reasonable description of the frontal positions, particularly with respect to the continuity of the frontal evolution, than that from the CMC analysis, as the fronts move over the warm ocean surface. Some discrepancies between the simulation and the CMC analysis exist. Most of them are either transient (e.g., the closed isobar of 1006 hPa over Cape Hatteras) or likely due to the lack of appropriate observations over the ocean (e.g., the surface low over Labrador Sea) and in the Canadian North (e.g., the coldest air mass behind the parent cyclone).

At 14/00-24, both the CMC analysis and the simulation show the growth of a closed mesolow (i.e., the MFC) out of the mesotrough in the frontal zone (cf. Figs. 3.2 and 3.4); so it indeed can be regarded as a frontal cyclone. It is found from the simulation that once the cyclone develops its first closed isobar, it begins to form its own warm/cold frontal systems with corresponding organized thermal advection. Meanwhile, the NFC continued to deepen as it propagated rapidly into southern Labrador Sea under the influence of the general cyclonic flow. Its intensity even becomes stronger than that of the parent cyclone from the simulation. It is seen that a two-member cyclone family forms along the newly organized large-scale front, after the MFC and NFC both advanced into the leading portion of the slowly moving baroclinic zone (see Figs. 3.4b,c). This pattern is very similar to the frontal wave structure shown by Joly and Thorpe (1990, cf. Figs. 1.1 and 3.4c). Note, though, that the analyzed baroclinic zone to the east of the NFC does not seem to be consistent with the local pressure configuration, either from the continuity consideration (cf. Figs. 3.2a, 3.4a and 3.5a) or from any conceptual cyclone models (Reed 1990; Uccellini 1990). Such an inconsistency could also be evaluated from the time evolution of the simulated θ_e contours (cf. Figs. 3.2c, 3.4c and 3.5c), since θ_e is a conserved variable in an inviscid, pseudoadiabatic flow. It is seen that a high-θ_e tongue, coupled with along-frontal flows, is distributed ahead of the baroclinic zone (Fig. 3.4c), which clearly feeds energy into the cyclone systems in the form of latent and sensible heat along the fronts. In fact, an elongated rainfall band, mostly convective in nature, has been reproduced ahead of the leading frontal zone, whereas moderate stratiform precipitation occurs along the warm fronts of the two cyclones (cf. Figs. 3.4a and 3.8). It should be pointed out that the more rapid deepening of the MFC at this stage coincides with the intense precipitation occurring to the north (cf. Figs. 3.1 and 3.8). It is apparent that the slowly decaying parent cyclone and the previous frontal trough tend to lose their local circulation characteristics as the MFC deepens rapidly with time.

By 14/12-36, the MFC had deepened rapidly from 1000 to 988 hPa in 12 h; it was embedded in a broad SW-NE elongated surface low (see Fig. 3.5a). However, this elongated pattern was not present in the CMC analysis at either 6 h earlier or later (not shown).

a)

b)

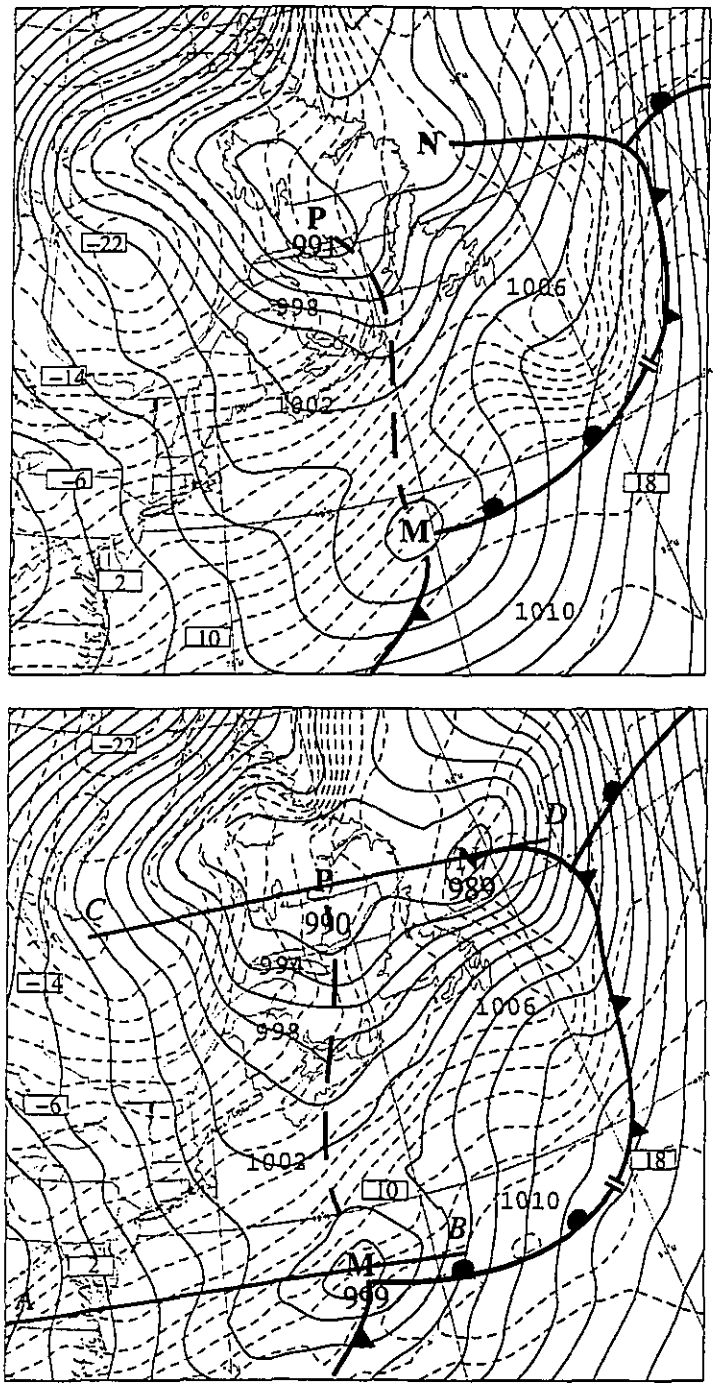

Fig. 3.4 As in Fig. 3.2, but for the CMC analysis and 24-h control simulation valid at 0000 UTC 14 March 1992 (14/00-24). Lines AB and CD in (b) show the locations of cross sections used in Figs. 3.12a, b, respectively.

c)

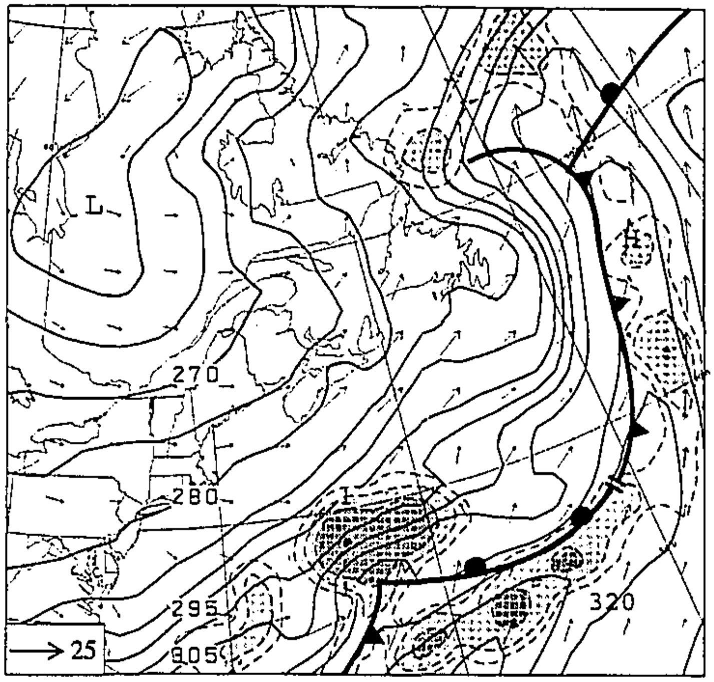

Fig. 3.4 (continued)

a)

b)

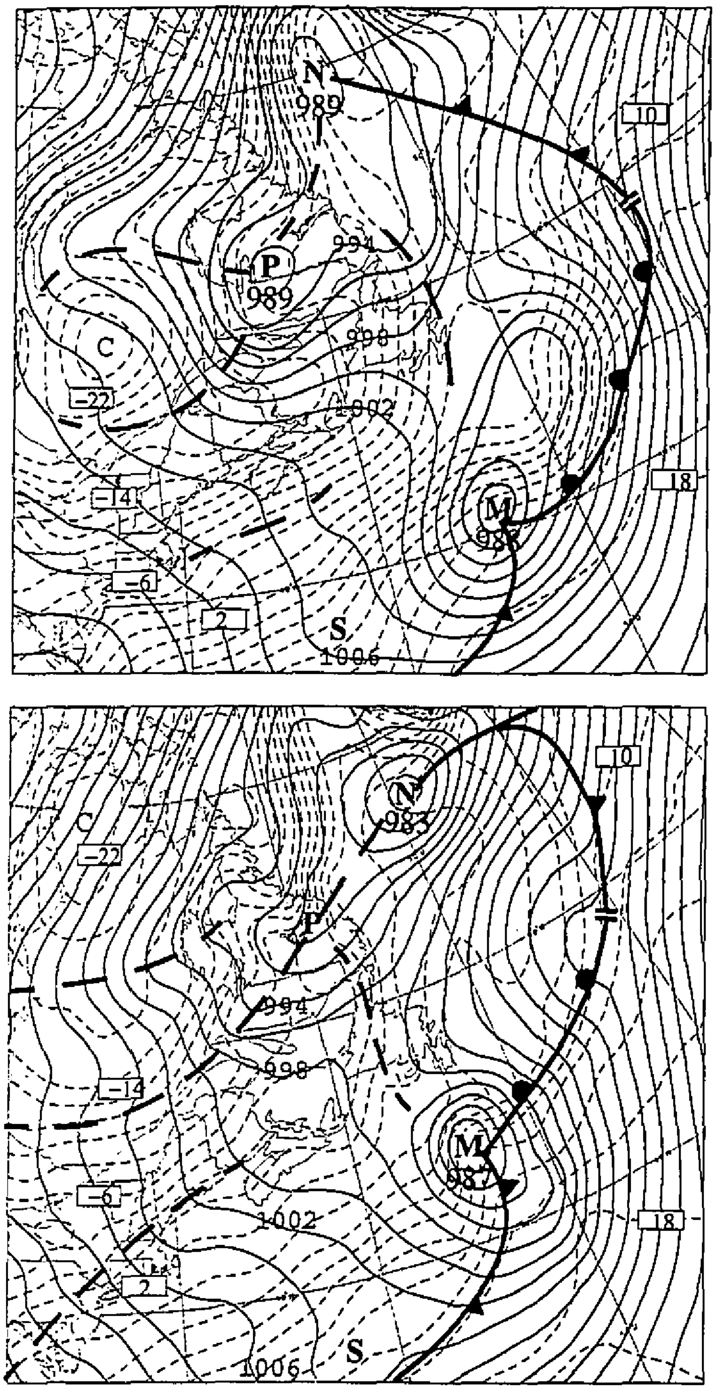

Fig. 3.5 As in Fig. 3.2, but for 1200 UTC 14 March 1992 (14/12-36).

c)

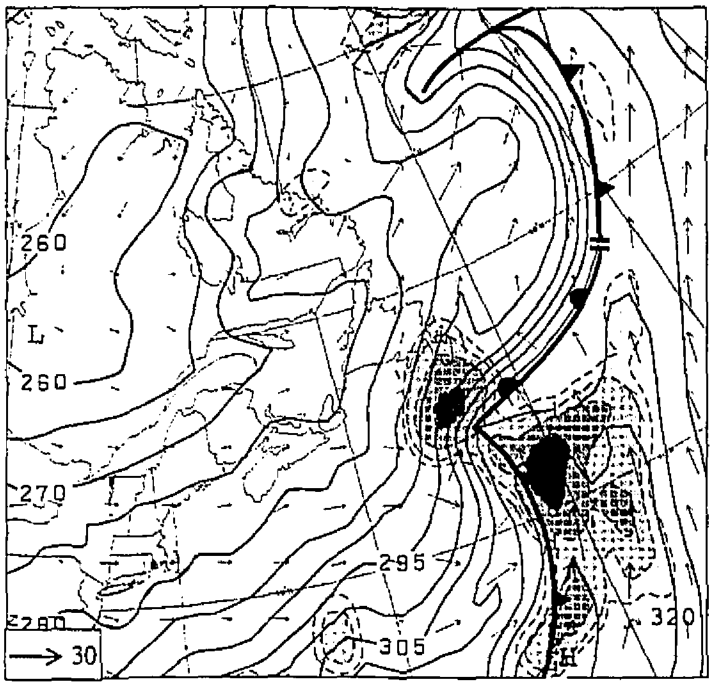

Fig. 3.5 (continued)

In contrast, the 36-h simulation exhibits a more circular cyclone pattern which is typical for explosively deepening cyclones (Fig. 3.5b). This indicates that the elongated trough to the northeast of the analyzed MFC might be caused by an inconsistent ship report far offshore, i.e., at 50^0 W/44^0 N. Nevertheless, the cold/warm frontal structures associated with the MFC in the CMC analysis were well defined. It is evident that the model reproduces its 12-hPa central pressure drop in 12 h as well as the related cold/warm frontal systems (cf. Figs. 3.5a-c). Note the different precipitation structure from the one simulated 12 h earlier (cf. Figs. 3.4c and 3.5c). Specifically, more intense and extensive rain falls ahead of the cold front and near the MFC's center, whereas little precipitation occurs to the north along the primary baroclinic zone. This is because the precipitating system to the south tends to consume most of the CAPE and available moisture so that the energy supply to the northern system is "blocked." This can be seen from the presence of a wide (narrow) high-θ_e tongue with a strong (moderate) low-level jet to the south (north) ahead of the frontal zones (see Fig. 3.5c). This scenario also conforms with the development of high (low) cloud tops to the south (north) that is visible in the infrared satellite imagery (see Fig. 3.8a,b).

As the MFC spinned up rapidly, the parent cyclone evolved slowly in both its intensity and movement (see Fig. 3.5). The model appears to produce some slight error in the position and the closed circulation of the parent cyclone, likely owing to the specified northern lateral boundary conditions in which much coarser upper-air observations were available for analysis. Nonetheless, the model reproduces well the intense temperature gradients forced along the ice edge over northern Labrador Sea (see Figs. 3.2, and 3.4-3.6). Furthermore, the model mimics the continued deepening of the NFC (cf. Figs. 3.5a,b), which meanders over the Labrador Sea due partly to the larger-scale cyclonic influence and partly to the blocking of the low-level flow by the Greenland topography. Of interest at this time is the emergence of a surface short-wave trough, denoted as "S", to the southeast of the MFC in both the analysis and the simulation. This trough tends to amplify over the baroclinic zone and becomes the third member of the frontal-cyclone family, i.e., the SFC.

In the following 12 h, the MFC deepened even more rapidly than before, i.e., at a rate of 14 hPa/12 h (Fig. 3.1). At 15/00-48, its central pressure dropped to 974 hPa after it propagated to the far east of Newfoundland (Fig. 3.6). It is evident that its associated circulation tended to overpower the remnants of the parent low and the NFC. It is encouraging that the MFC from the 48-h simulation resembles closely that of the CMC analysis in terms of both the intensity and position. In addition, the model replicates very well the cold/warm frontal structures, the thermal ridge wrapping into the cyclone center and the pressure ridge to the north of the cyclone. The model captures too the weakening and wandering nature of both the parent low and the NFC. Besides, it appears to reproduce the intensification of the surface short-wave trough into a closed mesolow, or the SFC ("S"), and its associated cold/warm frontal systems (cf. Figs. 3.6a,b). Some of the discrepancies between the analysis and the simulation could be partly attributed to the lack of appropriate surface observations far offshore. The wavelength of the three-cyclone family is approximately 1000 - 1500 km, much shorter than the one implied by the classical baroclinic theory. The hourly rainfall patterns show again the development of more precipitation to the south along the cold front (Fig. 3.6c). More significant rainfall (2- 3 mm hr^{-1}) occurs to the northwest of the MFC center, which is consistent with the polar-orbiting satellite imagery at 14/18 (cf. Figs. 3.6c and 3.8). An upper-air sounding taken at the cyclone center reveals that all the rainfall is stratiform in nature with cloud tops at about 800-600 hPa (Fig. 3.3b). The sounding structures are quite different from those at the incipient stage of the MFC, which include the presence of weaker vertical shear, more stable and saturated conditions below 800 hPa and less stable above, and a lower tropopause.

At 15/12-60, both the CMC analysis and the 60-h integration show that the MFC has experienced another 6-7 hPa deepening during the previous 12 h and it has almost absorbed the circulations associated with the parent cyclone and the NFC. The MFC becomes a robust oceanic cyclone (Fig. 3.7). The model reproduces very well the basic circulation characteristics of the MFC with respect to its ambient perturbations. Subsequently, the system

a)

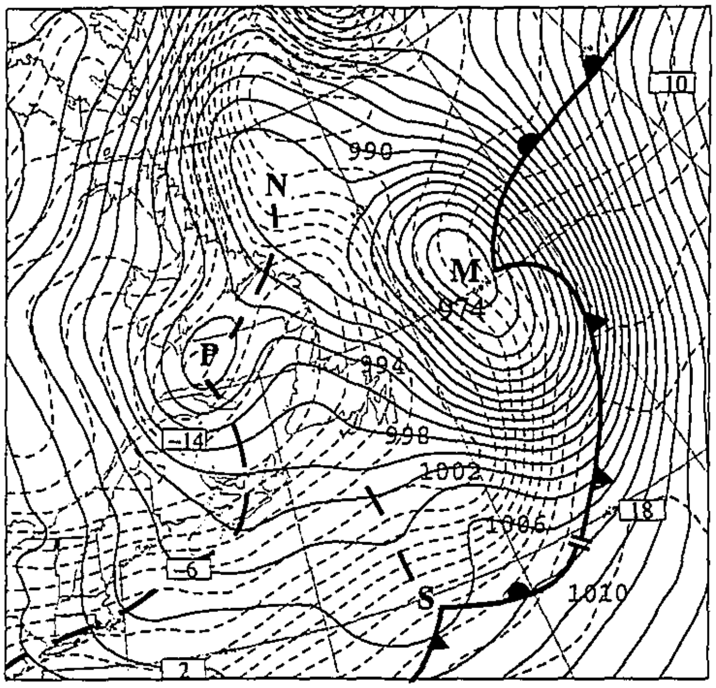

b)

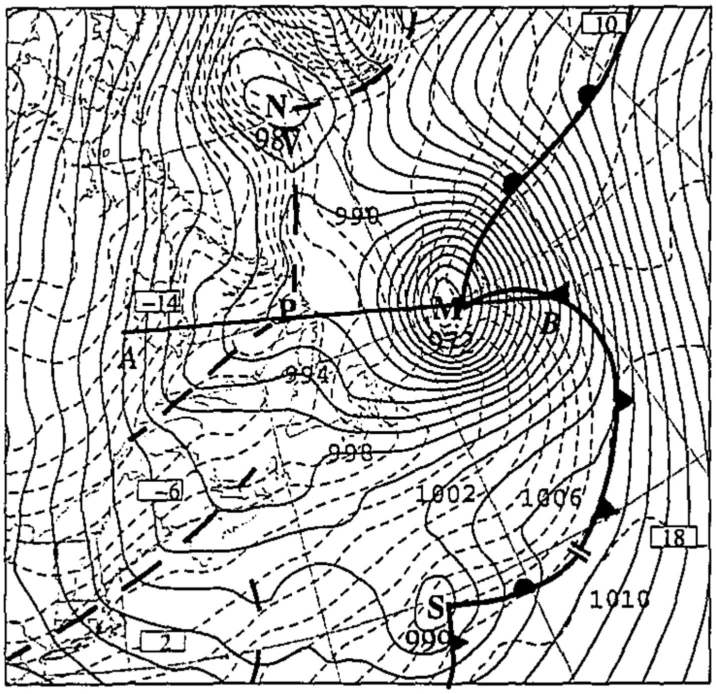

Fig. 3.6 As in Fig. 3.2, but for 0000 UTC 15 March 1992 (15/00-48). Line AB in (b) shows the location of cross section used in Figs. 3.13 and 3.14. Lines CD and EF in (c) show locations of the cross sections used in Figs. 3.15a and b, respectively.

c)

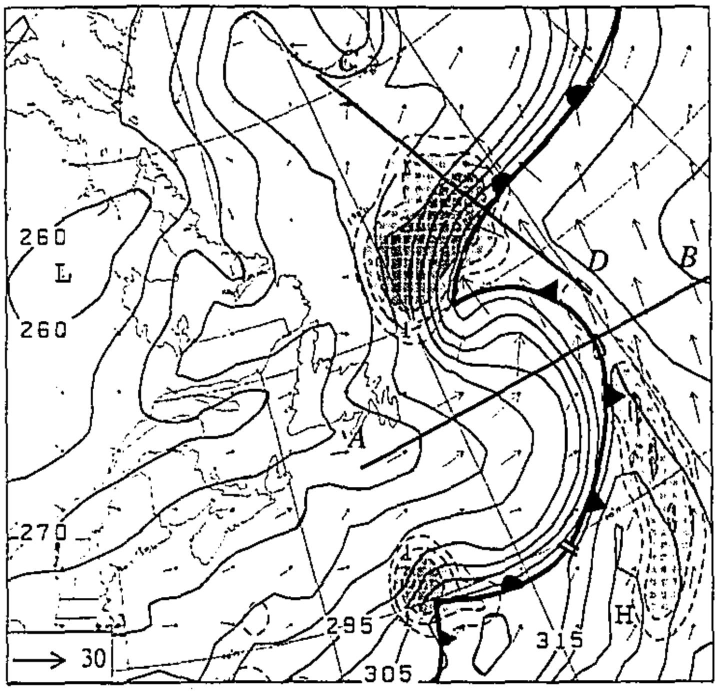

Fig. 3.6 (continued)

began to fill slowly as it continued its northeastward movement. Of particular interest is the development of several short-wave perturbations in the vast cold sector behind the leading primary cold front, as marked by "L_1", "L_2" and "L_3"; they are superposed again with intense thermal gradients (see Figs. 3.5-3.7). These baroclinic perturbations seem to correspond reasonably well to the subsequent three secondary cyclonic developments over the area at 16/12 (see Fig. 3.9). Their lateral dimensions and circulation structures as well as the processes leading to their genesis appear to be similar to those of the NFC and SFC presented above, since they all developed in the same baroclinically unstable basic state and propagated along a similar track northeastward from the offshore of North Carolina.

It is worth noting that the rapid deepening of the MFC and NFC occurs at the expense of the existing available potential energy of the parent cyclone. Specifically, the frontal cyclones tend to gain angular momentum and experience their central pressure drops as they propagate from high- to low- pressure regions, i.e., to the left of the upper-level flow towards the circulation center of the parent cyclone. This is particularly true for the NFC whose central pressure begins near the isobar of 1005 hPa at a distance of 1200 km to the south (see Fig. 2.3b) and ends up with 987 hPa at about 500 km to the northeast of the parent cyclone center (see Fig. 3.6). Therefore, the intensifying mechanisms and characteristics of the frontal cyclones differ from those typical extratropical cyclones as studied by many previous researchers (see the recent reviews by Reed 1990; Hoskins 1990; Uccellini 1990).

3.2 Evolution of upper-level flows

Figures 3.10 and 3.11 show the evolution of the mid-to-upper-level flows within which the above cyclogenesis events take place. At the onset of the MFC's explosive deepening stage, i.e., 14/00-24, the large-scale circulation is still dominated by the parent cyclone to the north, but its filling begins to show up at 850 hPa in terms of its depth, the associated pressure gradient and vorticity concentration (cf. Figs. 2.4 and 3.10). The short-wave disturbance, always having its trough base located at the left entrance region of the upper-level

a)

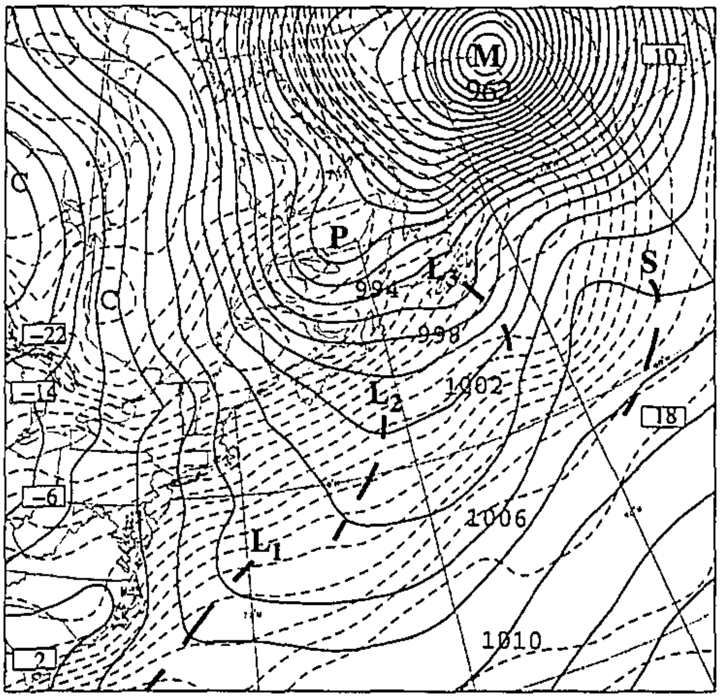

b)

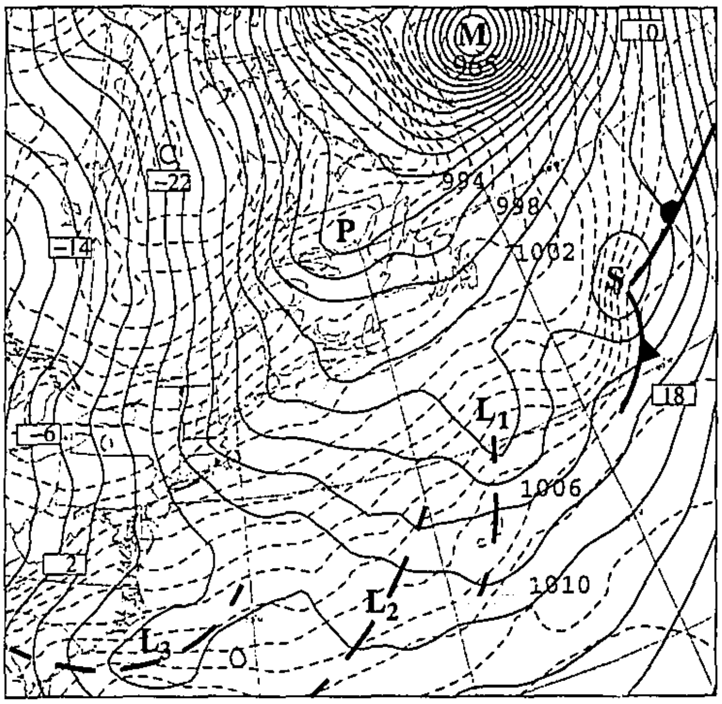

Fig. 3.7 As in Figs. 3.2 a,b, but for 1200 UTC 15 March 1992 (15/12-60). Letters, "L_1", "L_2" and "L_3" denote the formation positions of new frontal cyclones.

a)

b)

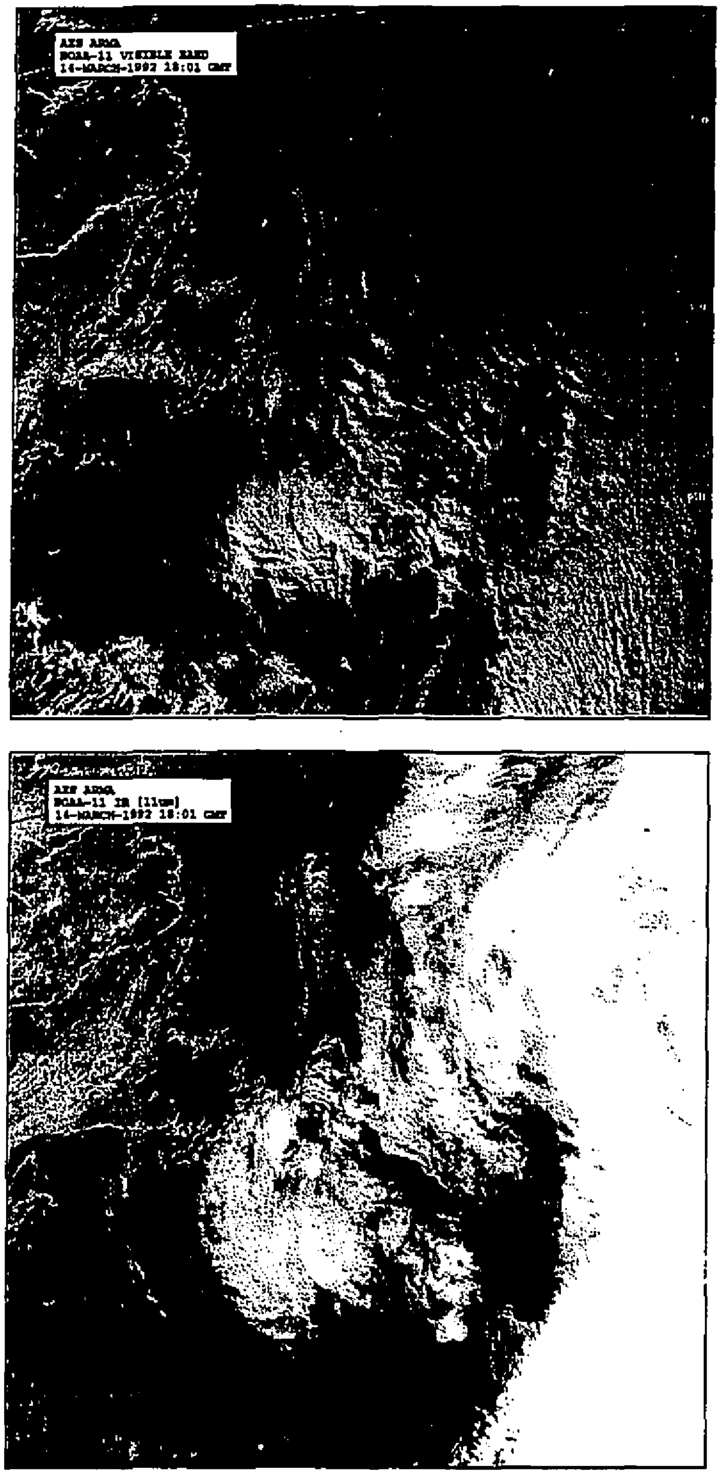

Fig. 3.8 a) Visible; and b) infrared satellite imagery at 1801 UTC 14 March 1992. Location of the MFC is marked by "M".

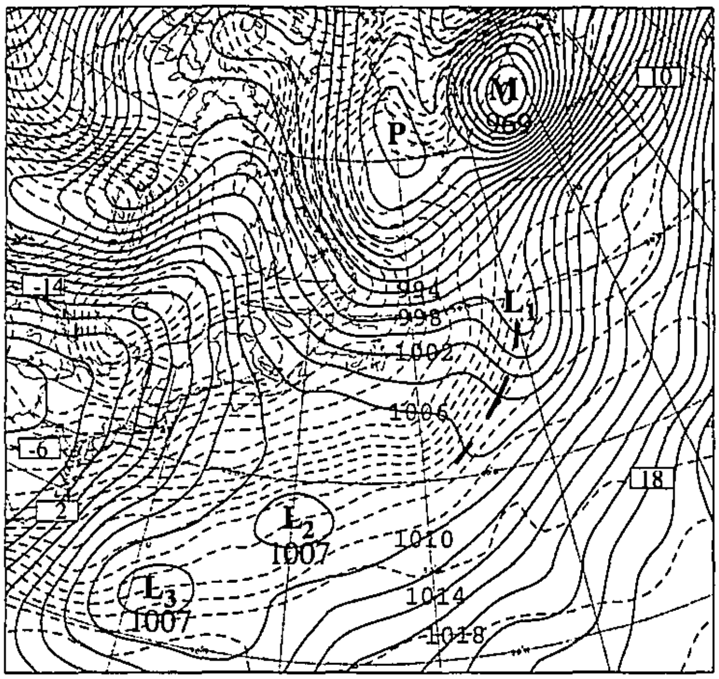

Fig. 3.9 As in Fig. 3.2a but for the CMC analysis at 1200 UTC 16 March 1992. Letters, "L_1", "L_2" and "L_3" denote newly formed frontal cyclones.

jet streak, moves slowly eastward. We will see in section 3.4 that this trough is closely related to a potential vorticity (PV) center associated with the tropopause depression that is enhanced by the direct secondary transverse circulation in the left entrance region of the jet streak. As this PV anomaly is advected downstream along the near-straight jet streak, the associated curvature vorticity decreases so that the trough loses its identity with time. In contrast, two new mesoscale perturbations, induced by the MFC ("M") and the NFC ("N"), become visible in both the height and temperature fields up to 500 hPa (cf. Figs. 3.4 and 3.10). Their related cross-isobaric flows toward lower pressure are also evident, more pronounced in the case of the MFC-induced perturbation. Of particular importance is that the broader area of height deficit induced by the MFC is favorably juxtaposed with the existing thermal structure (e.g., Fig. 3.10c). Specifically, as the MFC propagates rapidly into the slowly evolving low-level baroclinic zone, a pronounced phase lag develops between the thermal trough and the newly formed height trough such that an extensive area of marked cold advection appears to the rear of the MFC. This scenario occurs because the movement of the MFC is strongly influenced by a PV anomaly near the tropopause, as will be seen in section 3.4, whereas that of the thermal trough is mainly determined by the advective process. Zhang and Harvey (1995) have shown how a favorable phase relationship between the pressure and thermal waves can be established when a convectively enhanced midlevel trough and a thermal wave propagate at different speeds. In the present case, such a baroclinic set-up clearly provides a positive feedback to the cyclogenesis, perhaps assisting the subsequent explosive deepening of the MFC. However, this mesocyclonic influence decreases with height. At 250 hPa, the basic flow is still dominated by the jet streak and the parent cyclone, although both have weakened, with little evidence of the secondary development (cf. Figs. 2.4a and 3.10a). The MFC is still located near the core of the jet streak on its cyclonic side.

By 15/00-48, the westerly jet streak has weakened from 75 m s^{-1} to about 60 m s^{-1} during the previous 48 h, and its movement slows as it propagates toward a large-scale ridge ahead (see Fig. 3.11a). This allows the MFC to advance quickly into the far left exit region of

a)

b)

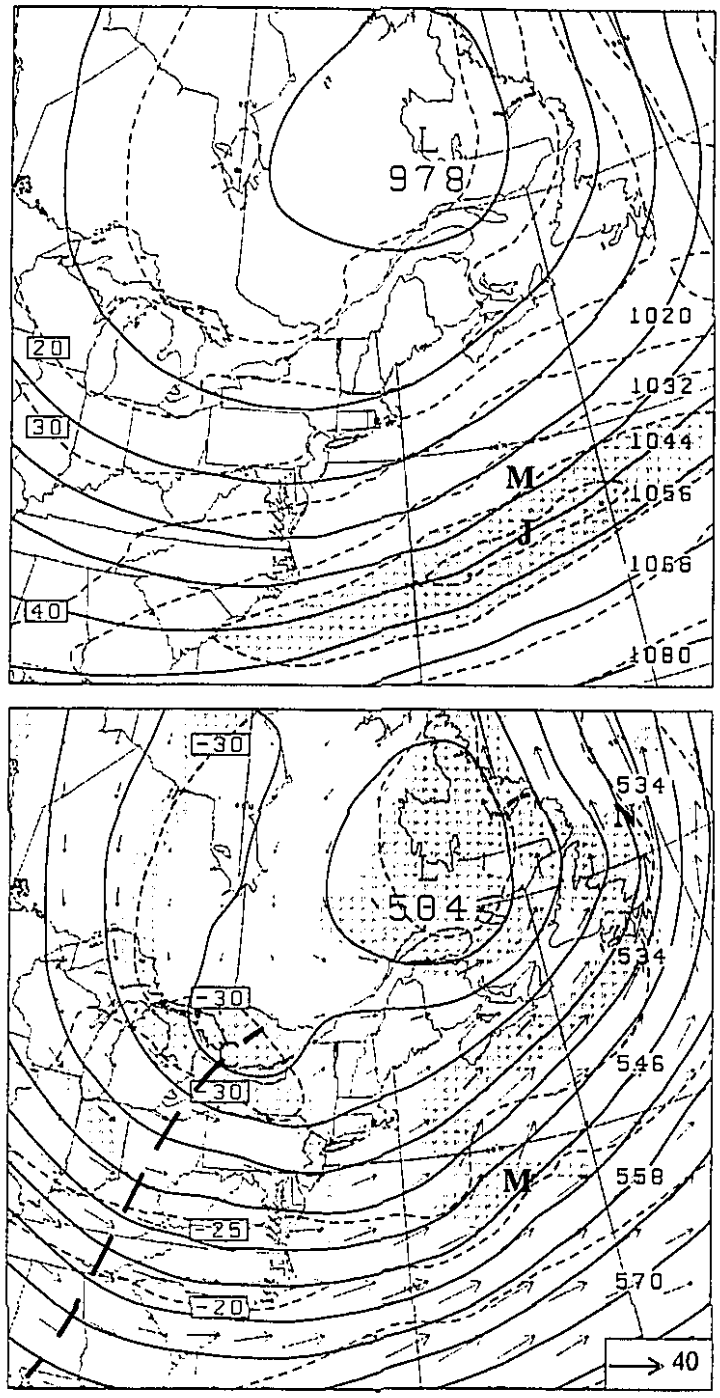

Fig. 3.10 As in Fig. 2.4, but from 24-h control simulation (14/00-24). Locations of the surface parent, major and northern frontal cyclones are marked by letters "P", "M" and "N", respectively. Inset indicates the scale of horizontal wind speed (m s^{-1}).

c)

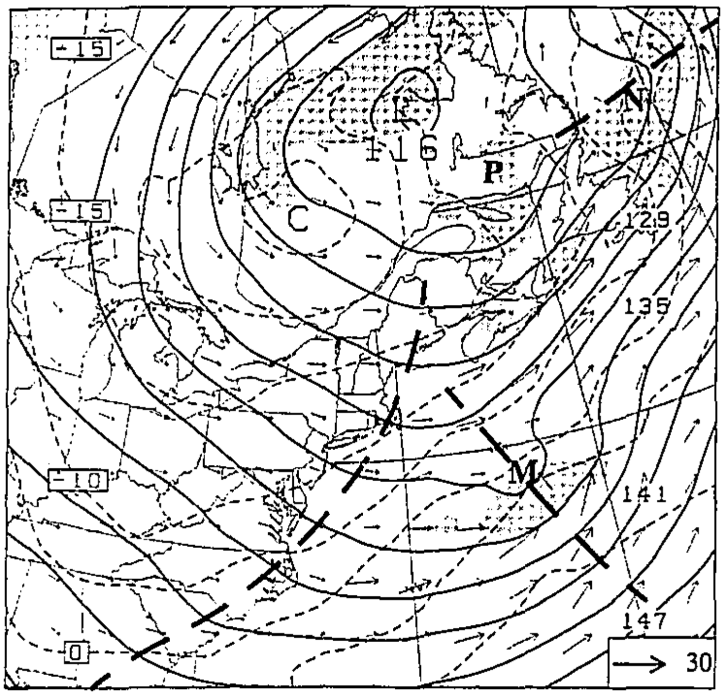

Fig. 3.10 (continued)

a)

b)

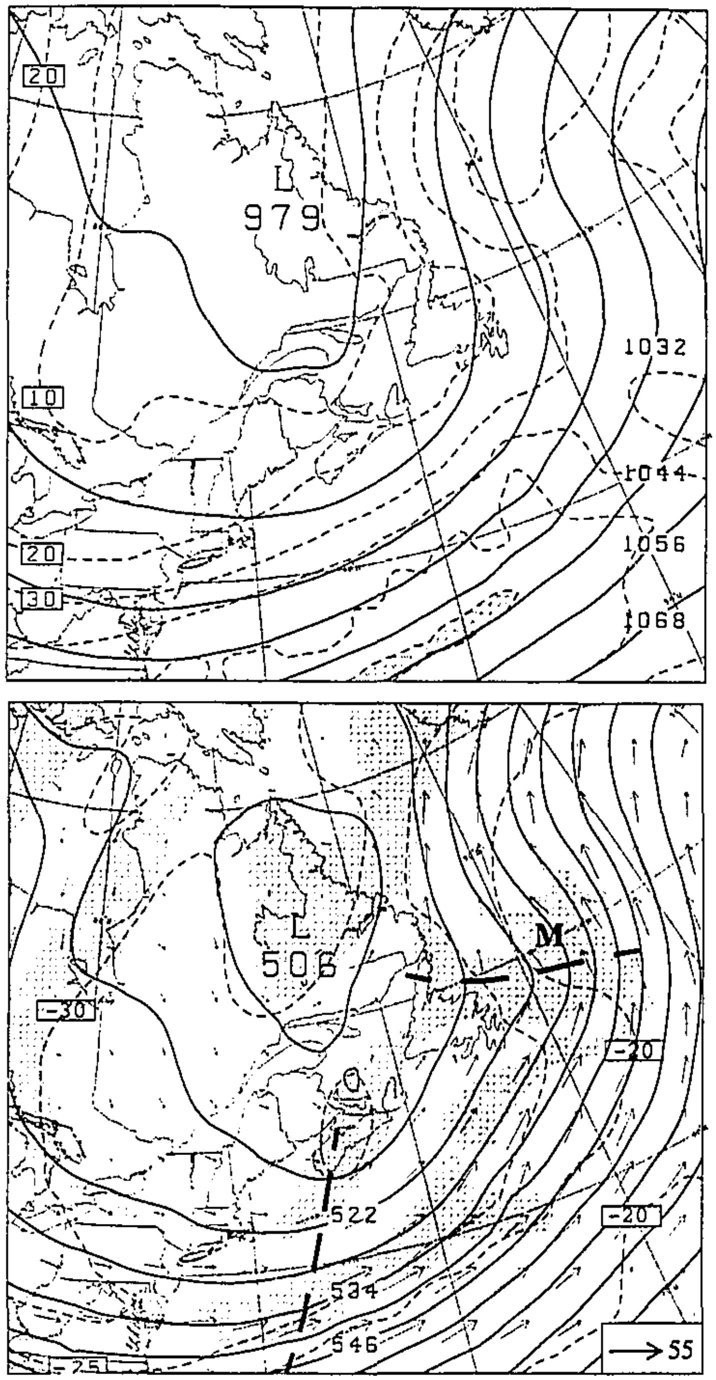

Fig. 3.11 As in Fig. 2.4, but from 48-h control simulation (15/00-48). Locations of the surface parent, major , northern, and southern frontal cyclones are marked by letters "P", "M", "N" and "S", respectively. Inset indicates the scale of horizontal wind speed (m s^{-1}).

c)

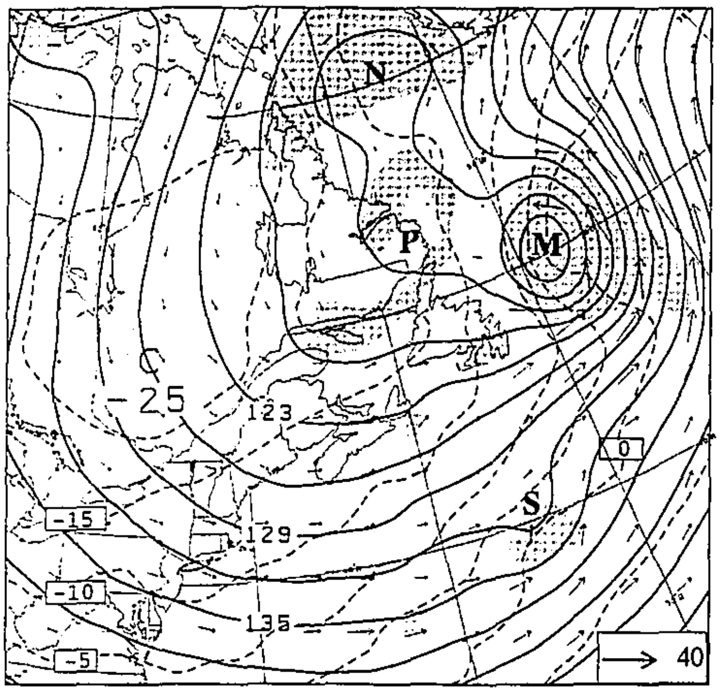

Fig. 3.11 (continued)

the jet streak after 14/00-24. Thus, unlike the case studied by Uccellini and Kocin (1987), the jet-streak induced ageostrophic circulation does not seem to have direct influence on the deepening of the MFC; however, it has an indirect effect on the cyclogenesis through the enhancement of the upper-level PV anomalies, as will be discussed in section 3.4. At this mature stage, the MFC generates closed circulations at 850 hPa and begins to dominate the parent cyclone and the NFC, just like what happens at the surface. Moreover, the wind-thermal configuration exhibits intense cold (warm) advection behind (ahead of) the system, which is instrumental in the baroclinic conversion of available potential energy into kinetic energy. Thus, the MFC induces intense cross-isobaric winds up to 500 hPa which are in significant contrast with the benign flows in the vicinity of the other two remnant systems. Note that a well-developed thermal ridge extends towards the MFC center (Figs. 3.11b,c), which can be regarded as equivalent to a positive PV-anomaly contribution to the genesis of the system, from a PV-inversion viewpoint (Davis and Emanuel 1991).

3.3 Vertical baroclinic structures

To gain additional insight into the baroclinic structures of the various types of cyclones, Figs. 3.12 and 3.13 show the vertical cross section of height and temperature deviations, superimposed with along-plane wind vectors, through their centers at 14/00-24 and 15/00-48, respectively. All deviations are obtained by deducting their pressure-level averages in the cross section. The pressure trough associated with the MFC exhibits the typical westward tilt up to 700 hPa. Higher up, the cyclonic circulation of the parent cyclone prevails with strong vertical shear; again there is little vertical tilt (Fig. 3.12a). Flow vectors show evidence of warm advection along the warm front and across the MFC center in the lowest 200 hPa, and a deep layer of moderate cold advection above from the west. This tends to tighten the isotherms and statically destabilize the atmospheric columns near the MFC center. On the other hand, the northward advection of high-θ_e air in the warm sector leads to the development of near-saturated updrafts and intense precipitation across the warm front.

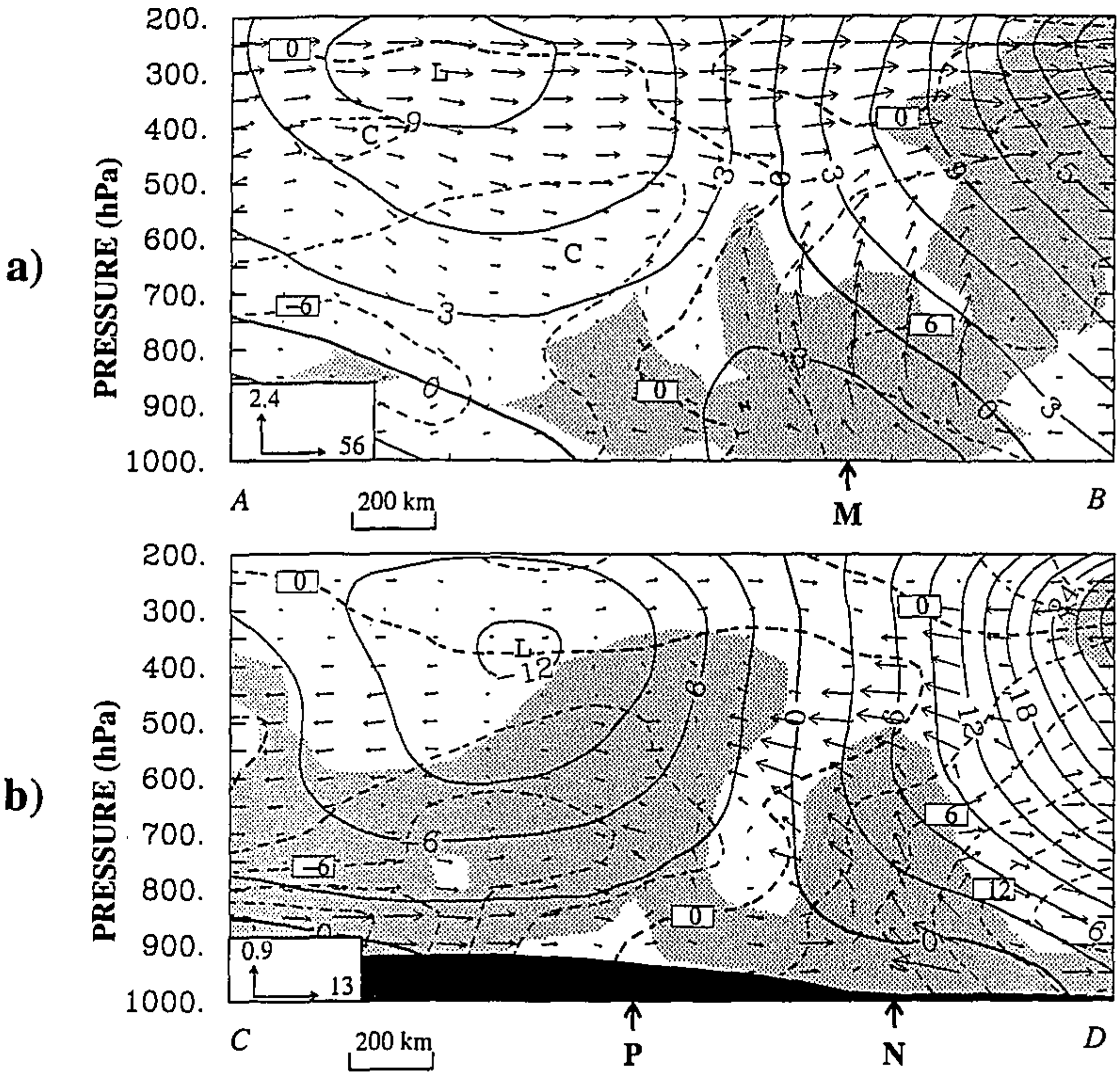

Fig. 3.12 Vertical cross section of height deviations (solid) at intervals of 3 dam and temperature deviations (dashed) at intervals of 3 °C, superposed with along-plane flow vectors, which is taken along line a) AB; and b) CD given in Fig. 3.4b from 24-h control simulation. Inset shows the scale of vertical (Pa s^{-1}) and horizontal motion (m s^{-1}). Locations of the surface low pressure centers are indicated on the abscissa. Shading denotes relative humidity > 90%.

Similar but much shallower vertical circulations occur in association with the NFC (see Fig. 3.12b). This implies that both the MFC and the NFC are in favorable environments for cyclonic development, at least with the upper-level cyclonic influence and the available latent heating in the lower to middle troposphere.

In contrast, the parent cyclone is characterized by a vertically coherent trough structure with little horizontal movement (see Figs. 3.12b and 3.10). Strong cold advection occurs only in the lowest 200 hPa from the northwest (cf. Figs. 3.4b and 3.12b). Higher up, a deep layer of (two-dimensional) divergence is present, as implied by the outward flow vectors away from lower heights around the system. These features are all consistent with the slow filling of the parent cyclone during the study period. In addition, the propagation of the NFC into Labrador Sea tends to block the source of warm and moist air from the warm sector, and thus deprives the parent cyclone of access to the available potential energy through latent heat release.

By 15/00-48, the parent cyclone loses its indentity from its surface circulation (Fig. 3.6). This appears to result from the advection of colder polar air mass into the cyclone center under the influence of both the NFC and MFC. As a result, the closed circulation of the parent cyclone becomes elevated with time (Figs. 3.13 and 3.14). At this stage, more intense cyclonic circulation, particularly in the lowest 300 hPa, occurs in the vicinity of the MFC. Strong cross-isobaric convergence into the MFC center, as revealed by flow vectors, leads to the marked concentration of cyclonic vorticity up to 600 hPa through vortex stretching (cf. Figs. 3.13 and 3.14). This convergence also tightens substantially isotherms in a deep layer, with cold (warm) advection behind (ahead of) the MFC (see Figs. 3.11, 3.13 and 3.14). Clearly, the intensifying thermal advection tends to increase the baroclinic conversion from available potential energy to kinetic energy, which is consistent with the rapid intensification of low-level winds and cyclonic vorticity during this period (Fig. 3.14).

Note that the cyclonic vorticity, convergence zone and trough axis associated with the MFC all tilt upshear, as for a typical baroclinic unstable wave. Of particular interest is that the

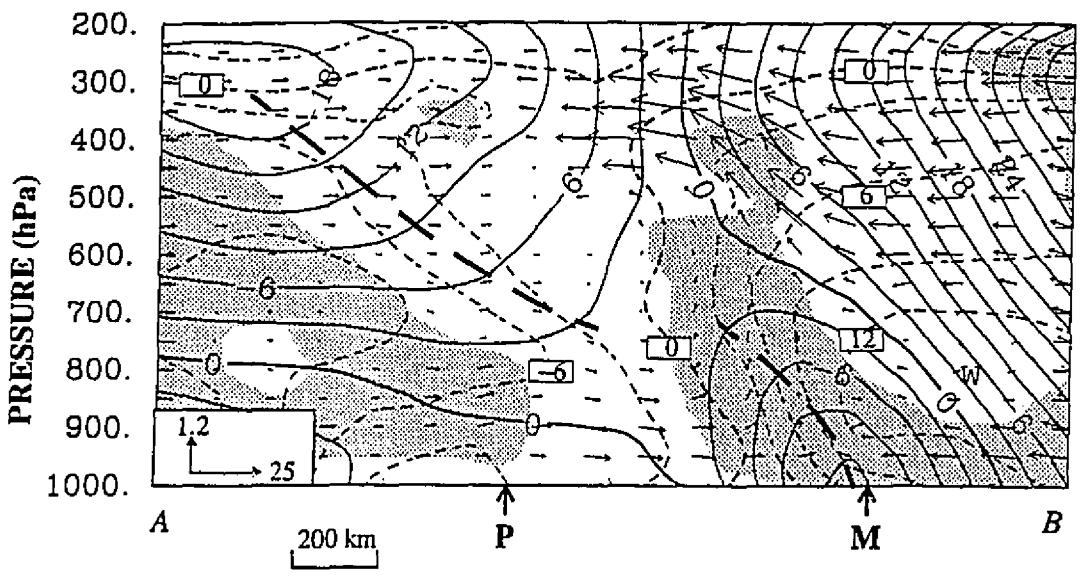

Fig. 3.13 As in Fig. 3.12,but from 48-h control simulation along the line AB given in Fig. 3.6b. Thick dashed lines represent the subjectively analyzed height troughs in the plane.

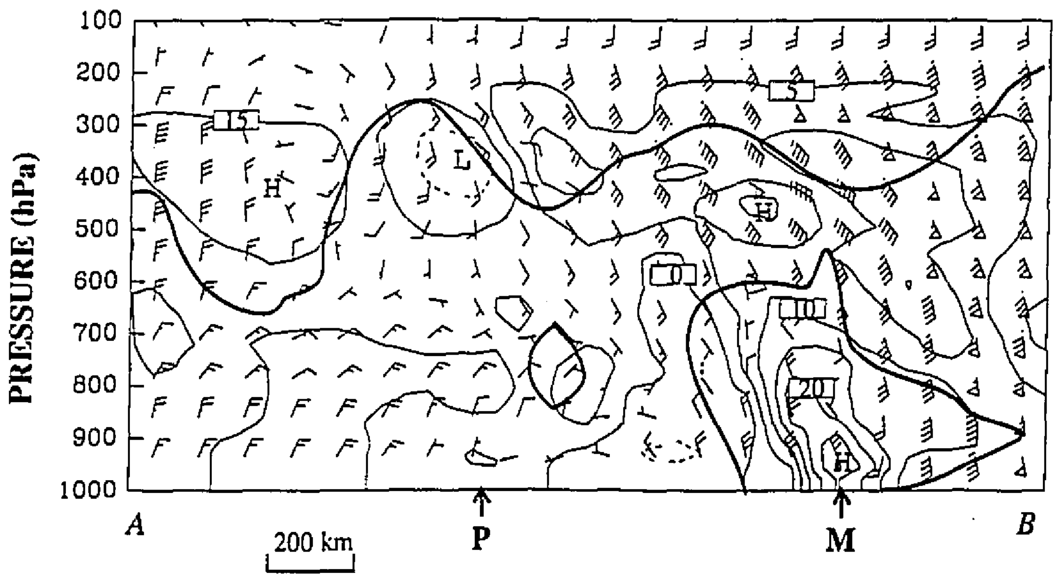

Fig. 3.14 Vertical cross section of relative vorticity (solid/positive, dashed/negative) at intervals of $5\times10^{-4}\ s^{-1}$ superposed with wind barbs from 48-h control simulation, taken along line AB given in Fig. 3.6b. Thick solid line represents PV of 2 PVU. Winds are plotted in the same manner as in Fig. 3.3. Locations of the primary and major cyclone centers are denoted by letters "P" and "M", respectively.

parent cyclone contributes little, through differential vorticity advection, to the deepening of the MFC, since the parent vorticity center at 400 hPa occurs to the far west of the MFC (Fig. 3.14). Rather, a deep layer (i.e., from 700 to 300 hPa) of cyclonic vorticity is advected into the MFC region from behind by intense southwesterly flows (20 - 30 m s^{-1}). As will be shown in the next subsection, this positive vorticity layer corresponds to a high-PV ring of the tropopause depression on the cyclonic side of the upper-level jet streak. Note also the near-saturated slantwise ascent that occurs up to 350 hPa in the vicinity of the MFC (cf. Figs. 3.6c and 3.13). This slantwise ascent draws high-θ_e air from the boundary layer in the warm sector where little or no upward motion is present, and then lifting to saturation takes place in the convergent flow and the instability is released. It is evident that latent heat release must play an important role in the rapid deepening of the MFC and the other two secondary frontal systems, since more intense precipitation occurs in close proximity to their centers (Hack and Schubert 1986).

To facilitate the understanding of moist dynamical processes of the frontal cyclogenesis compared to typical baroclinic development, Figs. 3.15a,b show vertical structures of cross-frontal flows and thermodynamic conditions across the cold and warm fronts of the MFC during its mature stage. The cold front is characterized by a deep layer of descent to its rear, a sharp change to ascent along the near-upright frontal zone, an intense updraft in a narrow zone ahead and a weak vertical motion in the warm sector. The θ_e-structure exhibits the presence of potential instability ahead of the cold front, and it is released partly near the frontal zone in the form of deep convection. As mentioned previously, the potential instability is established as a result of the transport of tropical high-θ_e maritime boundary-layer air by the low-level intensifying flow that is enhanced by upward sensible and latent heat fluxes from the warm ocean (see Fig. 3.6c). In this respect, Hedley and Yau (1991) showed an example of a numerical simulation with idealized initial conditions on how an imposed warm sea-level thermal anomaly can generate a potentially unstable environment in the warm sector.

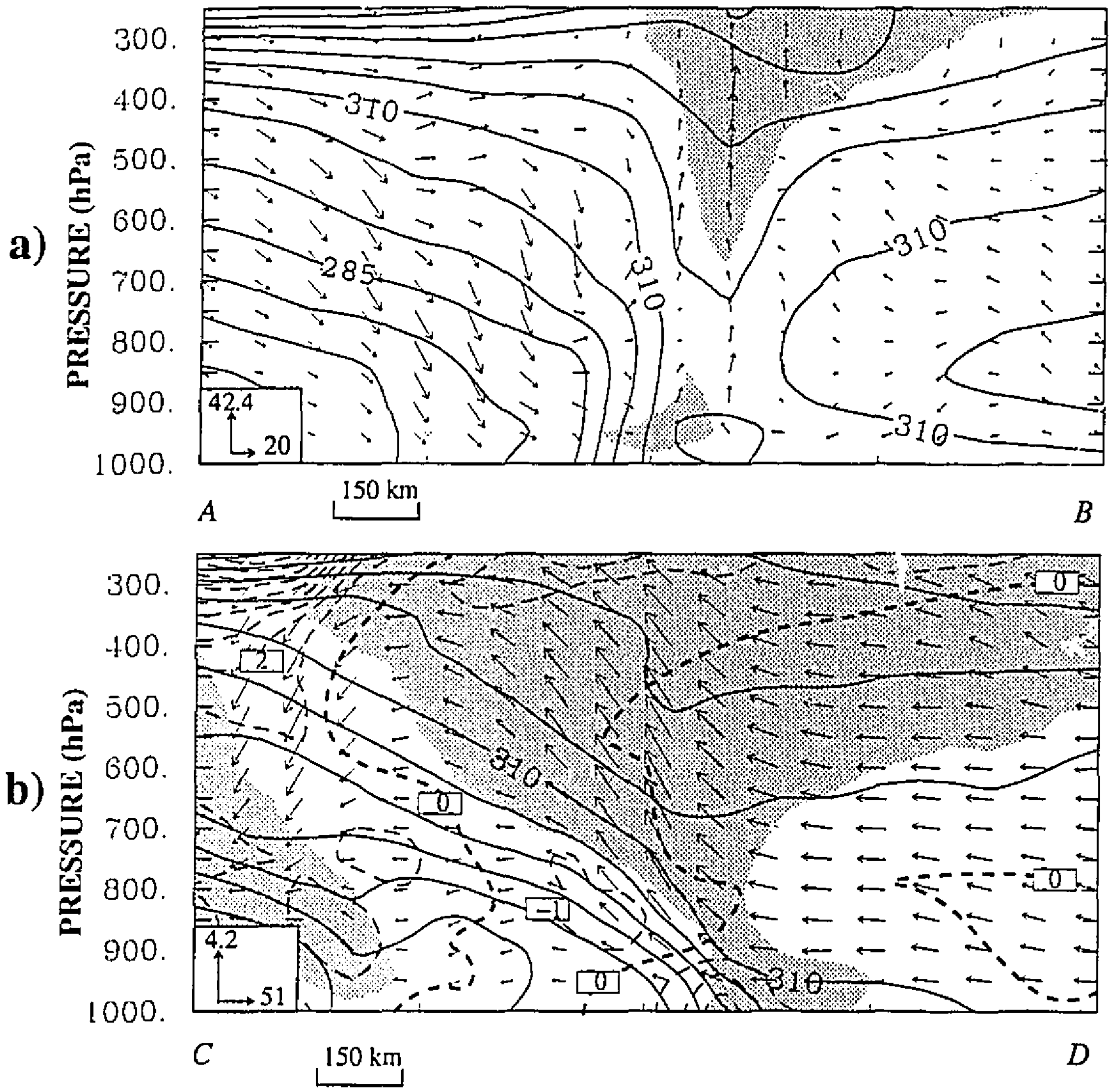

Fig. 3.15 Vertical cross section of equivalent potential temperature θ_e (solid) at intervals of 5 K, superposed with flow vectors, from 48-h control simulation along line a) AB and b) CD given in Fig. 3.6c. Thick dashed lines denote areas with negative moist potential vorticity. Shading denotes relative humidity > 90%. Insets indicate the scale of vertical motion (Pa s^{-1}) and horizontal wind speed (m s^{-1}).

Note the quite different low-level θ_e profiles across the cold front, i.e., a deep well-mixed θ_e layer (up to 800 hPa) behind the front that is generated by strong upward surface fluxes of sensible and latent heat in the cold air mass overlying the warm ocean water, and a shallow layer of the stratified warm air mass ahead with little horizontal thermal gradient and little vertical coupling except in the intense updraft zone.

While potential instability of the environment accounts for the development of *upright* convection along the cold front, *slantwise* convection appears to be the mechanism by which latent heat is released along the warm front. For this purpose, moist potential vorticity (MPV) is plotted; it is defined as:

$$\mathrm{MPV} = \left[\frac{\partial\theta e}{\partial x}\left(\frac{\partial w}{\partial y} - \frac{\partial v}{\partial z}\right) + \frac{\partial\theta e}{\partial y}\left(\frac{\partial u}{\partial z} - \frac{\partial w}{\partial x}\right) + \frac{\partial\theta e}{\partial z}\left(\frac{\partial v}{\partial x} - \frac{\partial u}{\partial y} + f\right)\right]/\rho \qquad (3.1)$$

where u, v and w are the wind speed along x, y and z directions, respectively; θe is the equivalent potential temperature; f is the Coriolis parameter; and ρ is the density of the air. One can see that there is little or no upward motion in the warm sector but strong sloping ascent along the well-defined warm frontal zone. This suggests that the potentially unstable air is being transported by the southerly flow into the frontal zone, where lifting to saturation occurs and the instability is released. Since the region of ascent (up to 300 hPa) is close to saturation, the nearly-zero to negative MPV implies the presence of moist symmetric instability in the sloping flow, as has also been noted by Kuo and Reed (1988); Reuter and Yau (1990); Huo et al. (1995) and others.

3.4 Vertical potential vorticity structure

In this section, we use the dynamic variable, potential vorticity (PV), to gain insight into the vertical interactions of upper- and lower-level disturbances. PV is defined in the same way as MPV except for replacing θe in Eq. (3.1) with θ. PV has many useful properties, such as its conservation following three-dimensional, adiabatic, inviscid motion (Rossby 1940; Ertel 1942) and its invertibility to recover three-dimensional winds from a given mass field. Its invertibility also makes it possible to quantify the different roles of diabatic processes and the low- versus upper-level disturbances in cyclogenesis. For instance, Reed et al. (1991) simulated a marine cyclone that developed in a strong baroclinic area with anomalously high PV along the east coast of the US. They identified three main types of PV contributing to the positive anomaly: i) PV with its origin in the upper troposphere or lower stratosphere associated with the tropopause depression; ii) low- to midlevel PV produced by condensation in the precipitating clouds; and iii) surface warm anomaly in the potential temperature equivalent to a concentrated surface PV anomaly (Bretherton 1966). In this section, we study the distribution and development of PV, following Reed et al. (1993), in order to address the roles of upper-level PV anomalies in the multiple secondary cyclogenesis events.

For this purpose, Figs. 3.16 - 3.18 show the horizontal evolution of PV at 400- and 900-hPa as well as vertical cross sections of PV and flow vectors. The vertical cross sections are taken roughly along the 400-hPa flows through the upper-level PV and the surface cyclone centers, in order to examine the vertical coupling of PV anomalies. At the incipient stage of the MFC, i.e., at 13/12-12, there is little low-level PV over the secondary genesis regions and the major PV concentration is associated with the parent cyclone over northern Quebec. By comparison, the upper-level PV is characterized by a ring of high PV exceeding 4 PVU (1 PVU = 10^{-6} m^2 K s^{-1} kg^{-1}) at the cyclonic side of the jet stream, with near-zero PV in the central weak-flow region. If a typical value of 2 PVU is used to define the "dynamic" tropopause, this ring of upper-level PV anomalies is indicative of tropopause depression - a process of dry and warm intrusion of the stratospheric air. This PV ring is found to form as a consequence of the development of the parent cyclone. Specifically, the parent cyclone deepens as an upper-level PV anomaly associated with a short-wave trough is advected cyclonically towards its surface low, and then it fills as the PV anomaly is advected downstream (e.g., Reed et al. 1991; Huo et al. 1995). Thus, this PV ring represents the interface between the polar air mass in the central weak-flow area and the tropical air mass

a)

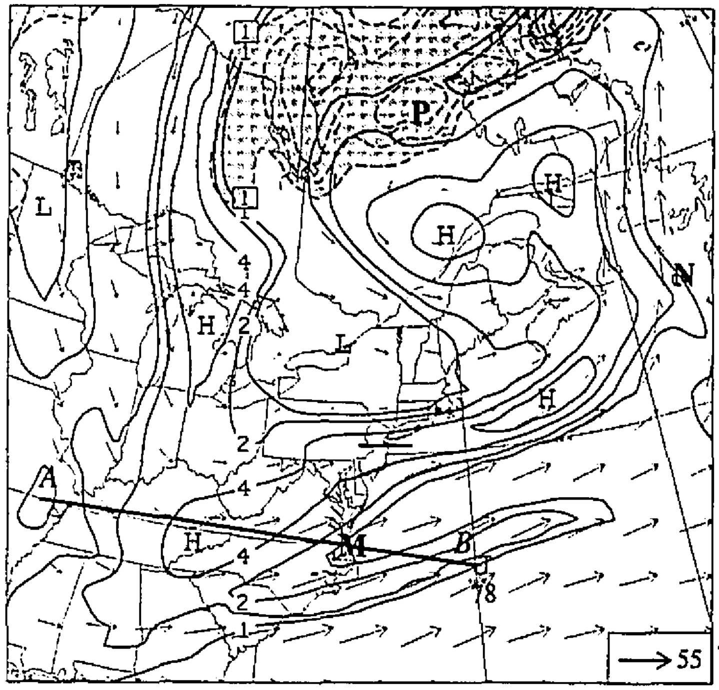

b)

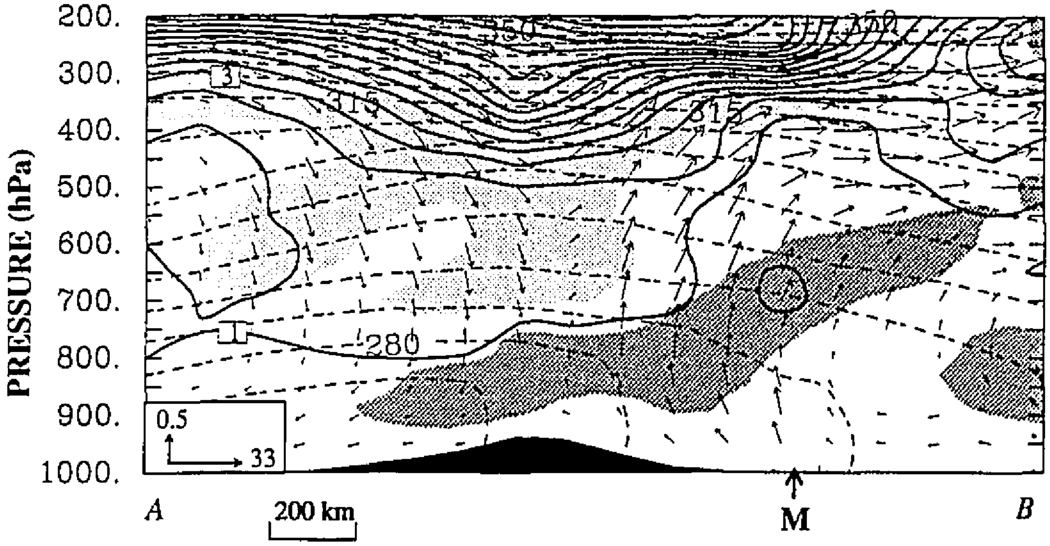

Fig. 3.16 a) Distribution of 400-hPa PV (solid) with contours of 1, 2, 4 and 6 PVU and 900-hPa PV (dashed) at intervals of 1 PVU, superposed with 400-hPa wind vectors from 12-h control simulation (13/12-12); b) Vertical cross section of PV (solid) at intervals of 1 PVU and potential temperature θ (dashed) at intervals of 5 K, superposed with flow vectors, along line AB given in (a). Light (dark) shading denotes relative humidity < 30% (> 90%). Letters 'M', 'N', 'P', 'J' and 'H' denote the centers of the surface major, northern and parent frontal cyclones, 250-hPa jet streak and local maxima of 400-hPa PV. Inset indicates the scale of vertical motion (Pa s^{-1}) and horizontal wind speed (m s^{-1}).

outside. It is of interest to note that the track of the MFC during the 6-day period resembles extremely well the distribution of the PV ring, indicating at least the steering role of the upper-level PV anomalies in the propagation of the MFC as well as the NFC and SFC.

Note the PV ridge along the mid-Atlantic states that corresponds exactly to the secondary short-wave trough at the incipient stage of the MFC (cf. Figs. 2.4 and 3.16a); the pre-MFC is located about 700 km downstream. A vertical cross section through the upper-level PV and the pre-MFC centers shows that the dynamic tropopause is seen descending to 500 hPa behind the short-wave trough axis and then advected toward the pre-MFC, as also evidenced by the low relative humidity down to 700 hPa (Fig. 3.16b). Of particular importance is that the stratospheric subsidence is caused by the ageostrophic convergence in the left entrance region of the upper-level jet streak (Uccellini et al. 1985). Thus, the intensity of the short-wave trough and its associated PV anomaly depends on their relative positions with respect to the jet streak. This appears to explain why the trough moves slowly eastward and weakens as does the jet streak.

Because the upper-level PV anomaly is being advected eastward at a rate faster than the surface system, it begins to overtake the pre-MFC at 13/12-12, leading to surface pressure fall (cf. Figs. 2.3 and 3.2), an increase of the low-level convergence (Fig. 3.16b) and the formation of a closed mesolow (i.e., the MFC) soon afterward. This process is very similar to that described by Hoskins et al. (1985) in which an upper-level PV anomaly overruns a low-level baroclinic zone, causing the spin up of a surface cyclone. Thus, 13/12-12 marks the beginning of the more direct influence of the upper-level PV anomaly on the surface cyclogenesis. Prior to this time, the low- and upper-level interaction may not affect the surface development, perhaps and more importantly, owing to the lack of ample moisture for latent heat release. More rapid genesis of the MFC occurs 6 hours later, when intense precipitation occurs in the vicinity of the cyclone center (see Fig. 3.4) as a consequence of the enhanced low-level cyclonic circulation and convergence.

By 14/00-24, a low-level PV anomaly, resulting mostly from latent heating in the slantwise ascent (cf. Figs. 3.4 and 3.17), appears just near the leading edge of the upper-level PV ring. The development of PV anomaly by latent heating has been discussed extensively by Bosart and Lin (1984), Boyle and Bosart (1986), Whitaker et al. (1988), Davis and Emanuel (1991) and others. Of our interest is that this heating-induced PV anomaly, confined completely in the cloud region with relative humidity greater than 90%, is well "locked" with the upper-level PV anomaly (Fig. 3.17b). This vertical coupling coincides with the rapid deepening of the MFC, indicating the importance of the low- and upper-level interactions in the secondary cyclogenesis. Unlike other cyclogenesis cases in which the tropopause depression intensifies concurrently with surface development (e.g., Huo et al. 1995), the upper-level PV anomaly behind the MFC become less organized than that at earlier hours after the system propagated into the left exit region of the jet streak. This is caused by the jet-streak indirect transverse circulation that tends to lift, though slowly, the dynamic tropopause upward (cf. Figs. 3.16b and 3.17b). On the other hand, a PV-poor region is seen to the north of the MFC (Figs. 3.17a,b), which corresponds to the slantwise ascent along the warm frontal zone. This PV-poor region is produced partly by the upward lifting of the tropopause and partly by the vertical advection of negative PV above the level of maximum heating.

At 15/00-48, a "comma-shaped" low-level PV, peaked at 950 hPa, develops in the vicinity of the MFC, with its maximum value exceeding 9.5 PVU near the cyclone center (Fig. 3.18). Again, this low-level PV concentration is well "locked" with the upper-level PV anomaly. Note that a warm-core thermal structure occurs up to 300 hPa near the MFC center; its northeastward tilt is caused by the cross section that is taken through both the cold and warm frontal zones of the system. This warm anomaly results from both the diabatic heating and the warm advection in the slantwise ascent. Note also that the MFC is always located downstream of the 400-hPa PV reservoir at its leading edge; so the upper-level PV-rich air could be effectively advected into the MFC center to feed the surface development.

a)

b)

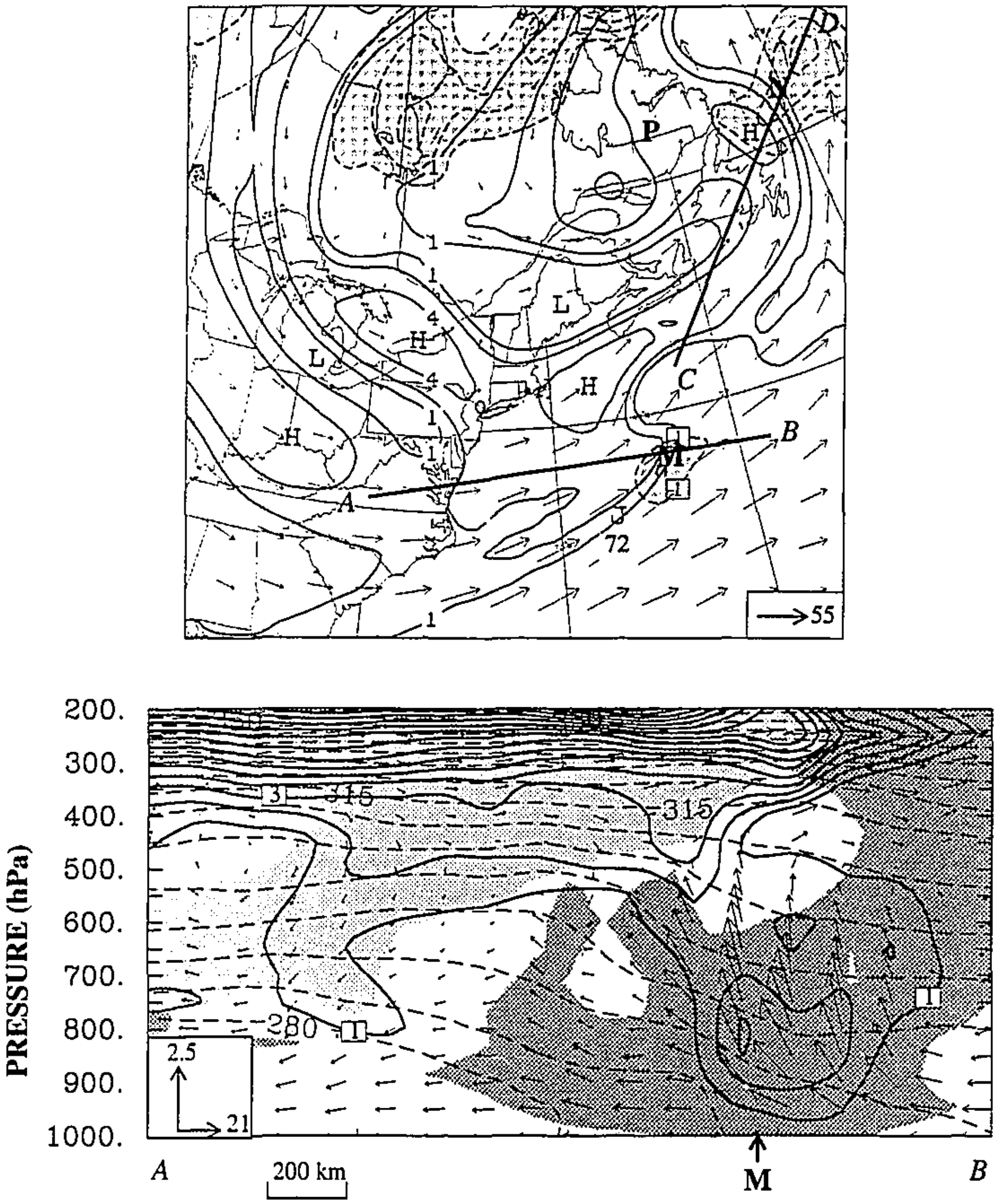

Fig. 3.17 As in Fig. 3.16, but from 24-h control simulation (14/00-24).

a)

b)

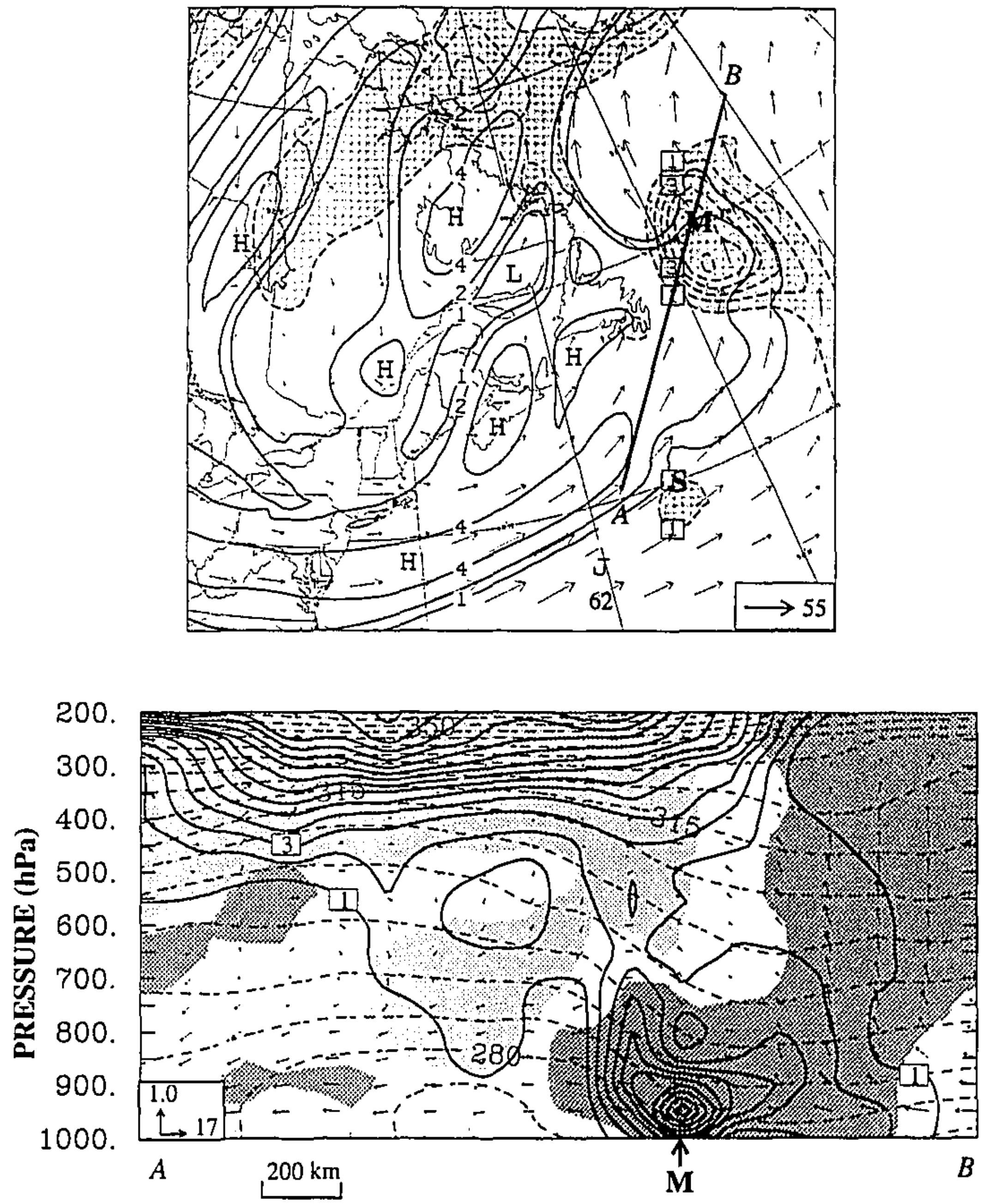

Fig. 3.18 As in Fig. 3.16, but from 48-h control simulation (15/00-48).

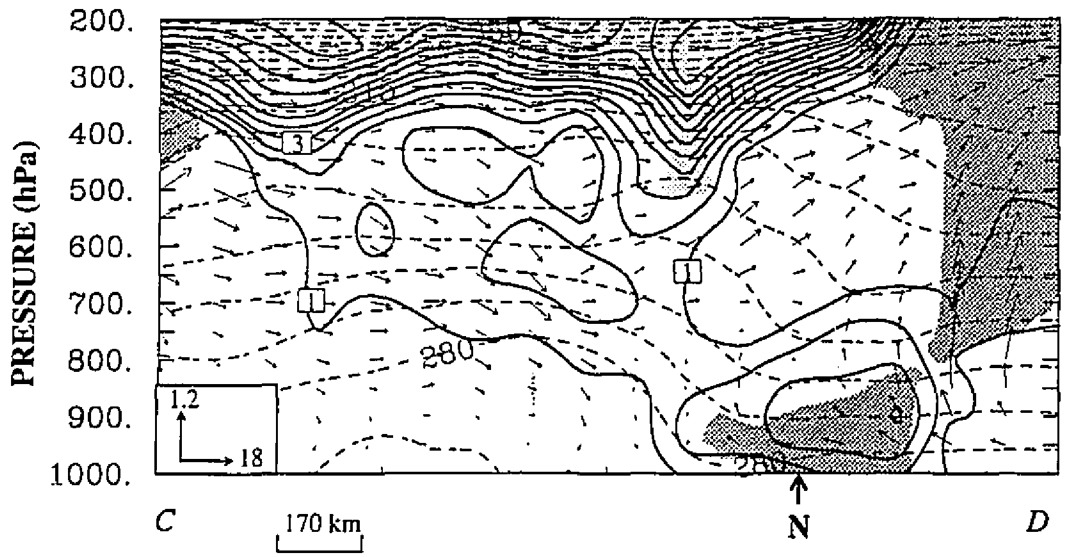

Fig. 3.19 As in Fig. 3.16b, but for the cross section taken along the line CD in Fig. 3.17a.

Finally, it is worth noting that the NFC and SFC also intensify under the favorable influence of upper-level PV anomalies, but at the lateral periphery rather than downstream of the PV ring. For example, Figs. 3.17a and 3.19 do show the vertical coupling of the low- and upper-level PV anomalies associated with the NFC at 14/00-24; similarly at other hours. However, this vertical "locking" is not as effective as it is in the case of the MFC, owing to the lack of the continued advection of upper-level higher PV from behind into the NFC. Furthermore, since both the NFC and SFC intensify in the left exit region of the jet streak, the tropopause tends to be elevated with time, producing less influence on the deepening of the systems. Still further, because both systems begin their amplification closer to the primary cold frontal zone with weaker baroclinicity than the MFC (cf. Figs. 3.2 and 3.5), less available potential energy could be converted to kinetic energy for baroclinic growth. Thus, the NFC and SFC could not grow into systems as "robust" as the MFC.

Chapter 4 Sensitivity Analysis

After showing in the preceding chapter that the MM4 reproduces very well the structures and evolution of the frontal cyclogenesis family over the western Atlantic ocean, it is possible to use that simulation as a control run (Exp. CTL) to investigate the model sensitivity to different physical processes. In particular, we have seen that the secondary cyclogenesis family develops as a result of the interactions between diabatic heating, the low- to mid-level thermal advection, and the upper-level forcing associated with the tropopause depression. Thus, sensitivity runs could be conducted to isolate and quantify the contribution of each of these processes to the secondary developments at different stages of their life cycles. Furthermore, understanding the impact of various physical processes on the simulated track, structure and evolution of the secondary frontal systems will help us identify the necessary ingredients for a successful simulation of the storms. Our analysis is performed through the diagnostics of a number of sensitivity simulations as compared with those from the control simulation (Exp. CTL).

Section 4.1 describes the experimental designs. Section 4.2 documents the model sensitivity to latent heat release, and surface sensible and latent heat fluxes from the ocean as well as surface characteristics in the absence of diabatic heating. Section 4.3 examines the effects of the surface fluxes in the presence of moist convection.

4.1 Experiment design

In order to investigate the relative importance of various parameters in these secondary developments, five 48-h sensitivity simulations are carried out by turning off a particular parameter while holding all other parameters identical to Exp. CTL. Table 4.1 provides description of all the sensitivity experiments being performed. Note that most of the sensitivity simulations are performed by switching off convective and grid-scale diabatic heating to simplify the diagnosis of the processes leading to the secondary cyclogenesis in the present case. Detailed procedures are described as follows.

Table 4.1 Description of sensitivity simulations, the average e-folding time (T_e) between 13/12-12 and 15/00-48, and the minimum central pressures (P_{min}) of the MFC/NFC.

Code	P_{min} (hPa)	T_e (hour)	Remarks
CTL	972/987	21.8	Control simulation
DRY	986/984	40.8	No convective and grid-scale diabatic heatings are allowed
G90	987/985		DRY run with a uniform grid size of 90 km
NOC	994/987	58.2	DRY run with the ocean replaced by a "continental" surface
NFXD	987/981		DRY run without surface sensible and latent heat fluxes
NFXM	992/983		Moist run without surface sensible and latent heat fluxes

i) No latent heat release (Exp. DRY). As mentioned in the preceding chapter, the rapid spin-up of the MFC after 14/00-24 is accompanied by a substantial amount of precipitation in both the observations and the simulation. Moreover, our PV analysis shows the diabatic generation of a low-level PV anomaly in the cloud region that is vertically "locked" with the upper-level PV anomalies. This indicates that latent heating must have played an important role in the deepening of the system. Thus, it is desirable to isolate the effects of diabatic heating from large-scale baroclinicity on the secondary cyclogenesis. For this purpose, a dry simulation is conducted, in which neither convective nor grid-scale condensation are included (Exp. DRY). The continuity equation for specific humidity is still integrated in order to include the virtual temperature effect. Supersaturation is removed, but the feedback of the resulting latent heat to the thermodynamic equation is neglected. Without the condensational heating, the model atmospheric circulations are only determined by advective processes. Therefore, a comparison between Exps. DRY and CTL would show how these secondary cyclogenesis events depend on latent heating versus large-scale adiabatic processes.

ii) No surface fluxes of sensible and latent heat with (Exp. NFXM) *or without diabatic heating* (Exp. NFXD). Surface heat and moisture fluxes can substantially alter a cyclogenetic environment by reducing its static stability, enhancing condensational heating and modifying the low-level baroclinicity. However, previous numerical studies showed various degrees of their influence on cyclogenesis, e.g., from having an important positive impact (Kuo et al. 1991; Lapenta and Seaman 1992) to virtually no effect (Petterssen et al. 1962; Reed and Simmons 1991) and a negative impact (Kuo and Low-Nam 1990). Since our frontal cyclone family develops in the vicinity of the Gulf Stream, large surface fluxes from the warm ocean may be expected to have a substantial impact on the storm deepening. In particular, Orlanski (1986) and Nakamura (1988) have argued the importance of surface fluxes in the (dry) development of such secondary cyclones. Thus, two sensitivity experiments are performed: one with the surface fluxes switched off from Exp. DRY so that their influence on the dry cyclogenesis can be evaluated (Exp. NFXD), and the other with the surface fluxes withheld from Exp. CTL since surface fluxes may be often more significant in the presence of diabatic heating (Exp. NFXM).

iii) No oceanic surface characteristics (Exp. NOC). Surface characteristics can affect the cyclogenesis through the availability of surface moisture for evaporation, which varies from 0 for a dry surface to 1 for a moist surface, and, most importantly, through the surface roughness that determines the frictional dissipation of cyclonic circulations or cyclonic spin-down (Holton 1993). In particular. the surface frictional effects have been shown by Mullen and Baumhefner (1988), Huo et al. (1996b) and others to be extremely significant for explosively deepening oceanic cyclones. Since all secondary cyclones presented in the preceding chapter deepens over the ocean surface, it is necessary to examine whether or not these developments are solely of oceanic nature, and if not, what is its influence on the final depth of the storm. This could be done by performing a sensitivity experiment, in which the surface roughness length over the ocean is treated as that of "land", with a value typical for the continental interior (Exp. NOC). It should be noted, however, that such an experiment does not isolate completely the frictional effect since the surface winds, modified by the changes in the roughness, will in turn affect the heat and moisture transfers at the ocean surface.

4.2 Adiabatic simulations

a) Influence of diabatic heating versus large-scale processes

When diabatic heating is turned off (Exp. DRY), the structure and intensity of the MFC during the first 18-h integration are nearly the same as that in Exp. CTL (Fig. 3.1), since little precipitation occurs prior to the genesis stage. Then, the MFC deepens at a rate of 20 hPa/30 h, as compared to the control-simulated 34 hPa/30 h rate. At the end of the 48-h simulation, the dry MFC is about 14 hPa weaker than the moist one, which represents approximately 59% of the total deepening by dry dynamics. In terms of the average e-folding time, however, the dry MFC one is about twice as large as that for the moist MFC (see Table 4.1). While diabatic heating plays an important role in the rapid deepening of the MFC, its impact on the track of the system is small. Fig. 2.1 shows that the dry MFC follows closely the observed and the control-simulated tracks, except that it propagates somewhat slower. The difference in position between the two runs is about 400 km at the end of the 48-h integration. It follows that the large-scale dynamics tend to determine the track and development of the secondary cyclone, whereas moist processes help accelerate the propagation and deepening of the system. The results are in agreement with previous studies of explosively deepening oceanic storms that occurred at much larger scales (> 3000 km), e.g., Anthes et al. (1983), Chen et al. (1983), Kuo and Reed (1988), and Huo et al. (1996b). However, they are in significant contrast with the coastal cyclogenesis studies by Lapenta and Seaman (1992) and Doyle and Warner (1992), who showed that the coastal cyclogenesis fails to occur in the absence of latent heating.

The above conclusion could be further seen from the 48-h evolution of surface maps showing the moist and dry frontal cyclones (cf. Figs. 4.1 and 3.2-3.6). The horizontal extent and overall circulation characteristics, including the associated warm/cold frontal structures and the pressure ridge to the north, are similar between the two runs, except for the more tightened pressure gradients in the vicinity of the moist cyclone. Note again that both the MFC and NFC tend to move to the left of the upper-level flow towards the colder air. For example, the surface temperature near the MFC center changes from 17 ^{0}C at 14/00-24 to 15 ^{0}C at 14/12-36 and 11 ^{0}C at 15/00-48 (see Figs. 4.1a-d). It should be mentioned that when a grid size of 90 km is used to simulate the case without diabatic heating (Exp. G90), the model could still duplicate the basic structures of the cyclone family, except that the MFC central pressure is 1 hPa weaker than that in Exp. DRY. This indicates that any grid size between 30 and 90 km is suitable for the simulation of the energy growth at the frontal cyclones scale. A fine grid size of 30 km is used in the moist runs (i.e., Exps. CTL and NFXM) because it allows the use of state of the art Kain-Fritsch cumulus parameterization and grid-scale physics schemes.

On the other hand, the slower movement and the weakening of the dry MFC allow the NFC to increase its intensity, namely, by 3 hPa at the end of the 48-h integration (cf. Figs. 4.1d and 3.6b). This appears to result from the less significant suppression of the NFC cyclonic circulation by the MFC, through the vortex-vortex interaction (Hikum et al. 1996), when the two cyclones are in close proximity. It is of interest that the more intense NFC gives rise to more pronounced southward transport of colder air, increasing substantially the surface thermal gradient across the MFC, e.g., 20 ^{0}C/20^{0} LON in Exp. CTL versus 34 ^{0}C/20^{0} LON in Exp. DRY (cf. Figs. 4.1d and 3.6b). This appears to explain the more rapid deepening of the MFC in the final 12-h integration. It is also of interest that although the NFC appears to be 2 hPa deeper in central pressure than the MFC, its circulation intensity, horizontal extent and vertical depth are not as robust as the MFC; similarly in other sensitivity simulations. This could be attributed to the fact that the NFC central pressure drop is largely caused by its movement from a high- to lower-pressure region towards the center of the weakening parent cyclone, as mentioned in Chapter 3. Moreover, the impact of diabatic heating on the NFC

a)

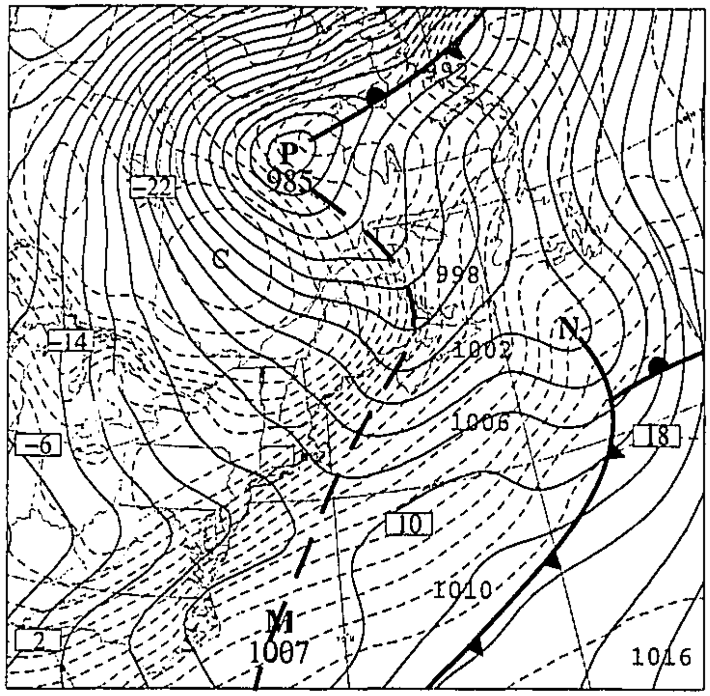

b)

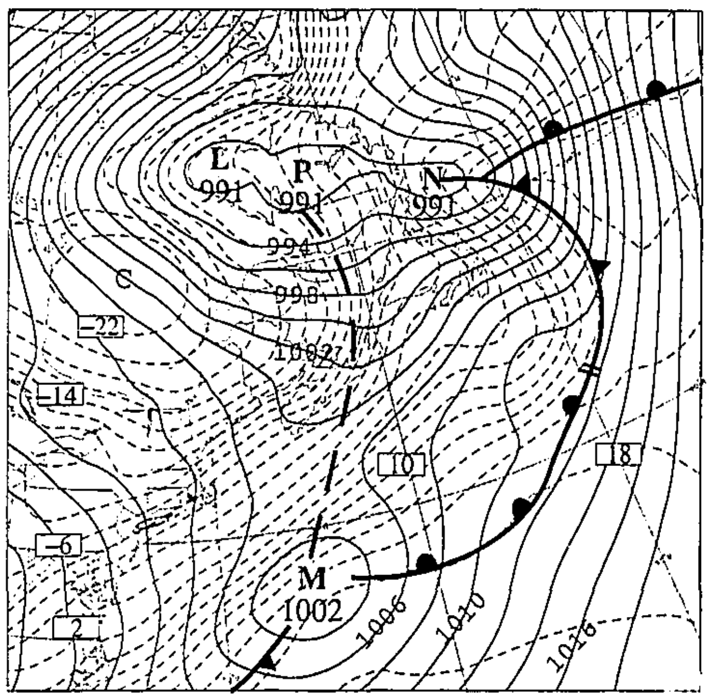

Fig. 4.1 Sea-level pressure (solid) at intervals of 2 hPa and surface temperature (dashed) at intervals of 2 °C from: a) 12-h integration (13/12-12); b) 24-h integration (00/14-24); c) 36-h integration (12/14-36); and d) 48-h integration (15/00-48) of Exp. DRY. Subjectively analyzed troughs and fronts are also shown. Locations of the parent, major and northern frontal cyclones are marked by letters "P", "M" and "N", respectively. Line AB in (d) shows the location of cross section used in Fig. 4.2a.

c)

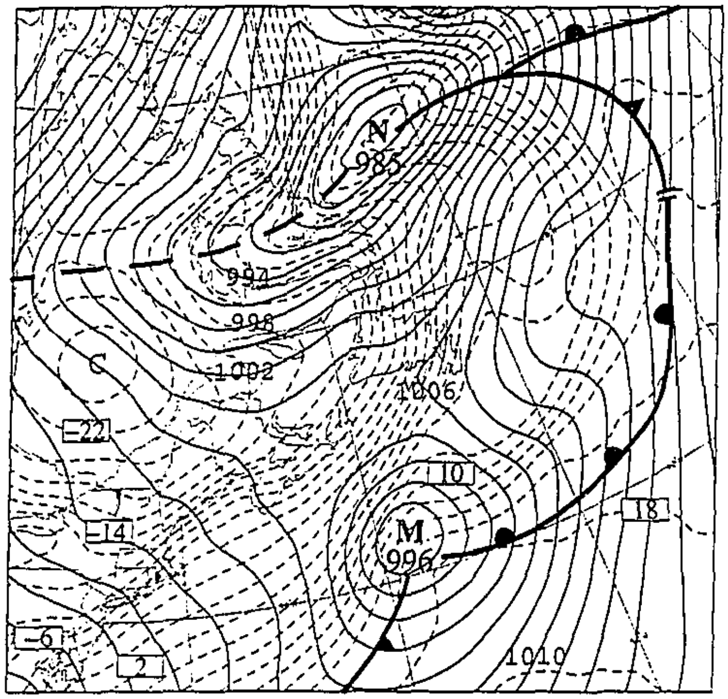

d)

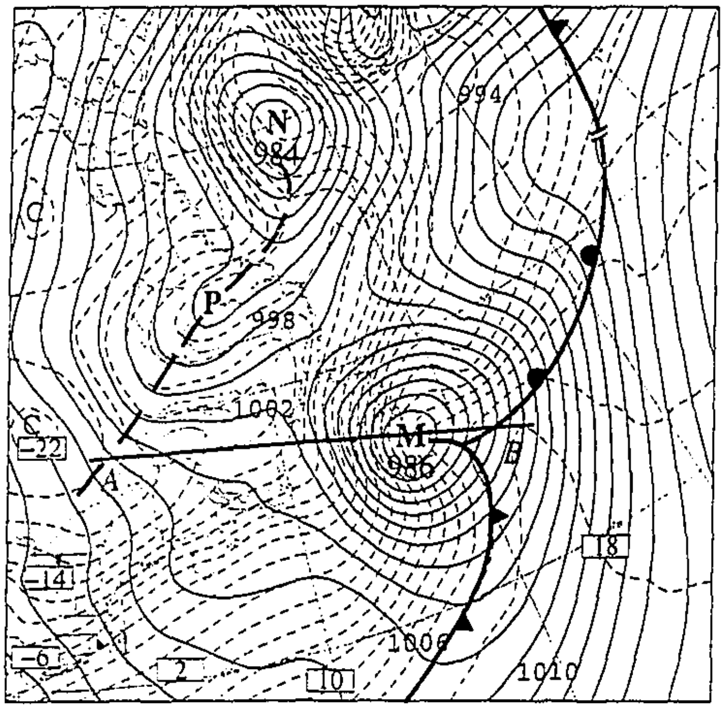

Fig. 4.1 (continued)

genesis is very small, since most of the latent energy supply from the south tends to be intercepted by the MFC. In contrast, the SFC fails to materialize in the absence of latent heating; only a weak mesotrough develops (see Fig. 4.1d). This implies that the SFC develops mainly as a result of latent heat release rather than the large-scale dry dynamics. This may explain why it is weak in all moist integrations (i.e., Exps. CTL and NFXM), as compared to the MFC and NFC.

To further understand the significance of the diabatic heating and the large-scale baroclinicity in the MFC genesis, Fig. 4.2a show the vertical cross section of height and temperature deviations at the end of the 48-h integration from the dry run. A comparison with Fig. 3.13 reveals: i) the development of a shallower height trough (up to 850 hPa) associated with the dry MFC; ii) the less pronounced influence of the dry MFC on the midtropospheric thermal field, as evidenced by the eastward tilt of isotherms above 800 hPa; and iii) the presence of strong thermal gradients below 800 hPa in the absence of diabatic heating. It is also evident that the large-scale trough, with its vertical structure nearly identical to that in Exp. CTL, does not seem to provide significant quasi-geostrophic forcing on the spin-up of the MFC.

The net (direct and indirect) effects of diabatic heating on the MFC genesis can be evaluated from Fig. 4.2b, which shows the height and temperature differences between the two simulations (i.e., CTL minus DRY). In the presence of diabatic heating, the MFC experiences net warming above 800 hPa with a maximum value of $> 6\ ^0$C occurring near 550 hPa and net cooling below with a minimum value of $< -6\ ^0$C. This net warming/cooling profile is hydrostatically consistent with the height deficit (rise) in the lower (upper) levels. Of importance is that although the strong net warming occurs in the upper troposphere, the most significant cyclonic response takes place near the surface. According to Hirschberg and Fritsch (1991), a given temperature perturbation in a layer of the upper troposphere would induce a larger pressure perturbation near the surface than in a layer of the lower troposphere. The lower- (upper-) level net height deficit (rise) implies increased mass and moisture

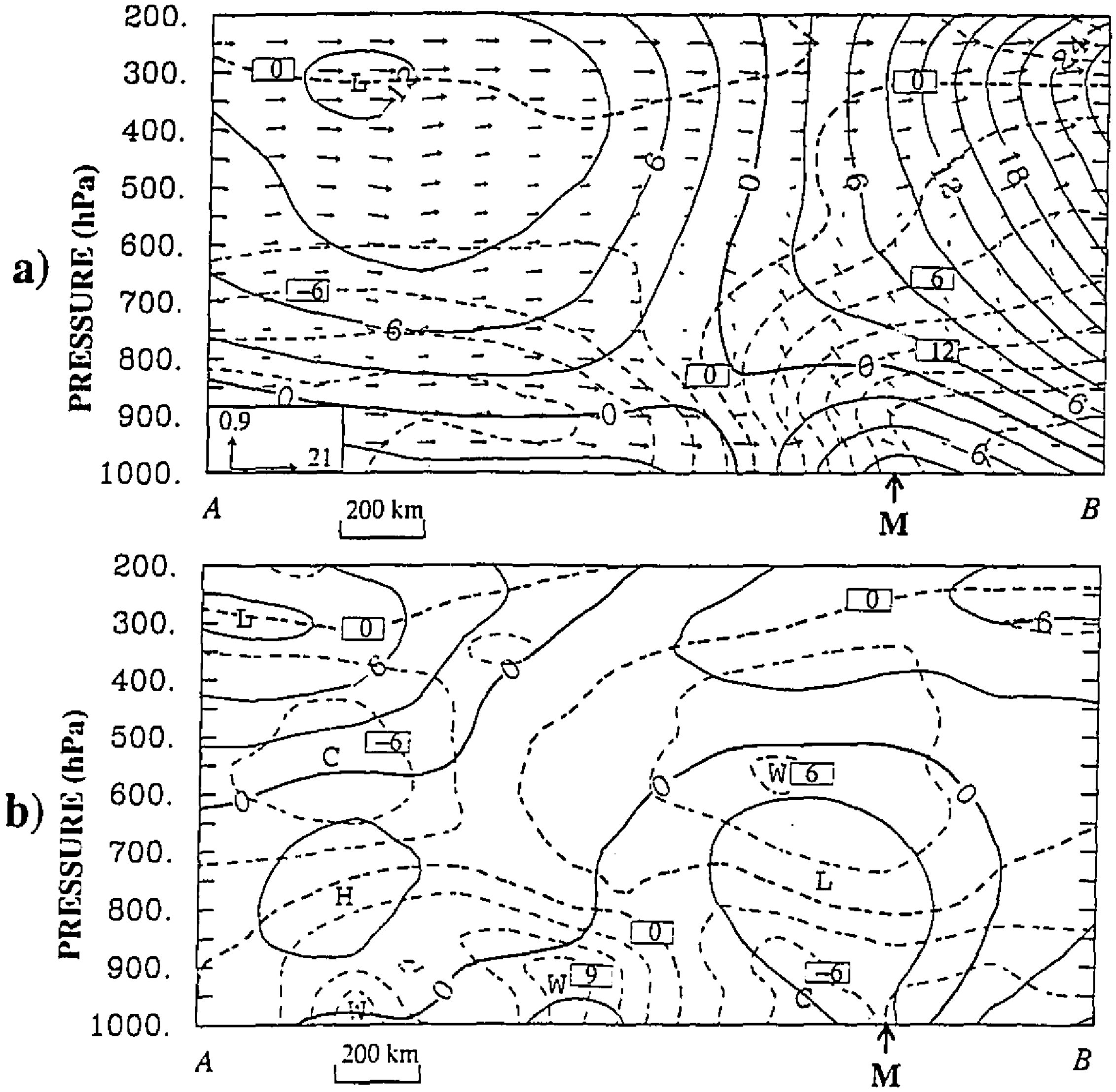

Fig. 4.2 Vertical cross section of (a) height deviations (solid) at intervals of 3 dam and temperature deviations (dashed) at intervals of 3 °C, superposed with along-plane flow vectors, which is taken along line AB in Fig. 4.1d from the 48-h DRY simulation; and (b) the height difference field (solid), at intervals of 3 dam and temperature difference field (dashed), at intervals of 3 °C between Exps. CTL and DRY, i.e., the fields shown in Fig. 3.13 minus those in Fig. 4.2a. Inset shows the scale of vertical (Pa s^{-1}) and horizontal motions (m s^{-1}). Location of the surface major frontal cyclone is indicated on the abscissa.

convergence (divergence) in the lower (upper) troposphere, which is favorable for cyclonic development. Because of the interaction between the MFC and NFC, the lowest 200 hPa in the cold sector, i.e., to the west of the MFC, is more than 9 ^{0}C warmer than that in Exp. DRY. This implies a reduced thermal gradient in the boundary layer, as previously mentioned, that is unfavorable for the production of available potential energy and thus the deepening of the MFC. Otherwise, the moist processes without the NFC may increase the cooling in the cold sector, as does in the layers above 800 hPa (Fig. 4.2b), since more cold air mass could be transported into the region by the enhanced cyclonic circulations (e.g., Huo et al. 1995).

The relative importance of dry dynamics in the development of the frontal cyclone family could again be understood from the upper- and low-level PV interactions. It is apparent from Fig. 4.3 that significant PV is being advected into the MFC from the PV ring to the rear, as appeared in the control run. The upper-level PV distribution exhibits little difference between Exps. CTL and DRY, except for the location of the MFC influence. This explains why the frontal cyclones in all the sensitivity simulations follow closely a track which is "arc-shaped" as the upper-level PV ring. Most of the differences among different simulations appear to occur in the lower levels, mainly in the magnitude, depth and horizontal extent of the low-level PV. Note first the formation of two low-level PV anomalies associated with the MFC and NFC, even in the absence of diabatic heating (Fig. 4.3a). A vertical cross section taken through the MFC center shows that intense PV, peaked at about 950 hPa, is concentrated in the frontal zone with magnitude half that in Exp. CTL. According to Davis et al. (1993), this strong low-level PV is generated by non-conservative processes, such as numerical diffusion, the surface friction and heat fluxes. While the low-level PV concentration is very weak and shallow compared to that in Exp. CTL, it is, to some degree, still coupled with its upper-level counterpart. By comparison, the advection of the upper-level PV remains favorable near the NFC until 36 h into the simulation, whereas little PV advection takes place near the SFC owing to its location at the lateral periphery of the upper-level PV ring.

a)

b)

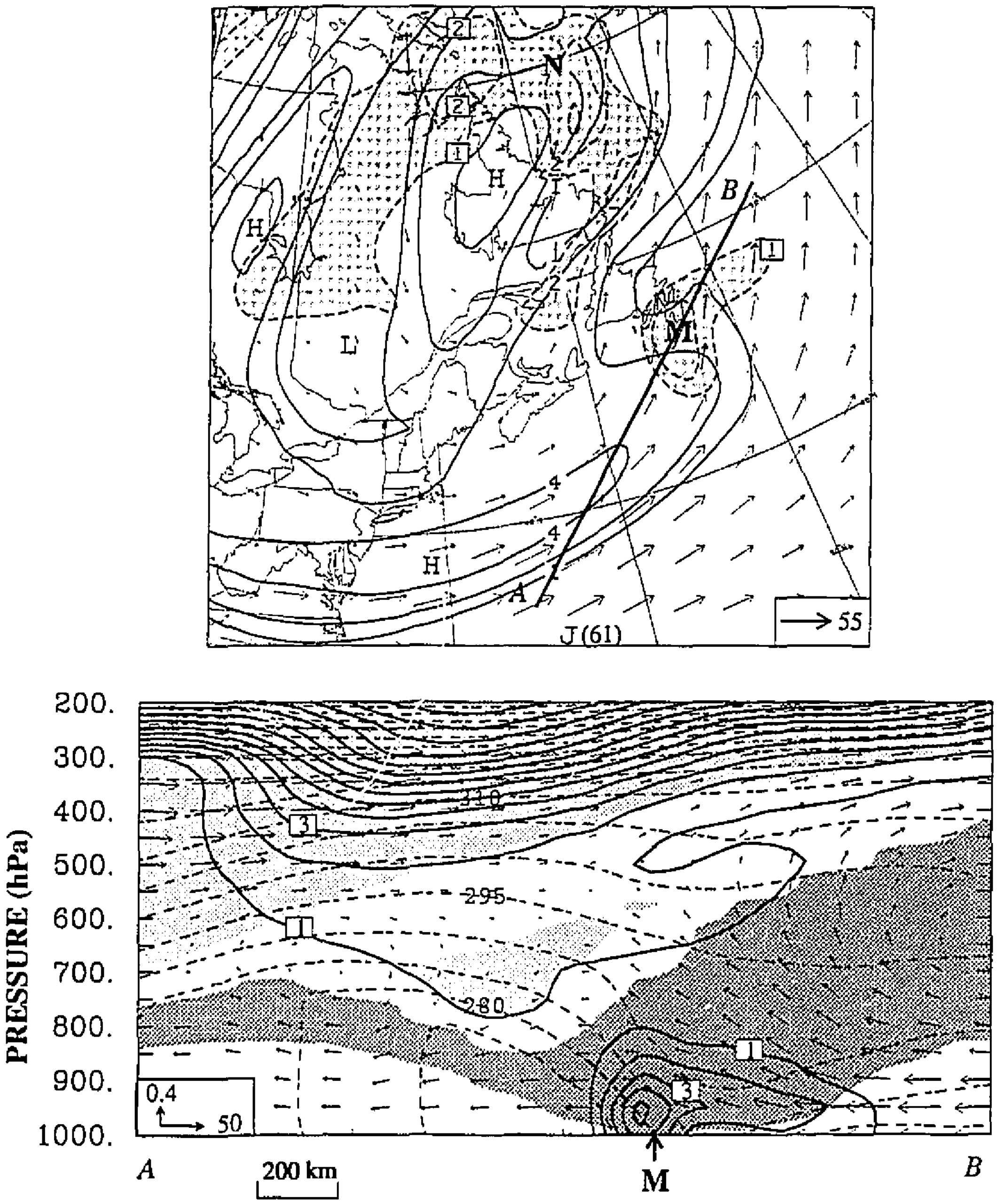

Fig. 4.3 As in Fig. 3.16, but for Exp. DRY at 15/00-48.

The results further reveal that the upper-level PV ring and its advection are instrumental in determining the track (see Fig. 2.1) and intensity (see Fig. 3.1) of the frontal cyclone family.

b) Influence of ocean surface characteristics

Since both the MFC and NFC develop in the absence of diabatic heating, it is natural to examine whether or not the dry frontal cyclogenesis is mainly caused by the less rough ocean surface. Surprisingly, the model is still able to replicate the MFC and NFC when the ocean surface in Exp. DRY is replaced by a "continental" surface (Exp. NOC). The basic circulation structures resemble well their pure dry counterparts (cf. Figs. 4.1 and 4.4). This further enforces the conclusion that the large-scale dry dynamics plays an essential role in the present secondary cyclogenesis events. However, treating the ocean as land results in the development of the weakest and slowest moving MFC among all the sensitivity tests performed; similarly for the NFC (see Table 4.1). For example, the MFC in Exp. NOC at the end of the 48-h integration is 8 (22) hPa weaker, and 500 (1100) km slower than that in Exp. DRY (CTL) (see Figs. 2.1, 3.1, 4.1 and 4.4). The average e-folding time is 58 h (see Table 4.1), which is much longer than that in Exps. DRY (41 h) and CTL (22 h). The result is in agreement with previous sensitivity studies in which weaker cyclones always move relatively slower (Kuo et al. 1991; Huo et al. 1996). As will be discussed in section 4.3, the effects of ocean surface sensible and latent heat fluxes in the absence of diabatic heating are small. Hence, the 8-hPa central pressure difference could be attributed to the increased surface drag over the ocean. Qualitatively, this is consistent with the boundary-layer theory that increasing the surface drag would result in a more rapid loss of horizontal momentum and spin-down of cyclonic vorticity (see Holton 1993). Thus, the result implies that i) the "Ekman" pumping is an important parameter in determining the amplification of frontal cyclones; and ii) the more rapid frontal cyclogenesis phenomena tend to occur more frequently over the oceans.

a)

b)

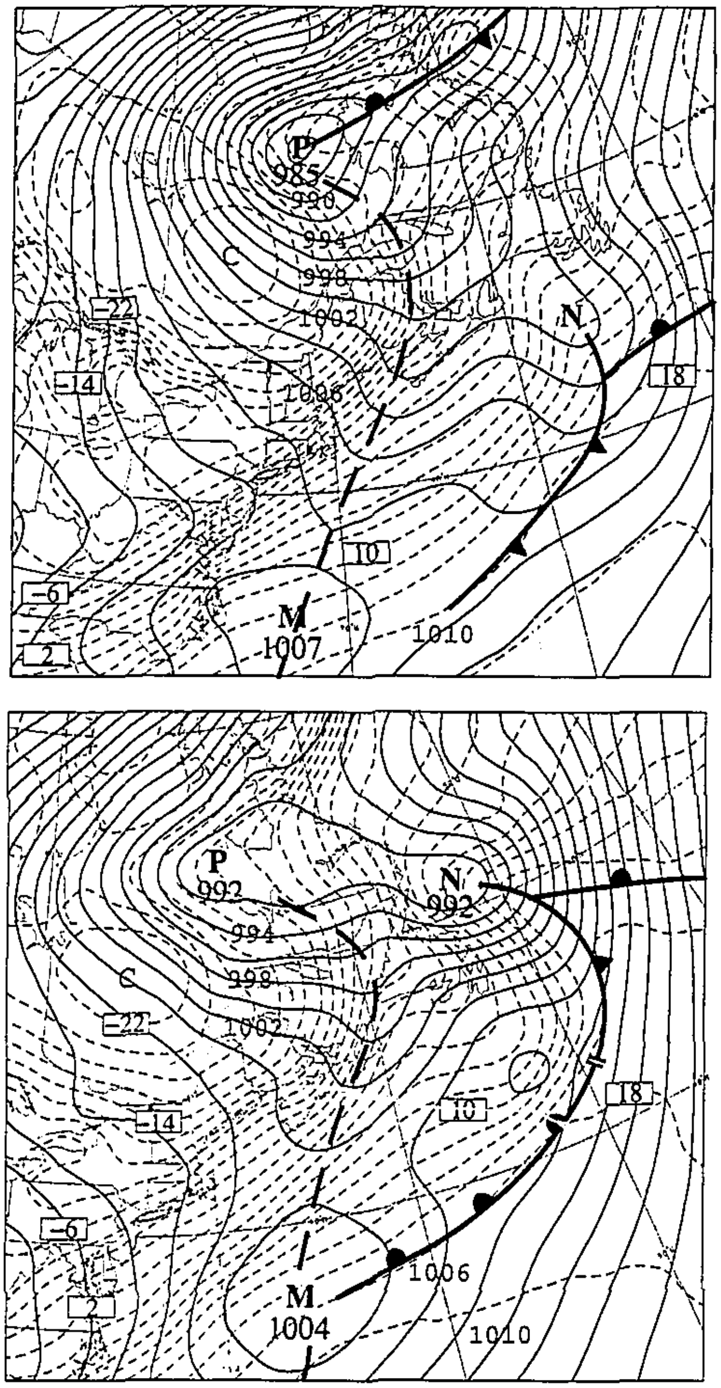

Fig. 4.4 As in Fig. 4.1, but for Exp. NOC.

c)

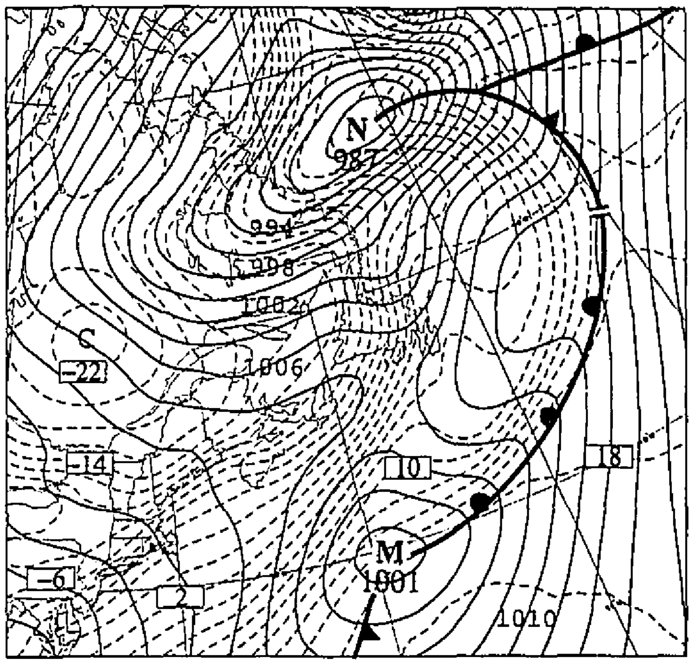

d)

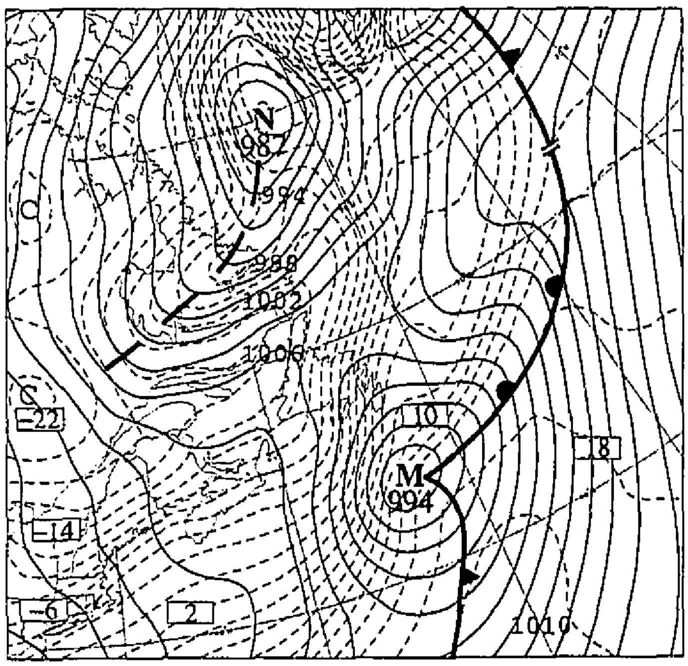

Fig. 4.4 (continued)

c) Relative importance of upper- versus low-level adiabatic processes

It is evident from the sensitivity simulations discussed above that the dry dynamics account for the genesis and a large portion of the final depth of the MFC and NFC. Thus, it is desirable to examine quantitatively different upper-level adiabatic forcings, i.e., vorticity versus thermal advection, to the cyclogenesis. This can be done through diagnostic analysis of the dry simulation using the simplified Zwack-Okossi development equation (Lupo et al. 1992; henceforth Z-O). The Z-O equation provides a complete description of all the forcing contributions at any level to the geostrophic vorticity changes at the surface or any pressure level close to the surface. The vorticity budget is performed at 950 hPa, at which level the frictional effect is small and so it can be neglected. The modified Z-O equation is given by Lupo et al. (1991) as follows:

$$\frac{\partial \xi_{gl}}{\partial t} = Pd \int_{Pt}^{Pl} (-\mathbf{V} \cdot \nabla \xi_a)\, dp - Pd \int_{Pt}^{Pl} \left[\frac{R}{f} \int_{P}^{Pl} \nabla^2 \left(-\mathbf{V} \cdot \nabla T + \frac{Q}{c_p} + S\omega\right) \frac{dp}{p} \right] dp$$

$$+ Pd \int_{Pt}^{Pl} \mathbf{k} \cdot \nabla \times \mathbf{F}\, dp - Pd \int_{Pt}^{Pl} \frac{\partial \xi_{ag}}{\partial t}\, dp \ , \qquad (4.1)$$

where ξ_{gl} is the geostrophic vorticity at level l ; P_l and P_t are the pressures at the bottom and top of the integration column, respectively; $Pd = (P_l - P_t)^{-1}$; ξ_a $(= \xi + f)$ denotes the absolute vorticity ; Q represents the diabatic heating rate; S is the static stability parameter, as defined by $S = -(T/\theta)(\partial\theta/\partial p)$; $\mathbf{F}$ denotes the friction force; and the other variables have their conventional meaning. The vertical velocity, ω, in p-coordinates is calculated using the omega equation as derived by Tsou and Smith (1990),

$$\left[\frac{R}{p} S \nabla^2 + f(\xi + f) \frac{\partial^2}{\partial p^2} \right] \omega = -f \frac{\partial}{\partial p} (-\mathbf{V} \cdot \nabla \xi_a) + \frac{R}{p} \nabla^2 (-\mathbf{V} \cdot \nabla T)$$

$$- \frac{R}{p} \nabla^2 \left(\frac{Q}{c_p}\right) + f \frac{\partial}{\partial p} (\mathbf{k} \cdot \nabla \times \mathbf{F}) \ . \qquad (4.2)$$

Eq. 4.2 implies that the vertical motion results from the contributions of four elements, namely, due to vertical differential vorticity advection (ω_ξ), the Laplacian of thermal advection (ω_T) and diabatic heating (ω_Q), and the vertical differential friction-induced vorticity (ω_F).

In the dry case, the diabatic heating terms in Eqs. (4.1) and (4.2) vanish. We may further simplify the vorticity tendency budget by excluding the last term of Eq. (4.1), since Tsou et al. (1987) found that the ageostrophic effect is small on synoptic temporal and spatial scales. If the frictional effect over the ocean can be neglected, Eqs. (4.1) and (4.2) can be rewritten as

$$\frac{\partial \xi_{gl}}{\partial t} = P_d \int_{P_t}^{P_l} (-\mathbf{V} \cdot \nabla \xi_a) \, dp - P_d \int_{P_t}^{P_l} \left[\frac{R}{f} \int_{P}^{P_l} \nabla^2 (-\mathbf{V} \cdot \nabla T + S\omega) \frac{dp}{p} \right] dp \ , \qquad (4.3)$$

$$\left[\frac{R}{p} S \nabla^2 + f(\xi + f) \frac{\partial^2}{\partial p^2} \right] \omega = f \frac{\partial}{\partial p} (-\mathbf{V} \cdot \nabla \xi_a) + \frac{R}{p} \nabla^2 (-\mathbf{V} \cdot \nabla T) \quad . \qquad (4.4)$$

The combination of Eqs. (4.3) and (4.4) gives the final form of the Z-O vorticity budget used in our analysis of the dry simulation,

$$\frac{\partial \xi_{gl}}{\partial t} = P_d \int_{P_t}^{P_l} \left[-\mathbf{V} \cdot \nabla \xi_a , \ - \frac{R}{f} \int_{P}^{P_l} \nabla^2 (S\omega_\xi) \frac{dp}{p} \right] dp$$

$$- P_d \int_{P_t}^{P_l} \left[\frac{R}{f} \int_{P}^{P_l} \nabla^2 (-\mathbf{V} \cdot \nabla T + S\omega_T) \frac{dp}{p} \right] dp \ , \qquad (4.5)$$

where $P_t = 100$ hPa is used to include some potential effects of the lower stratosphere. Terms on the right hand side of Eq. (4.5) represent the column-integrated contributions due to the vertical differential vorticity advection and the Laplacian of horizontal temperature advection to the net vorticity tendency at 950 hPa. Both terms include a purely advective part and the vorticity changes due to the adiabatic cooling (warming) in their induced ascent (descent). It is found that the induced cooling or warming effects are always negatively correlated with but weaker than their advective contributions (not shown). The above Z-O vorticity budget as well as the ω-equation computation are performed using the software package developed by Desjardin et al. (1993). The ω-equation is solved using successive over-relaxation assuming zero vertical and lateral boundary conditions.

Figure 4.5 shows one example of the column-integrated vorticity budget from the 24-h dry simulation, at which time the rapid deepening of the MFC just began. Two well-organized positive/negative tendency couplets are seen corresponding to the MFC and NFC, with their centers located near the zero tendency isopleths. The positive tendency centers represent roughly the locations where the cyclones are about to propagate, and thus Eq. (4.5) predicts correctly the movement and the trend of cyclonic development. Because the NFC has entered its most rapid deepening stage by this hour, its vorticity tendency couplet is greater in both amplitude and horizontal extent than the one associated with the MFC.

The net vorticity tendency couplets are well coordinated with the column-integrated contributions due to the vorticity advection and the Laplacian of thermal advection, with very slight phase shifts (cf. Figs. 4.5a-c). The vorticity contributions are closely related to the propagation of low-level cyclonic vorticity (e.g., see Fig. 3.14) and the advection of upper-level PV (see Fig. 4.3), whereas the thermal contributions are positive (negative) ahead (behind) in the southeasterly (northwesterly) sloping flow along the warm- (cold-) frontal zones (see Fig. 4.5c). Despite the fact that the adiabatic cooling (warming) always operates in the opposite sense to the vorticity and thermal advections [see Eq. (4.5)], both forcings exhibit well-defined positive contributions to the cyclonic developments. Of importance is that the thermal contributions to the column-integrated net tendencies are greater than those due to the vorticity advection for both the MFC and NFC. This suggests that the lower-level thermal

a)

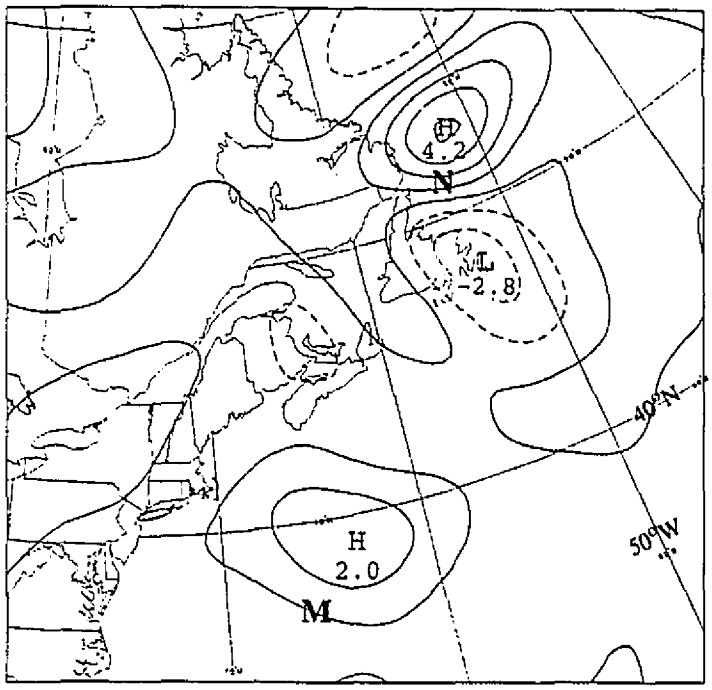

b)

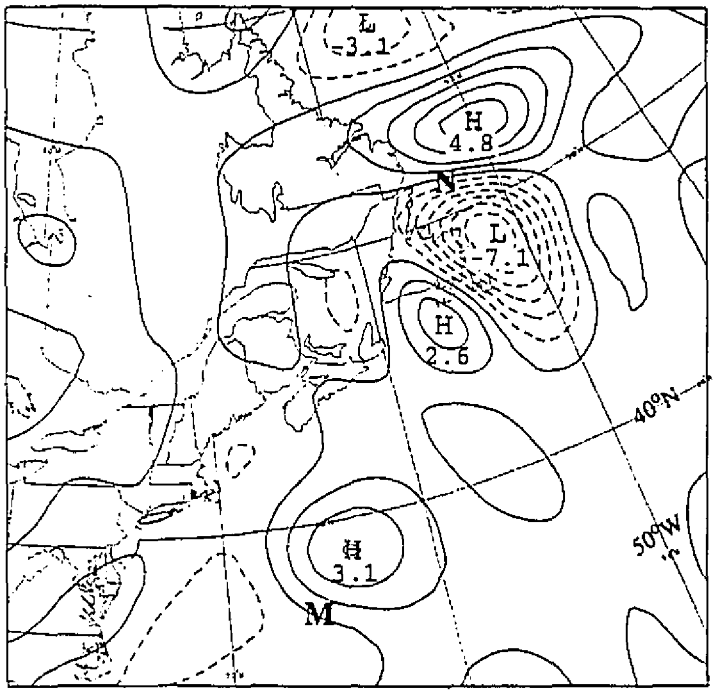

Fig. 4.5 Horizontal maps of the column-integrated vorticity budget at 950-hP at intervals of 10^{-9} s^{-2} from 24-h integration of Exp. DRY (14/00-24): a) contribution of differential vorticity advection; b) contribution of the Laplacian of temperature advection; and c) net tendency. Centers of the surface major and northern frontal cyclones are marked by letters "M" and "N", respectively. Boxes in (c) indicate the area over which the vorticity tendencies are averaged (see Table 4.1).

c)

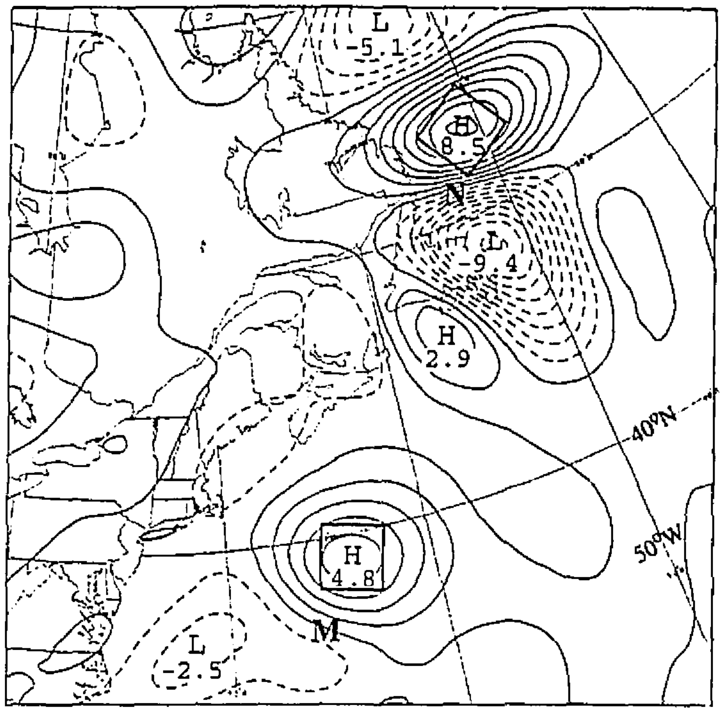

Fig. 4.5 (continued)

advection plays an important role in the genesis of the MFC and NFC, since more significant thermal advection occurs in the lowest 300 hPa (see Fig. 3.10) where both the flows (> 20 m s^{-1}) and thermal gradients (2 - 4 ^{0}C/100 km) are intense.

To gain further insight into the relative significance of the (upper-level) vorticity advection and the Laplacian of (low-level) thermal advection in the spin-up of the MFC and NFC, Tables 4.2 and 4.3 show 12-hourly the area-averaged contributions to the net vorticity tendency at 950 hPa during the life cycle of the two systems. It can be seen from Table 4.2 that the magnitudes of both advective effects increase with time, which is consistent with the continued deepening of the MFC. Of interest is that despite the concurrent increases their relative importance remains nearly steady during the life cycle of the MFC, namely, the thermal contribution accounts for over 60% of the total (dry) deepening. This implies that the intense low-level baroclinicity is crucial not only to the genesis, but also to the explosive deepening of the MFC.

Table 4.2 The magnitudes (10^{-9} s^{-2}) and relative contribution (%) of the column-integrated vorticity advection and the Laplacian of the thermal advection to the net geostrophic vorticity tendency at 950 hPa that are averaged over an area of 270 km x 270 km ahead of the MFC center.

	13/12-12	14/00-24	14/12-36	15/00-48
Vorticity (%)	0.9 (36)	2.0 (37)	3.6 (38)	5.2 (41)
Thermal (%)	1.5 (64)	3.1 (63)	5.8 (62)	7.6 (59)

Table 4.3 As in Table 4.2 but for the NFC.

	13/12-12	14/00-24	14/12-36
Vorticity (%)	2.5 (49)	4.2 (47)	4.7 (52)
Thermal (%)	2.6 (51)	4.8 (53)	4.3 (48)

Likewise, the magnitudes of thermal and vorticity contributions to the net vorticity tendency of the NFC also increase as it enters its mature stage; but their relative importance remains nearly the same, i.e., about 50% (see Table 4.3). Both contributions decrease after 36 h into the integration mainly owing to the "blocking" effect of the Greenland topography, which is consistent with the slow evolution of the NFC. The above findings appear to differ from the previous studies of oceanic storms in which the vorticity advection contributes the most to cyclogenesis during the explosive deepening phase (Lupo et al. 1992; Reed et al. 1994; Huo et al. 1996a,b).

4.3 Effects of oceanic sensible and latent heat fluxes

When both the diabatic heating and surface fluxes are turned off (Exp. NFXD), the track and central pressure trace of the MFC follow closely those in Exp. DRY (cf. Figs. 4.6 and 4.1); its central SLP is only 1 hPa weaker than its pure dry counterpart at the end of the 48-h integration. Note, though, that the central SLP difference is relatively larger at the MFC incipient stage (i.e., 3 hPa, see Table 4.4). This 3-hPa SLP difference is mainly caused by the surface sensible heat flux over the warm ocean since the effect of surface moisture flux is only significant when grid-box saturation occurs. Specifically, the upward surface heat flux ahead of the cold front before 14/00-24 tends to increase the thermal gradient, at least in the boundary layer (see Fig. 3.3a), thereby assisting the spin-up of the MFC in the context of dry dynamics — a positive effect on the frontal cyclogenesis. As the system moves far offshore, however, strong upward heat flux takes place primarily in the cold sector, as shown in Fig. 4.7, weakening the thermal gradient across the cold front (cf. Figs. 4.1 and 4.6). This explains why the central SLP difference between the two runs decreases towards the end of the 48-h simulation — a negative impact on the frontal cyclogenesis. Nevertheless, the results imply that in the absence of diabatic heating, the surface heat fluxes have very weak impact, through modifying the low-level baroclinicity, on the evolution and final intensity of the frontal cyclones. Thus, it would be more meaningful to investigate the effects of surface

a)

b)

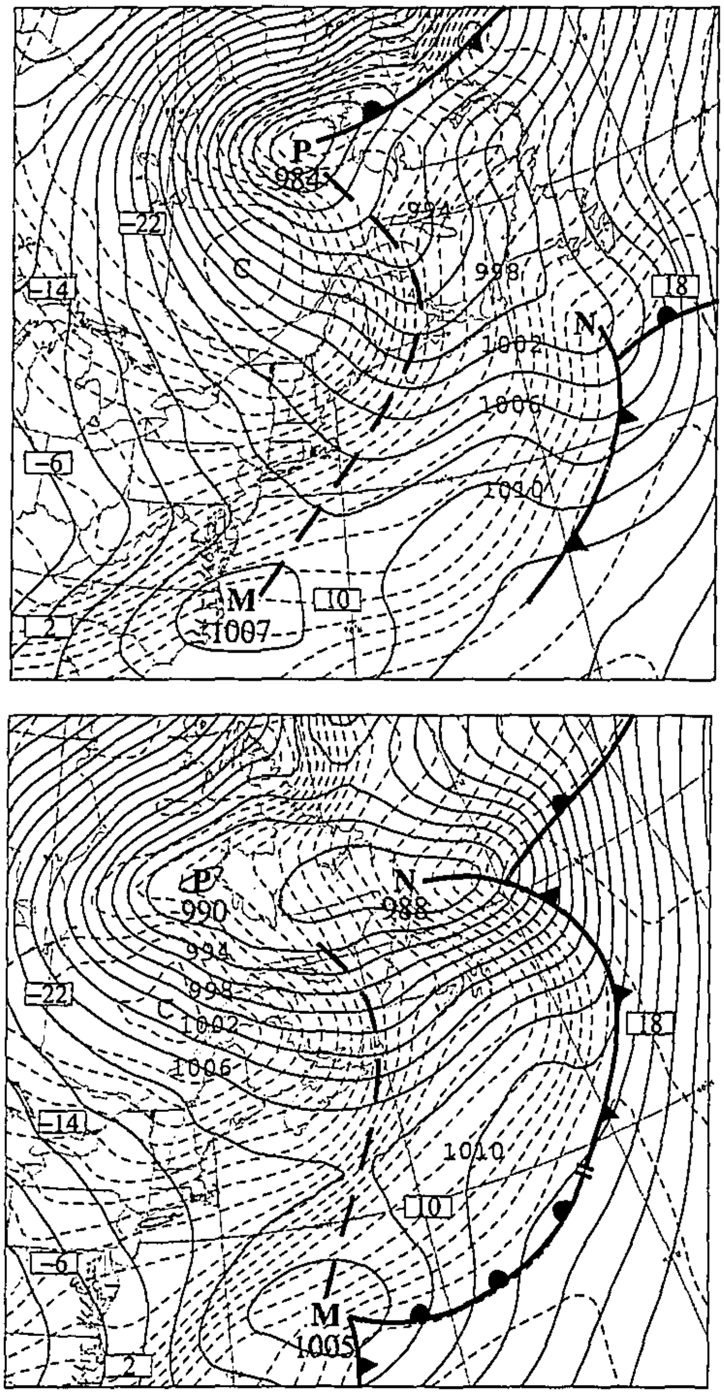

Fig. 4.6 As in Fig. 4.1, but for Exp. NFXD.

c)

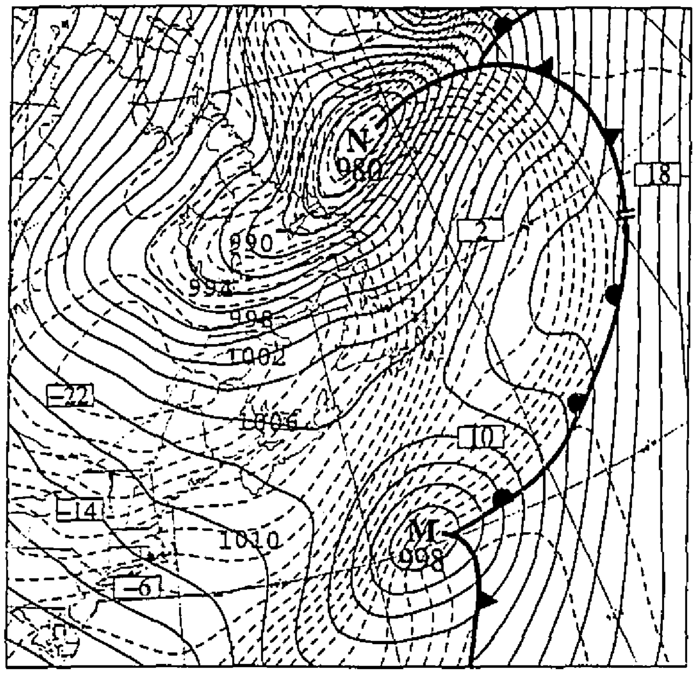

d)

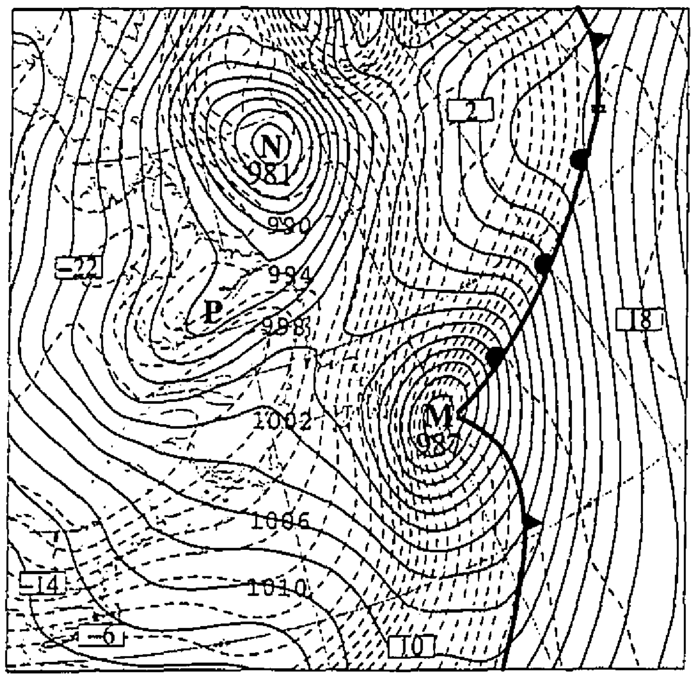

Fig. 4.6 (continued)

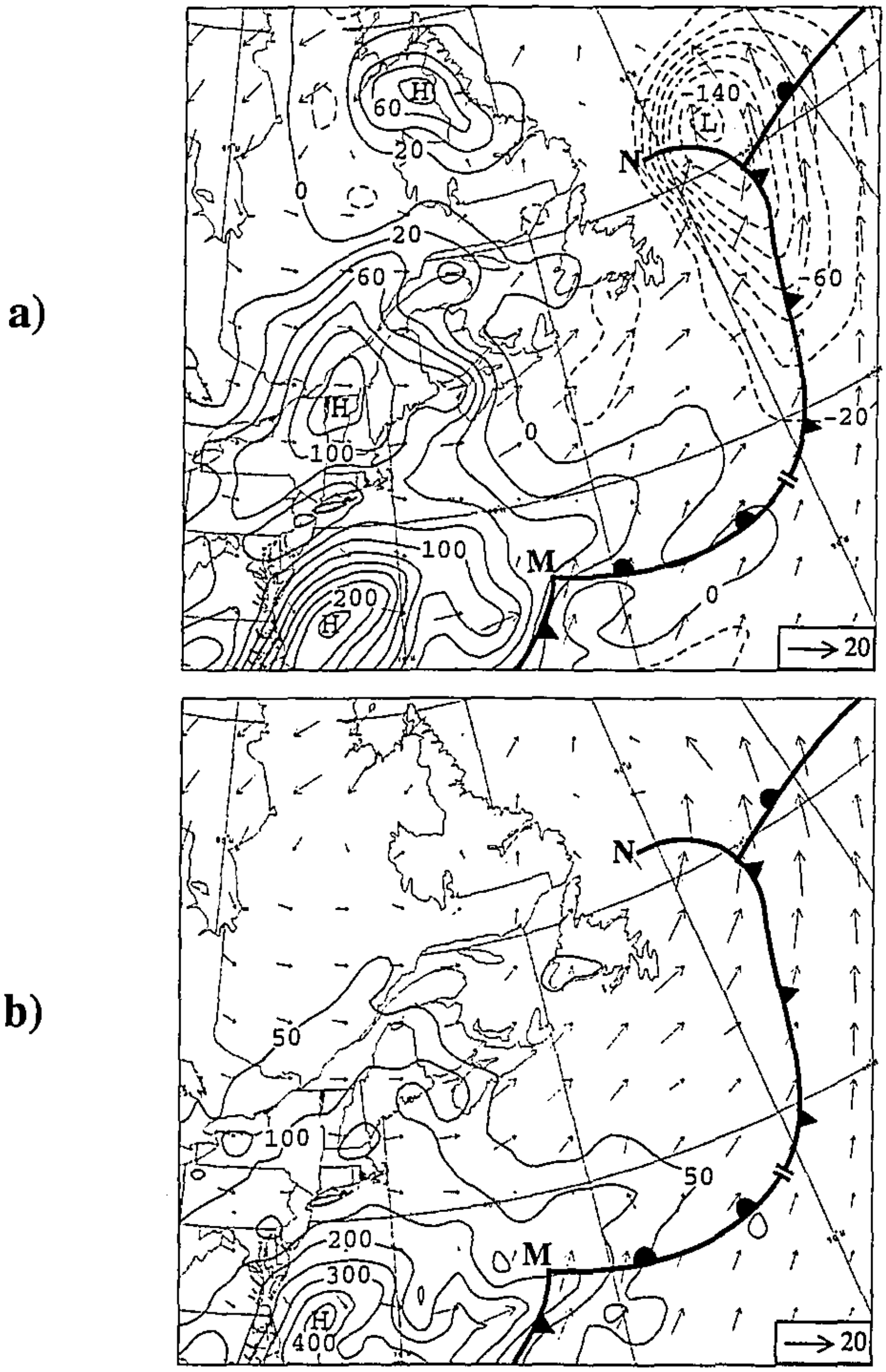

Fig. 4.7 Distribution of a) surface sensible heat flux at intervals of 20 W m^{-2}; and b) surface latent heat flux at intervals of 50 W m^{-2}, superposed with 900-hPa wind vectors from 24-h control simulation (14/00-24).

fluxes on the cyclogenesis in the presence of diabatic heating.

Table 4.4 Central SLP differences (hPa) between (a) Exps. NFXD and DRY (ΔP_{DRY}); and (b) Exps. NFXM and CTL (ΔP_{MST}).

	14/00-24	14/12-36	15/00-48
ΔP_{DRY}	3	2	1
ΔP_{MST}	6	10	14

When the surface fluxes are withheld but diabatic heating is allowed (Exp. NFXM), the model captures reasonably well the timing and location of the family of frontal cyclogenesis events as well as their life cycles (see Figs. 4.8a-d). However, the central SLP traces exhibit a continuing underdeepening of the MFC compared to that in Exp. CTL (see Fig. 3.1) — an indication of the positive influence of surface fluxes on the cyclogenesis. The MFC at the end of the 48-h simulation is 14 hPa weaker than that in Exp. CTL, which represents about 59% of the total deepening due to the surface fluxes. This impact is as pronounced as turning off the diabatic heating! Furthermore, Exp. NFXM reproduces the development of the SFC after 36 h into the integration, although it is relatively weak. It follows that the surface fluxes play a more significant role in oceanic cyclogenesis in the presence of diabatic heating, through reducing the static stability and increasing the moisture content in the maritime boundary layer. Note, however, that the deepening rate of the MFC becomes closer to that in Exp. CTL after 36-h integration (see Fig. 3.1), indicating the much less significant impact of the surface fluxes on the MFC genesis during its mature stage. This appears to be attributable to the rapid decreases of surface fluxes in the vicinity of the MFC as it moves northeastward into a colder water surface (see Fig. 4.7) where the continuing northward transport of tropical high-θ_e air tends to reverse the air-sea thermal gradient in the warm sector. Otherwise, the central SLP difference between the two runs could be much more pronounced.

a)

b)

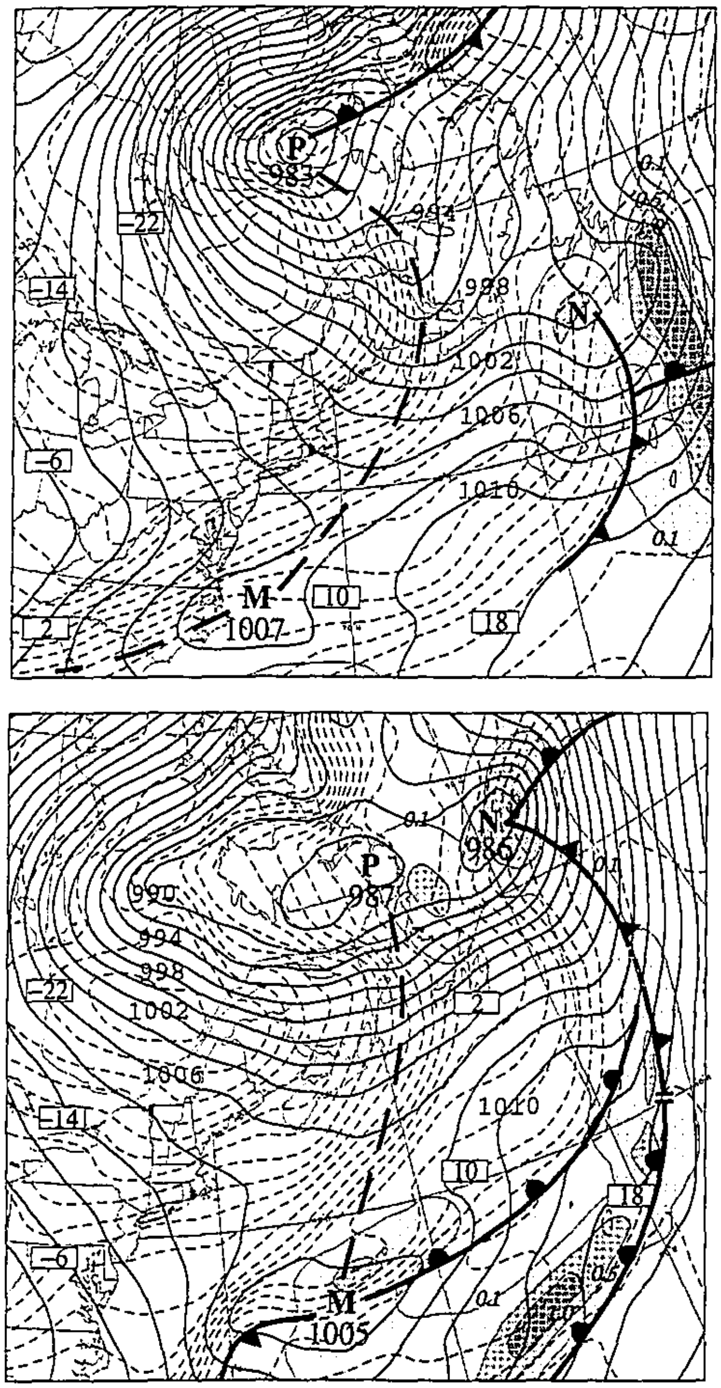

Fig. 4.8 As in Fig. 4.1, but for Exp. NFXM. Superposed is 6-hourly accumulated precipitation with contours of 0.1, 0.5, 1 cm.

c)

d)

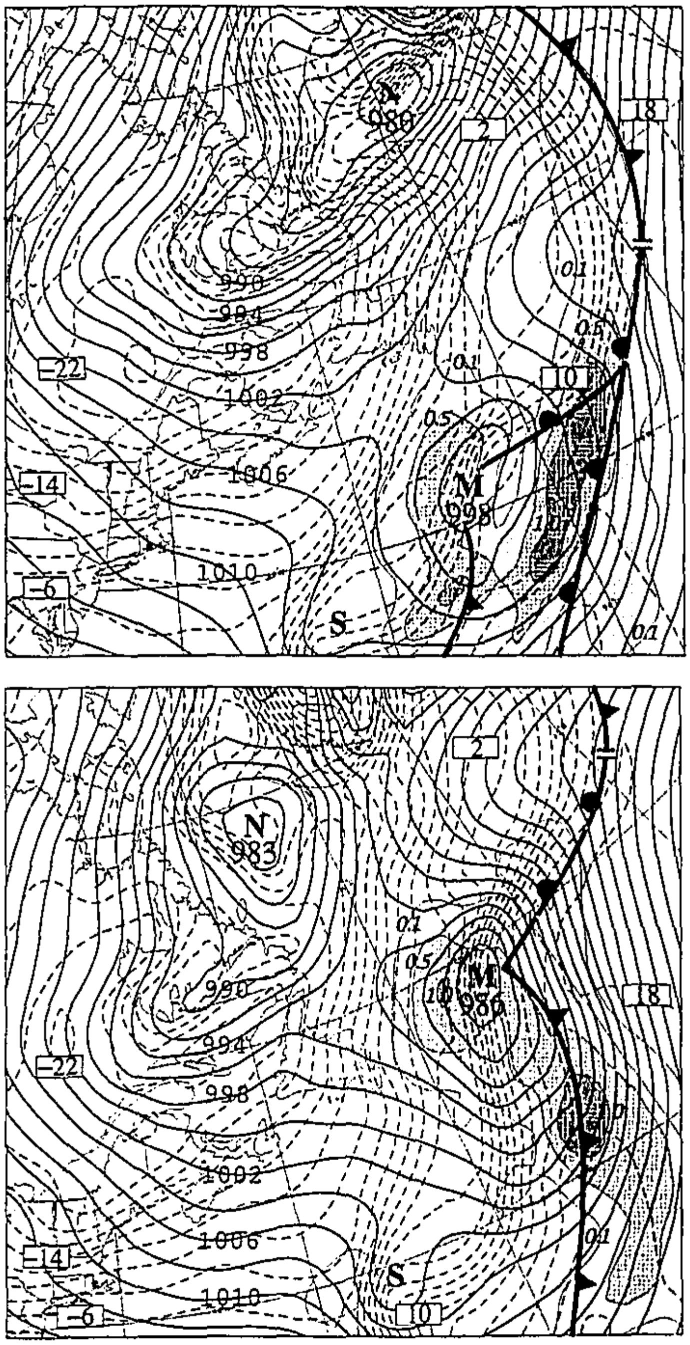

Fig. 4.8 (continued)

Since the surface fluxes affect the cyclogenesis more markedly in the presence of diabatic heating, it is desirable to compare the 48-h accumulated precipitation between Exps. CTL and NFXM in relation to the MFC development. It is seen from Figs. 4.9c,d that in the absence of surface fluxes, much less convective precipitation is generated during the MFC early development stages when it traverses the warm Gulf Stream. Only after 14/12-36, does more convective precipitation occur along the primary cold front as the tropical high-θ_e air overruns the frontal zone (cf. Figs. 4.8 and 4.9). Likewise, Exp. NFXM fails to produce an elongated zone of intense stratiform precipitation (> 3 cm) along the MFC track until 14/12-36, implying the delay of grid-box saturation near the MFC center. Furthermore, the storm development to the south of the MFC tends to intercept CAPE and moisture content that would be otherwise released along the warm frontal zone of the MFC system, which leads to poor efficiency of the diabatic heating (Hack and Schubert 1986). All this helps explain the slow deepening of the MFC up to 14/12-36 (see Fig. 3.1). Subsequently, the precipitation rate increases, especially near the MFC center, and it becomes more comparable in magnitude to that in Exp. CTL near the end of the 48-h integration (cf. Figs. 4.9a,b). This results in the development of more localized circulations in the vicinity of the MFC (see Fig. 4.8d).

Of particular interest is that while diabatic heating could be responsible for 59% of the MFC total deepening, it produces little differences in the deepening rate and final depth of the system when surface fluxes are withheld. Only 1 hPa central SLP difference occurs between Exps. NFXM and NFXD at the end of the 48-h integration (cf. Figs. 4.6 and 4.8) in spite of the considerable precipitation occurring in Exp. NFXM. The small central SLP difference could be again attributed to the delay in diabatic heating and the poor efficiency of latent energy in the MFC genesis, as discussed above. Another factor that could account for the small SLP difference appears to be closely related to the diabatic influence on the baroclinic structures of the lower troposphere. Specifically, the diabatical heating/cooling can modify directly the low-level temperature structures. In addition, its induced boundary-layer

a)

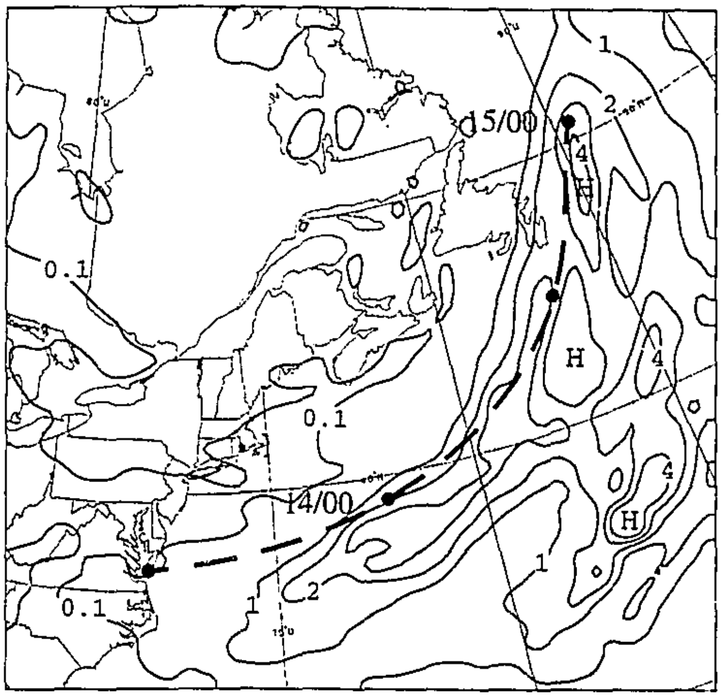

b)

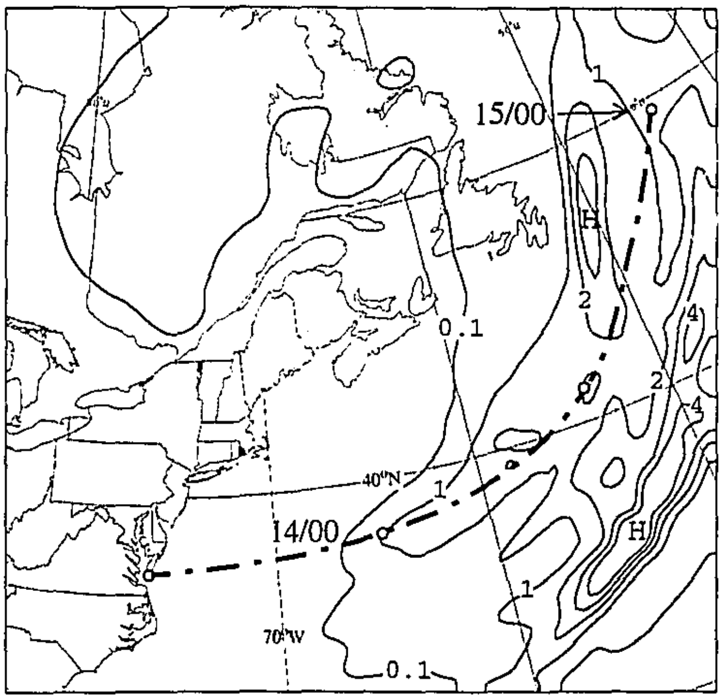

Fig. 4.9 The 48-h accumulated total precipitation for: a) Exp. CTL; and b) Exp. NFXM; and convective precipitation for: c) Exp. CTL; and d) Exp. NFXM, with contours of 0.1, 1, 2, 3, 4 cm. The simulated tracks of the MFC are also shown.

c)

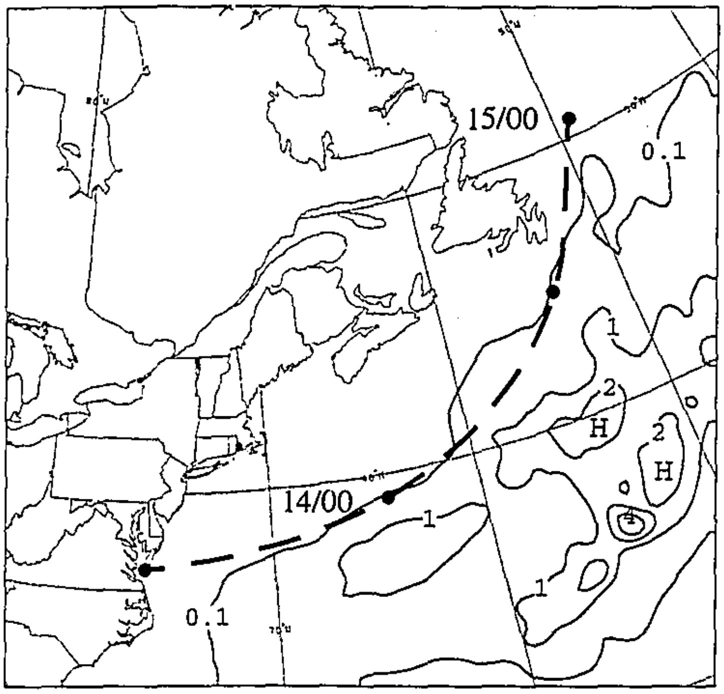

d)

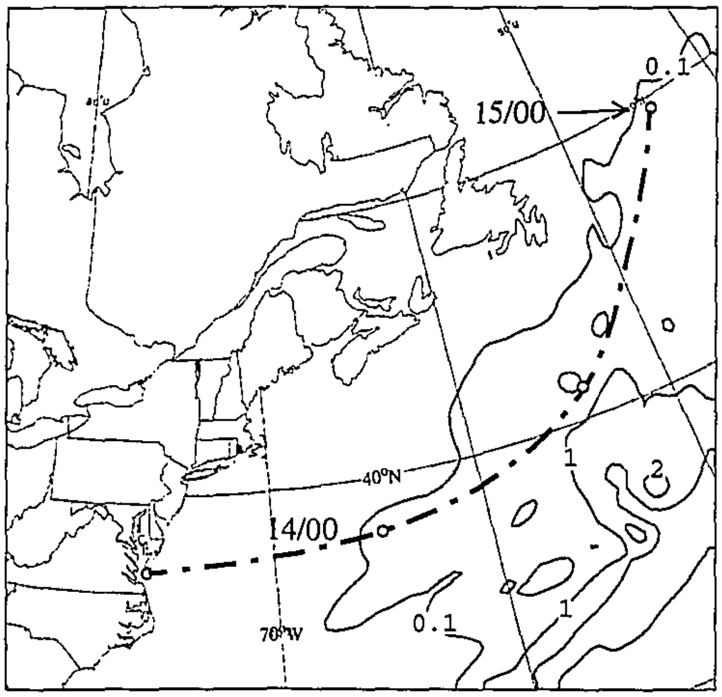

Fig. 4.9 (continued)

convergence tends to enhance the local thermal gradient, while weakening it away from the region; this is also true for the enhanced convergence along the pressure troughs where no precipitation occurs. As a result, a new surface frontal zone forms separately behind the primary cold front as the MFC deepens in the cold sector (see Figs. 4.8b-d). This tends to weaken the low-level cyclone-scale baroclinicity and the deepening of the MFC. Thus, the result reveals that the sea-surface temperature distribution plays an important role, through air-sea interaction, in determining the low-level baroclinic structure; it is indeed a stationary forcing. It also reveals that the impact of surface fluxes on cyclogenesis depends not only on how much precipitation could be produced but also on where the latent heat is released with respect to the cyclone center.

Chapter 5 Summary and Concluding Remarks

In this thesis, a series of (48 - 60 h) numerical simulations of a family of frontal cyclogenesis events that occurred over western Atlantic ocean during 13 - 15 March 1992 have been conducted using a nested-grid version of the PSU/NCAR mesoscale model (MM4) with a fine-mesh grid size of 30 km. These secondary cyclones formed in the large-scale frontal zone with their parent cyclone located in the polar region; they have a diameter of 800-1200 km and an interspacing of 1000-1500 km. One of the secondary cyclones (i.e., MFC) underwent explosive deepening, i.e., at a rate of 32 hPa/30 h, and it eventually overpowered the parent cyclone. Operational numerical weather prediction models, such as those at NMC and CMC, often fail to predict the development of such mesoscale frontal cyclones. In this study, we first obtained a successful 60-h simulation of the cyclogenesis events with enhanced initial conditions and full physics representations, and then performed several sensitivity tests to examine the effects of latent heat release vs. large-scale dynamics, surface friction, surface sensible and latent heat fluxes on the multiple cyclogenesis events.

It is shown that the control simulation reproduces very well the genesis, track and intensity of three secondary cyclones [i.e., the major (MFC), northern (NFC) and southern (SFC) frontal cyclones], the associated thermal structure and precipitation pattern as well as their surface circulations, as verified against the CMC analysis and other available observations. The average e-folding time for the MFC is about 22 h, which is close to theoretical estimation. The quasi-stationary nature and the filling stage of the parent cyclone are also well captured by the model. At the end of the 60-h integration, the model predicts the emergence of several short-wave disturbances in the cold sector behind the primary cold front, which correspond well to the subsequent development of new frontal cyclones seen in the CMC analysis.

It is found from the model simulation that the parent cyclone exhibits a vertically coherent structure during its filling stage, with a high-PV ring near the tropopause separating the secluded polar air from the outside tropical air mass. This PV ring appears to play an important role in determining the initiation and track of the frontal cyclones. It is also found that the MFC genesis begins as a mesoscale disturbance or PV anomaly, which could be traced back 3 days earlier from northern Alberta, travels cyclonically into the large-scale frontal trough that is characterized by intense baroclinicity in the lowest layers. All the secondary cyclones are shown to form as a consequence of the superposition of upper-level PV anomalies on the low-level baroclinicity in the cold sector behind the slow moving primary cold front, and then they propagate towards colder air into the leading frontal zone at a speed of 15 - 20 m s^{-1} and generate their own cold/warm frontal structures. As the MFC intensifies, a mesoscale trough is induced in the low-to-middle troposphere, which creates a favorable phase lag between the new pressure trough and a slow moving thermal wave. This phase lag provides a baroclinic conversion mechanism by which the system's kinetic energy could increase rapidly at the expense of available potential energy. In addition, the frontal cyclones are noted to move from high pressure regions towards the parent cyclone's center, thus gaining angular momentum for the intensification of their cyclonic vorticity. Thus, the parent cyclone provides a favorable environment for the secondary cyclogenesis. The MFC produces considerable amount of precipitation along its track, mostly convective along the cold front and stratiform near its circulation center and warm front.

To isolate the effects of large-scale baroclinicity from diabatic heating on the secondary cyclogenesis, a dry sensitivity experiment is conducted. It is shown that dry dynamics determines the initiation and track of the MFC and NFC, whereas moist processes accelerate the propagation and the deepening of the systems. Dry dynamics accounts for about 59% of the total deepening of the MFC, and its average e-folding time is almost twice as long as that of the moist MFC. However, a slower moving and weaker (dry) MFC tends to reduce its influence on the intensification of the NFC so that the dry NFC ends up with a lower central pressure. On the other hand, diabatic heating has little impact on the NFC genesis because most of the latent energy supply from the south is intercepted by precipitating clouds associated with the MFC system. All these suggest the presence of significant interaction in dynamics and thermodynamics between the frontal cyclones.

The simplified Zwack-Okossi vorticity equation is then calculated using the dry simulation output to examine quantitatively the relative importance of the tropopause depression and the low-level thermal advection in the multiple cyclogenesis events. It is found that the low-level thermal advection accounts for over 60% of the total (dry) deepening of the MFC and about 50% of the deepening of the NFC. This implies that the low-level baroclinicity is more instrumental in determining the explosive deepening of these secondary systems than the upper-level PV anomalies. This finding appears to be different from many of the previous studies of larger-scale cyclones in which upper-level vorticity advection tends to dominate the surface cyclogenesis.

To see whether or not the frontal cyclones would be oceanic phenomena in nature, a sensitivity simulation is conducted in which the dry simulation is rerun but with the ocean surface replaced by a typical 'land' surface roughness. It is found that the model is still capable of reproducing the basic circulation structures of both the MFC and NFC, although they are the slowest moving and deepening systems among all the sensitivity tests being conducted. The e-folding time of the MFC is about 58 h, which is much longer than that in Exps. CTL and DRY. The results reveal that i) the Ekman spin-down is an important parameter in determining the amplification of frontal cyclones; and ii) rapid frontal cyclogenesis phenomena tend to occur more frequently over oceans.

The impact of surface sensible and latent heat fluxes on the frontal cyclogenesis is examined using two sensitivity experiments: one with the surface fluxes switched off from Exp. DRY so that their influence on dry dynamics can be evaluated, and the other with the surface fluxes withheld from Exp. CTL. The dry simulation shows that in the absence of diabatic heating, the surface heat fluxes have very weak impact, through modifying the low-level baroclinicity, on the evolution and final intensity of the frontal cyclones. By comparison, when diabatic heating is allowed, the surface fluxes make significant differences in the deepening of the frontal cyclones as a result of reduced static stability and increased moisture content in the maritime boundary layer. Without the surface fluxes, the moist simulation produces much less convective precipitation ahead of the cold front and delay of grid-box saturation near the cyclone center. In this case, the surface fluxes accounts for about 59% of the MFC's deepening; this impact is as pronounced as turning off the diabatic heating. Similarly, the differences in the final intensity of the frontal cyclones between the dry and moist simulations are small in the absence of surface fluxes. These small differences could be attributed to i) the delay in latent heat release; ii) the formation of new frontal zones behind the primary cold front; and iii) the interception of CAPE and latent energy by precipitating clouds along the primary cold front such that the low-level convergence in the vicinity of the frontal cyclones is reduced. The results suggest that the impact of surface fluxes on cyclogenesis depends not only on how much precipitation could be produced but also on where the latent energy is released with respect to the cyclone center.

It is important to point out, however, that the above conclusions we have reached are based only on a single case study. More case studies of frontal cyclogenesis families are needed to generalize our findings and to provide data upon which to develop theoretical models. Considering the great difficulties of many operational models in predicting mesocyclogenesis in polar frontal zones, the above results clearly indicate the importance of obtaining more realistic upper-level observations and sea-surface temperatures into operational model initial conditions in hope of improving numerical weather prediction of the phenomena. In this regard, FASTEX (Fronts and Atlantic Storm Track Experiment), to be conducted in the next year, will provide a great opportunity to examine the predictability of frontal cyclogenesis events and study their genesis mechanisms.

Appendix A
Calculation of the e-folding time

Consider the Q-G vorticity equation valid at the center of a cyclone,

$$\frac{\partial \zeta_g}{\partial t} = -(\zeta_g + f)\ \nabla\cdot\mathbf{V} \tag{1}$$

where for the free atmosphere,

$$\zeta_g = \frac{g}{f}\ \nabla^2 h, \tag{2}$$

and at the surface,

$$\zeta_g = \frac{1}{f\rho_0}\nabla^2 p. \tag{2'}$$

Integrating Eq. (1) gives the growth rate of the cyclone with a unit of s^{-1},

$$-\nabla\cdot\mathbf{V} = \frac{1}{\Delta t}\ln\frac{(\zeta_g + f)|_{t1}}{(\zeta_g + f)|_{t0}}, \tag{3}$$

where $\Delta t = t_1 - t_0$. The inverse of the growth rate is the e-folding time, i.e., the time it takes for the perturbation to amplify by 2.72, or the doubling time. It is defined as

$$T_e = -\frac{1}{\nabla\cdot\mathbf{V}}\ . \tag{4}$$

Note that the e-folding time can not be computed directly from the divergence of the horizontal winds because of the presence of strong ageostrophic components.

To evaluate the growth rate of the MFC, we compute the e-folding time every 6 hours [i.e., Δt = 6 h in Eq. (3)], starting from 13/12-12, for Exps. CTL, DRY and NOC. Then, a vertically averaged T_e value between 900 and 1000 hPa is calculated to provide a more meaningful and consistent e-folding time at each time level.

Table A.1 The e-folding time averaged between 900 and 1000 hPa for Exps. CTL, DRY and NOC.

e-folding time (hour)			
Model hour	CTL	DRY	NOC
12-18	18.4	42.4	59.34
18-24	24.05	44.5	60.51
24-30	20.05	36.42	58.84
30-36	23.6	36.16	55.87
36-42	24.7	41.82	58.04
42-48	20.25	43.97	56.34
Average	21.8	40.8	58.2

References

Anthes, R. A., and T. T. Warner, 1978: The development of mesoscale models suitable for air pollution and other mesometeorology studies. *Mon. Wea. Rev.*, **106**, 1045-1078.

———, and D. Keyser, 1979: Tests of a fine-mesh model over Europe and the United States. *Mon. Wea. Rev.*, **107**, 963-984.

———, Y.-H. Kuo and J. R. Gyakum, 1983: Numerical simulation of a case of explosive marine cyclogenesis. *Mon. Wea. Rev.*, **111**, 1174-1188.

———, E.-Y. Hsie, and H. L. Kuo, 1987: Description of the Penn State/NCAR mesoscale model version 4 (MM4). NCAR Tech. Note, NCAR/TN-282, 66pp.

Arakawa, A., and V. R. Lamb, 1977: *Computational design of the basic dynamical process of the UCLA general circulation model. Methods in Computational Physics*, **17**, Academic Press, 173-265.

Benjamin, S. G., and N. L. Seaman, 1985: A simple scheme for objective analyses in curved flow. *Mon. Wea. Rev.*, **113**, 1184-1198.

Bjerknes, J., and H. Solberg, 1922: Life cycle of cyclones and the polar front theory of atmospheric circulation. *Geofys. Publ.* **3**(1).

Blackadar, A. K., 1976: Modeling the nocturnal boundary layer. *Preprints, Third Symp. on Atmos.Turbulence, Diffusion and air Quality*, Raleigh, Amer. Meteor. Soc., 46-49.

———, 1979: High resolution models of the planetary boundary layer. *Advances in Environmental Science and Engineering*, **1**, Edited by Pfafflin and Ziegler, Gordon and Breach Sci. Pub., New York, 50-85.

Bosart, L. F., and S. C. Lin, 1984: A diagnostic analysis of the Presidents' Day storm of February 1979. *Mon. Wea. Rev.*, **112**, 2148-2177.

———, and F. Sanders, 1991: An early-season coastal storm: Conceptual success and model failure. *Mon. Wea. Rev.*, **119**, 2831-2851.

Boyle, J. S., and L. F. Bosart, 1986: Cyclone-anticyclone couplets over North America. Part II: Analysis of a major cyclone event over the eastern United States. *Mon. Wea. Rev.*, **114**, 2432-2465.

Bretherton, F. P., 1966: Critical layer instability in baroclinic flows. *Quart. J. Roy. Meteor. Soc.*, **92**, 325-334.

Brown, J., and K. Campana, 1978: An economical time-differencing system for numerical weather prediction. *Mon. Wea. Rev.*, **106**, 1125-1136.

Browning, K.A., and B.W. Golding, 1995: Mesoscale aspects of a dry intrusion within a vigorous cyclone. *Quart. J. Roy. Meteor. Soc.*, **121**, 463-493.

———, and N.M. Roberts, 1994: Structure of a frontal cyclone. *Quart. J. Roy. Meteor. Soc.*, **120**, 1535-1557.

Charney, J. G., 1947: The dynamics of long waves in a baroclinic westerly current. *J. Meteor.*, **4**, 135-162.

Chen, S.-J., C. B. Chang and D. J. Perkey, 1983: Numerical study of an AMTEX'75 oceanic cyclone. *Mon. Wea. Rev.*, **111**, 1818-1829.

Colman, B.R., E.I. Tollerud and R.S. Collander, 1994: Assessing the use of upper-level jet streaks for the operational prediction of winter precipitation. *Preprints, Symposium on the Life Cycle of Extratropical Cyclones*, Bergen, Vol. 3, 274-279.

Davis, C. A., and K. A. Emanuel, 1991: Potential vorticity diagnostics of cyclogenesis. *Mon Wea. Rev.*, **119**, 1929-1953.

———, M. T. Stoelinga and Y.-H. Kuo, 1993; The integrated effect of condensation in numerical simulations of extratropical cyclogenesis. *Mon. Wea. Rev.*, **121**, 2039-2330.

Delsol, F., K. Miyakoda and R. H. Clarke, 1971: Parameterized processes in the surface boundary layer of an atmospheric circulation model. *Quart. J. Roy. Meteor. Soc.*, **97**, 181-208.

Desjardins, S., 1993: Etude diagnostique d'un front froid à l'aide de l'équation de dévelopment de Zwack-Okossi version étendue utilisant les sorties du modèle régional aux éléments finis. M. Sc. thesis, UQAM.

Doyle, J. D., and T. T. Warner, 1991: A Carolina coastal low-level jet during GALE IOP 2. *Mon. Wea. Rev.*, **119**, 2414-2428.

———, and ———, 1992: A numerical investigation of coastal frontogenesis and mesoscale cyclogenesis during GALE IOP 2. *Mon. Wea. Rev.*, **121**, 1048-1077.

Dudhia, J., 1989: Numerical study of convection observed during the winter monsoon experiment using a mesoscale two-dimensional model. *J. Atmos. Sci.*, **46**, 3077-3107.

Eady, E. T., 1949; Long waves and cyclone waves. *Tellus*, **1**, 33-52.

Ertel, H., 1942: Ein Neuer Hydrodynamischer Wirbelsatz. *Met. Zeits.*, **59**, 271-281.

Fitz-Roy, R., 1863: *The Weather Book.* Longman and Green.

Ford, R. P., and G. W. K. Moore, 1989: Secondary cyclogenesis - comparison of observations and theory. *Mon. Wea. Rev.*, **118**, 427-446.

Hack, J. J. and W. H. Schubert, 1986: Nonlinear response of atmospheric vortices to heating by organized cumulus convection. *J. Atmos. Sci.*, **43**, 1559-1573.

Harrold, and Browning, 1969: The polar low as a baroclinic disturbance. *Quart. J. Roy. Meteor. Soc.*, **95**, 710-723.

Hedley, M., and M. K. Yau, 1991: Anelastic modeling of explosive cyclogenesis, *J. Atmos. Sci.*, **48**, 711-727.

Hikum, G.J., D. Keyser and L. Bosart, 1996: The Ohio Valley wave-merger cyclogenesis event of 25-26 January 1978. Part II: Diagnosis using quasigeostrophic potential vorticity inversion. *Mon. Wea. Rev.*, **124**, in press.

Hirschberg, P. A., and J. M. Fritsch, 1991: Tropopause undulations and development of extratropical cyclones. Part I: Overviews and observations from a cyclone event. *Mon. Wea. Rev.*, **119**, 496-517.

Holton, J.R., 1993: *An Introduction to Dynamic Meteorology*. 3rd edition, Academic Press, New York, 511pp.

Hoskins, B.J., 1990: Theory of extratropical cyclones. *Extratropical Cyclones: The Erik Palmén Memorial Volume*, Edited by Newton and Holopainen, Amer. Meteor. Soc., 64-80.

———, M. E. McIntire and A. W. Robertson, 1985: On the use and significance of isentropic potential vorticity maps. *Quart. J. Roy. Meteor. Soc.*, **111**, 877-946.

Hsie, E.-Y., R. A. Anthes, and D. Keyser, 1984: Numerical simulation of frontogenesis in a moist atmosphere. *J. Atmos. Sci.*, **41**, 2581-2594.

Huo, Z., D.-L. Zhang, J. R. Gyakum, and A. Staniforth, 1995: A diagnostic analysis of the superstorm of March 1993. *Mon. Wea. Rev.*, **123**, 1740-1761.

———, ——— and ——— 1996: The life cycle of the intense IOP-14 storm during CASP II. Part I: Analysis and numerical simulations. *Atmos. - Ocean*, **34**, in press.

———, ——— and ———. 1996: The life cycle of the intense IOP-14 storm during CASP II. Part II: Sensitivity simulations. *Atmos.- Ocean*, **34**, in press.

Joly, A., and A. J. Thorpe, 1989: The stability of a steady horizontal shear front with uniform potential vorticity. *J. Atmos. Sci.*, 47, 2612-2622.

———, and ———, 1990a: Frontal instability generated by tropospheric potential vorticity anomalies. *Quart. J. Roy. Meteor. Soc.*, **116**, 525-560.

———, and ———, 1990b: The stability of time-dependent flows: An application of fronts in developing baroclinic waves. *J. Atmos. Sci.*, **47**, 163-182.

Kain, J. S., and J. M. Fritsch, 1990: A one-dimensional entraining/detraining plume model and its application in convective parameterization. *J. Atmos. Sci.*, **47**, 2784-2802.

———, and ———, 1993: Convective parameterization for mesoscale models: The Kain-Fritsch scheme. The Representation of Cumulus Convection in Numerical Models, *Meteor. Monogr.*, No. **46**, Amer. Meteor. Soc., 165-170.

Kasahara, A., and D. B. Rao, 1972: Instabilities of frontal motions in the atmosphere. *J. Atmos. Sci.*, **29**, 1090-1108.

Kuo, Y.-H., and R. J. Reed, 1988: Numerical simulation of an explosively deepening cyclone in the eastern Pacific. *Mon. Wea. Rev.*, **116**, 2081-2105.

———, and S. Low-Nam, 1990: Prediction of nine explosive cyclones over the western Atlantic with a regional model. *Mon. Wea. Rev.*, **118**, 3-25.

———, M. A. Shapiro and E. G. Donall, 1991: The interaction between baroclinic and diabatic processes in a numerical simulation of a rapidly intensifying extratropical marine cyclone. *Mon. Wea. Rev.*, **119**, 368-384.

Lapenta, W. M., and N. L. Seaman, 1990: A numerical investigation of East Coast cyclogenesis during the cold-air damming event of 27-28 February 1982. Part I: Dynamic and thermodynamic structure. *Mon. Wea. Rev.*, **118**, 2668-2695.

———, and ———, 1992: A numerical investigation of east coast cyclogenesis during the cold-air damming event of 27-28 February 1982. Part II: Importance of physical mechanisms. *Mon. Wea. Rev.*, **120**, 52-76.

Lupo, A. R., P. J. Smith and P. Zwack, 1992: A diagnosis of the explosive development of two extratropical cyclones. *Mon. Wea. Rev.*, **99**, 409-413.

Mansfield, D. A., 1974: Polar lows: The development of baroclinic disturbances in cold air outbreaks. *Quart. J. Roy. Meteor. Soc.*, **100**, 541-554.

Molinari, J., and M. Dudek, 1992: Parameterization of convective precipitation in mesoscale numerical models: A critical review. *Mon. Wea. Rev.*, **120**, 326-344.

Moore, G. K. W., and W. R. Peltier, 1987: Cyclogenesis in frontal zones. *J. Atmos. Sci.*, **44**, 384-409.

———, and ———, 1988: Nonseparable baroclinic instability. Part I: Quasi-geostrophic dynamics. *J. Atmos. Sci.*, **46**, 57-78.

———, and ———, 1989: Nonseparable baroclinic instability. Part II: Primitive-equations dynamics. *J. Atmos. Sci.*, **47**, 1223-1242.

Mullen, S. L., 1979: An investigation of small synoptic-scale cyclones in polar air streams. *Mon. Wea. Rev.*, **107**, 1636-2176.

———, and D. P. Baumhefner, 1988: The impact of initial condition uncertainty on numerical simulations of large-scale explosive cyclogenesis. *Mon. Wea. Rev.*, **117**, 2800-2821.

Nakamura, N., 1988: Scale selection of baroclinic instability - effects of stratification and nongeostrophy. *J. Atmos. Sci.*, **45**, 3253-3267.

Orlanski, I., 1968: Instability of frontal waves. *J. Atmos. Sci.*, **25**, 178-200.

———, 1986: Localized baroclinicity: A source for meso-α cyclones. *J. Atmos. Sci.*, **43**, 2857-2885.

Perkey, D. J., and C. W. Kreitzberg, 1976: A time-dependent lateral boundary scheme for limited-area primitive equation models. *Mon. Wea. Rev.*, **104**, 744-755.

Petterssen, S., D. L. Bradbury and K. Pedersen, 1962: The Norwegian cyclone models in relation to heat and cold sources. *Geofys. Publ.*, **24**, 243-280.

———, and S. Smebye, 1971: On the development of extratropical storms. *Quart. J. Roy. Meteor. Soc.*, **97**, 457-482.

Reed, R. J., 1979: Cyclogenesis in polar air streams. *Mon. Wea. Rev.*, **107**, 38-52.

———, 1990: Advances in knowledge and understanding of extratropical cyclones during the past quarter century: An overview. *Extratropical Cyclones: The Erik Palmén Memorial Volume*, Edited by Newton and Holopainen, Amer. Meteor. Soc., 27-45.

———, M. T. Stoelinga, and Y.-H. Kuo, 1992: A model-aided study of the origin and evolution of the anomalously high potential vorticity in the inner region of a rapidly deepening marine cyclone. *Mon. Wea. Rev.*, **120**, 893-913.

———, and A. J. Simmons, 1991: An explosively deepening cyclone over the North Atlantic that was unaffected by concurrent surface energy fluxes. *Wea. Forecasting*, **6**, 117-122.

———, and G. A. Grell, and Y.-H. Kuo, 1993: The ERICA IOP 5 storm. Part II: Sensitivity tests and further diagnosis based on model output. *Mon. Wea. Rev.*, **121**, 1595-1612.

———, Y.-H. Kuo and S. Low-Nam, 1994: An adiabatic simulation of the ERICA IOP 4 storm: An example of quasi-ideal frontal cyclone development. *Mon. Wea. Rev.*, **122**, 2688-2708.

Reuter, G. W., and M. K. Yau, 1990: Observations of slantwise convective instability in winter cyclones, *Mon Wea. Rev.*, **118**, 447-458.

Richtmyer, R.D., 1957: Difference Methods for Initial-Value Problems. *Interscience*, 283 pp.

Rossby, C. G., 1940: Planetary flow patterns in the atmosphere. *Quart. J. Roy. Meteor. Soc.*, **66**, (suppl) 68-87.

Sanders, F., 1986: Explosive cyclogenesis in the west-central North Atlantic ocean, 1981-84. Part I: Composite structure and mean behavior. *Mon. Wea. Rev.*, **114**, 1781-1794.

———, and J. R. Gyakum, 1980: Synoptic-dynamic climatology of the "bomb". *Mon. Wea. Rev.*, **108**, 1589-1606.

Schär, C., and H. Davies, 1989: An instability of mature cold fronts. *J. Atmos. Sci.*, **47**, 929-950.

Staley, D. O., and R. L. Gall, 1977: On the wavelength of maximum baroclinic instability. *J. Atmos. Sci.*, **34**, 1679-1688.

Thorncroft, C. D., and B. J. Hoskins, 1990: Frontal cyclogenesis. *J. Atmos. Sci.*, **47**, 2317-2336.

Tsou, C. H., P. J. Smith, and P. M. Pauley, 1987: A comparison of adiabatic and diabatic forcing in an intense extratropical cyclone system. *Mon. Wea. Rev.*, **115**, 763-786.

——— and ———, 1990: The role of synoptic/planetary scale interaction during the development of a blocking anticyclone. *Tellus*, **42A**, 763-786.

Uccellini. L.W., 1990: Processes contributing to the rapid development of extratropical cyclones. *Extratropical Cyclones: The Erik Palmén Memorial Volume*, Edited by Newton and Holopainen, Amer. Meteor. Soc., 81-105.

———, and D. R. Johnson, 1979: The coupling of upper- and lower-tropospheric jet streaks and implications for the development of severe convective storms. *Mon. Wea. Rev.*, **107**, 682-703.

———, D. Keyser, K. F. Brill and C. H. Wash, 1985: The Presidents' Day cyclone of 18-19 February 1979: Influence of upstream trough amplification and associated tropopause folding on rapid cyclogenesis. *Mon. Wea. Rev.*, **113**, 962-988.

———, and P. J. Kocin, 1987: The interaction of jet streak circulations during heavy snow events along the east coast of the United States. *Wea. Forecasting*, **2**, 298-308.

Wang, J., 1995: A numerical investigation of the coastal frontal cyclogenesis of 3-4 October 1987. M. Sc. thesis, McGill University, 79pp.

Whitaker, L. M., L. W. Uccellini, and K. F. Brill, 1988: A model-based diagnostic study of the rapid development phase of the Presidents' Day cyclone. *Mon Wea. Rev.*, **116**, 2337-2365.

Zhang, D.-L., 1989: The effect of parameterized ice microphysics on the simulation of vortex circulation with a mesoscale hydrostatic model. *Tellus*, **41A**, 132-147.

———, H.-R. Chang, N. L. Seaman, T. T. Warner, and J. M. Fritsch, 1986: A two-way interactive nesting procedure with variable terrain resolution. *Mon. Wea. Rev.*, **114**, 1330-1339.

———, E.-Y. Hsie and M. W. Moncrieff, 1988: A comparison of explicit and implicit precipitation of convective and stratiform precipitating weather systems with a meso-β-scale numerical model. *Quart. J. Roy. Meteor. Soc.*, **114**, 31-60.

———, and R. A. Anthes, 1982: A high-resolution model of the planetary boundary layer-sensitivity tests — comparisons with SESAME-79 data. *J. Appl. Meteor.*, **21**, 1594-1609.

———, J. S. Kain, J. M. Fritsch and K. Gao, 1994: Comments on "Parameterization of convective precipitation in mesoscale numerical modes: A critical review". *Mon. Wea. Rev.*, **122**, 2222-2231.

———, and R. Harvey, 1995: Enhancement of extratropical cyclogenesis by a mesoscale convective system. *J. Atmos. Sci.*, **52**, 1107-1127.